Epithelial dynamics during mouse neural tube development

By

Laura Bocanegra-Moreno

May, 2023

A thesis submitted to the
Graduate School
of the
Institute of Science and Technology Austria
in partial fulfillment of the requirements
for the degree of
Doctor of Philosophy

Committee in charge:
Mario de Bono, Chair
Jérôme Gros
Carl-Philipp Heisenberg
Anna Kicheva

The thesis of Laura Bocanegra-Moreno, titled Epithelial dynamics during mouse neural tube development, is approved by:

Supervisor: Anna Kicheva, ISTA, Klosterneuburg, Austria

Signature: _____

Committee Member: Carl-Philipp Heisenberg, ISTA, Klosterneuburg, Austria

Signature: _____

Committee Member: Jérôme Gros, Institut Pasteur, Paris, France

Signature: _____

Defense Chair: Mario de Bono, ISTA, Klosterneuburg, Austria

Signature: _____

Signed page is on file

ISTA Thesis, ISSN: 2663-337X

I hereby declare that this thesis is my own work and that it does not contain other people's work without this being so stated; this thesis does not contain my previous work without this being stated, and the bibliography contains all the literature that I used in writing the dissertation.

I declare that this is a true copy of my thesis, including any final revisions, as approved by my thesis committee, and that this thesis has not been submitted for a higher degree to any other university or institution.

I certify that any republication of materials presented in this thesis has been approved by the relevant publishers and co-authors.

Signature: _____

Laura Bocanegra-Moreno

May, 2023

Signed page is on file

Abstract

During development, tissues undergo changes in size and shape to form functional organs. Distinct cellular processes such as cell division and cell rearrangements underlie tissue morphogenesis. Yet how the distinct processes are controlled and coordinated, and how they contribute to morphogenesis is poorly understood. In our study, we addressed these questions using the developing mouse neural tube. This epithelial organ transforms from a flat epithelial sheet to an epithelial tube while increasing in size and undergoing morphogen-mediated patterning. The extent and mechanism of neural progenitor rearrangement within the developing mouse neuroepithelium is unknown. To investigate this, we performed high resolution lineage tracing analysis to quantify the extent of epithelial rearrangement at different stages of neural tube development. We quantitatively described the relationship between apical cell size with cell cycle dependent interkinetic nuclear migrations (IKNM) and performed high cellular resolution live imaging of the neuroepithelium to study the dynamics of junctional remodeling. Furthermore, developed a vertex model of the neuroepithelium to investigate the quantitative contribution of cell proliferation, cell differentiation and mechanical properties to the epithelial rearrangement dynamics and validated the model predictions through functional experiments. Our analysis revealed that at early developmental stages, the apical cell area kinetics driven by IKNM induce high levels of cell rearrangements in a regime of high junctional tension and contractility. After E9.5, there is a sharp decline in the extent of cell rearrangements, suggesting that the epithelium transitions from a fluid-like to a solid-like state. We found that this transition is regulated by the growth rate of the tissue, rather than by changes in cell-cell adhesion and contractile forces. Overall, our study provides a quantitative description of the relationship between tissue growth, cell cycle dynamics, epithelia rearrangements and the emergent tissue material properties, and novel insights on how epithelial cell dynamics influences tissue morphogenesis.

Acknowledgments

I would like to start by expressing my gratitude to Prof. Anna Kicheva for her support and trust throughout this journey. Her professional and personal mentorship has been invaluable, and I will always be thankful for her scientific rigor, which has served as an example for me to grow as a scientist. Thank you Ani!

I am also deeply grateful to Prof. Marcin Zagórski, whose endless scientific support has enriched the scope of our research project. It has been a privilege to work with both Marcin and Ani.

Furthermore, I would like to extend my appreciation to Prof. Carl-Philipp Heisenberg and Prof. Jérome Gros for accepting to be on my thesis committee and for their scientific inputs during my PhD. I am also thankful to Prof. Edouard Hannezo for supporting our research work by sharing his ideas and knowledge with us.

I am indebted to all members of the Kicheva Lab, to Katarzyna Kuzmicz-Kowalska and Kasumi Kishi for the fruitful and always encouraging discussions. Amrita Singh, thank you for sharing your skills with me and for your experimental and analytical support. Thomas Minchington, Stefanie Rus, Rohit Harish, Monika Kulig, Catherine Gilbert, Martina Greunz-Schindler thank you for the many times you helped me in different ways over the years. All of you have contributed to my personal and professional growth during the PhD.

I would also like to express my gratitude to the Imaging and Optics facility and the animal facility at ISTA, without whom my work would not have been possible. Special thanks to Katharina Bauer, whose constant support and availability have facilitated my research in a substantial manner.

This professional achievement would not have been possible without the support of my parents and brother who constitute a safe and nurturing place to return to during challenging times. I am also grateful for the support of my husband, who dedicated time to help me when I needed it and encouraged my personal and professional development. Lastly, I am thankful for my friends in Austria, who have always had open hands and hearts to sustain me during both good and bad times, and I am grateful to have them in my life.

About the author

Laura Bocanegra-Moreno completed a BSc in Biology at Los Andes University in Colombia. In summer of 2016, she completed a MSc in biology with emphasis in Genetics and Development at the University of Geneva in Switzerland, where she investigated the cellular behaviours involved in Hydra regeneration. After her master studies, she joined ISTA graduate school in September 2016 and became part of the group of Anna Kicheva in July 2017. Since then, she has been investigating the relationship between epithelial cell dynamics and tissue growth in mouse neural tube development. In 2019, she co-authored a review entitled "Roadmap on multiscale coupling of biochemical and mechanical signals during development" in *Physical Biology*. During her PhD, Laura presented her research at multiple occasions, including the Development and Stem Cell regional meeting in Vienna, the SFB Neuro Stem Modulators retreat and the "Dynamics of biological systems: from viruses to populations" virtual conference in Krakow. Laura's PhD work performed in collaboration with Edouard Hannezo (ISTA) and Marcin Zagorski (Jagiellonian University) was published in *Nature Physics*.

List of publications

1. Bocanegra-Moreno, L., Singh, A., Hannezo, E., Zagorski, M., Kicheva, A. (2023). Cell cycle dynamics control fluidity of the developing mouse neuroepithelium. Nature Physics. https://doi.org/10.1038/s41567-023-01977-w.

2. Lenne, P. F., Munro, E., Heemskerk, I., Warmflash, A., Bocanegra-Moreno, L., Kishi, K., Kicheva, A., Long, Y., Fruleux, A., Boudaoud, A., Saunders, T. E., Caldarelli, P., Michaut, A., Gros, J., Maroudas-Sacks, Y., Keren, K., Hannezo, E., Gartner, Z. J., Stormo, B., … Tlili, S. (2021). Roadmap for the multiscale coupling of biochemical and mechanical signals during development. *Physical Biology*, *18*(4), 1478-3975.

Table of Contents

List of figures

Chapter 1. Neural tube development and epithelial cell dynamics

1.1 The developing spinal cord

The vertebrate spinal cord arises from the posterior neural tube, which extends along the rostro-caudal body axis (Figure 1A). This organ is one of the characteristic features of the phylum Chordata, which includes a variety of organisms, from the amphioxus, a small marine animal with simple anatomy and without a brain, to vertebrates, such zebrafish and mouse. In vertebrates, the spinal cord is part of the central nervous system (CNS) and is responsible for sensing and transmitting signals of movement between the body and the brain (Leung & Shimeld, 2019).

The vertebrate spinal cord is a central model system for understanding the principles that govern pattern formation. Along the dorsoventral (DV) axis, an elaborate pattern of multiple progenitor subtypes is established during development. This DV organization is dictated by morphogens that form gradients of activity along the DV axis. These morphogens are Shh produced from the notochord and the floor plate, and BMPs and Wnts produced from the roof plate and overlaying ectoderm (Sagner & Briscoe, 2019). These morphogens induce the expression of specific sets of transcription factors to establish discrete domains of neural progenitors that give rise to distinct classes of neurons (Figure 1B) (Sagner & Briscoe, 2019). Pattern formation proceeds in two-phases: before E9.5, neural progenitor identities are actively specified by Shh and Bmp signalling (Kicheva, Bollenbach, Ribeiro, Pérez Valle, et al., 2014). Then after E9.5, morphogen signalling activity decreases, the neural identities are maintained by cross-regulatory interactions between transcription factors (Kicheva, Bollenbach, Ribeiro, Pérez Valle, et al., 2014).

In this research study we investigated how the dynamics of growth, epithelial rearrangements and cell shape changes influence neuroepithelium dynamics during spinal cord development to promote tissue morphogenesis. To provide a comprehensive understanding of this process, we will first describe how the spinal cord forms during embryonic development. Next, we will discuss the evidence of cell rearrangements in the neuroepithelium and the cellular and molecular mechanics that control neural tube growth. Finally, we will examine evidence that supports the regulation of morphogenesis by the epithelium dynamics.

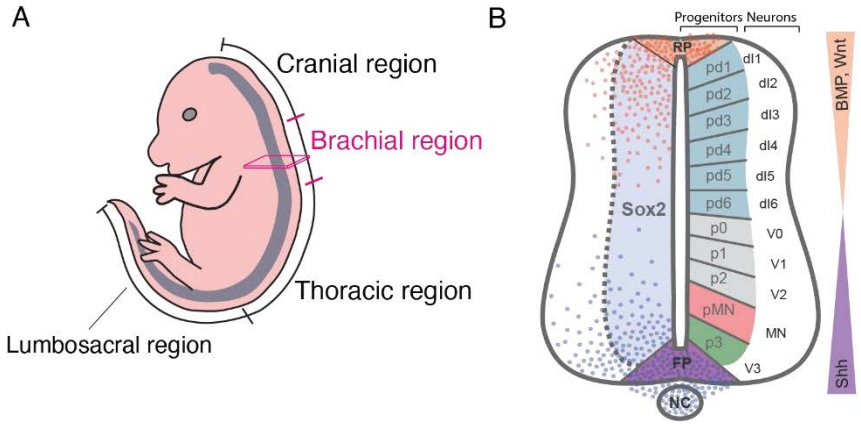

Figure 1. Patterning of the mouse spinal cord. A. Spinal cord regions along the anterior posterior axis of mouse embryos. Spinal cord is coloured in grey. **B.** Transverse section from the brachial region of the spinal cord. The dorsoventral (DV) axis is divided into discrete neural progenitor domains that express specific transcription factors. Shh signalling from the notochord and floor plate in combination with BMP and Wnt from the roof plate direct cell fate specification.

1.2 Neural tube morphogenesis

The embryonic structure that gives rise to the spinal cord in vertebrates is the neural tube. The progenitors that form the neural tube originate in the caudolateral epiblast (CLE), and the node streak border (NSB) (Henrique et al., 2015). These regions harbours neuromesodermal progenitors (NMPs) which have the potential to acquire neural or mesodermal fates, thus contributing to the formation of the neural tube and the paraxial mesoderm (Figure 2A). Once specified, neural progenitors are incorporated into the neural plate, a flat shaped epithelium. Over time, the neural plate bends and folds along the ventral midline to form a closed neural tube.

Neural plate extension along the AP axis occurs through the polarized intercalation of neural epithelial cells along medio-lateral axis via a process called convergent extension (CE). In mice, the planar cellular polarity (PCP) pathway is the main regulator of convergent extension. Thereby, mutations in the core genes of the pathway such as *Vangl2*, *Celsr1* and *Dishevelled 1 and 2* results in defects in neural tube extension and closure ultimately, leading to severe phenotypes such as craniorachischisis (Nikolopoulou et al., 2017). Cell intercalation during convergent extension has been associated with the apical accumulation of F-actin and phosphorylated myosin II (pMLC) at short cell boundaries that are preferentially oriented along the mediolateral axis (Nishimura et al., 2012). The apical distribution of these cytoskeletal proteins promoted the anisotropic contraction of the junctions to undergo polarized cell intercalation.

Live imaging of the mouse neural plate showed that cells exchange their positions in several distinct ways: by rosette resolution, T1 transitions, single cell intercalation in which a single cell moves in between two neighbours; and division mediated cell intercalation in which daughter cells after division actively separate and intercalate between neighbouring cells (Williams et al., 2014). In the neural plate, the core components of the PCP pathway regulate the neighbour exchange events. The genetic deletion of *Vangl2* gene decreased the number of clonal cells that separated along the anterioposterior (AP) axis, significantly inhibited the AP resolution of rosettes and decreased the AP/ML ratio of the epithelium (Williams et al., 2014). The relative frequency of the distinct apical junctional remodeling mechanisms was however not affected. The inability of the cells to rearrange along the mediolateral axis when PCP pathway is suppressed demonstrate that this pathway controls the dynamics of cell junctions to promote convergent extension.

In parallel to convergent extension, which commences at the embryonic stage e7.5, the ventral region of the neural plate bends, forming the medial hinge point (MHP) and the lateral sides fold generating the dorsolateral hinge points (DLHPs). Several mechanisms have been proposed to regulate the formation of the hinge points. Cross-repression between active Shh and BMP signalling from the notochord and the surface ectoderm, respectively, has been observed to influence the localization of junctional and cytoskeleton proteins along the apical-basal axis of the epithelium promoting apical constriction (Eom et al., 2011; Ybot-Gonzalez et al., 2002). The reduction in apical cell area at the MHP has been associated to an increase of cells in S-phase, where nuclei are predominantly located at the basal side of the epithelium (Eom et al., 2011). Hence, changes in cell shape are important for MHP formation. In contrast, physical contact of the surface ectoderm with the lateral sides of the neural plate has been found crucial for the formation of the DLHPs, this physical proximity locally increases cell division promoting bending of the dorsal neural plate (McShane et al., 2015). Furthermore,

physical contact of the notochord with the ventral neural plate, and the surface ectoderm with the dorsal neural plate is thought to generate mechanical forces than can alter the cell cycle progression (De Goederen et al., 2022), this might explain the increase in the length of S-phase in the MHP and the acceleration of the cell cycle in the DLHPs however further experimental testing is required to confirm this hypothesis.

To complete the process of neural tube formation, after neural plate bending, the neural folds appose and fuse along the medio-lateral axis of the embryos to form a tube (Figure 2B.). In mammals, neural tube closure proceeds sequentially from three different locations along the AP axis through neural fold fusion, a process also named zippering (Copp & Greene, 2010) . The first point of zippering is initiated at the cervical region where fusion proceeds bidirectionally towards the hindbrain and the trunk, the second point of zippering starts at the boundary between the midbrain-forebrain and the third point occurs at the anterior end of the forebrain (Copp & Greene, 2010). Fusion commences with the interaction between surface ectodermal cells from opposite sides displaying cellular protrusions rich in actin-mediated cytoskeleton structures (Molè et al., 2020). Concomitantly, apical enrichment of actomyosin at the neural folds induces apical constriction and generate a belt-like structure across cells, which promotes neural fold apposition along the mediolateral axis and fusion at the zippering point (Galea et al., 2017). In order to propagate closure, neuroepithelial cells highly expressing integrins at the dorsal folds interact with the fibronectin-rich basal membrane lying in between the neuroepithelium and the surface ectoderm (Molè et al., 2020). Likewise, the surface ectoderm basally attaches to the basal membrane via integrin-mediated adhesion and this coordinated anchorage drives the formation of rosette-like cell arrangements in the surface ectoderm that supports novel cell contacts promoting continuous progression of the neural tube closure (Molè et al., 2020).

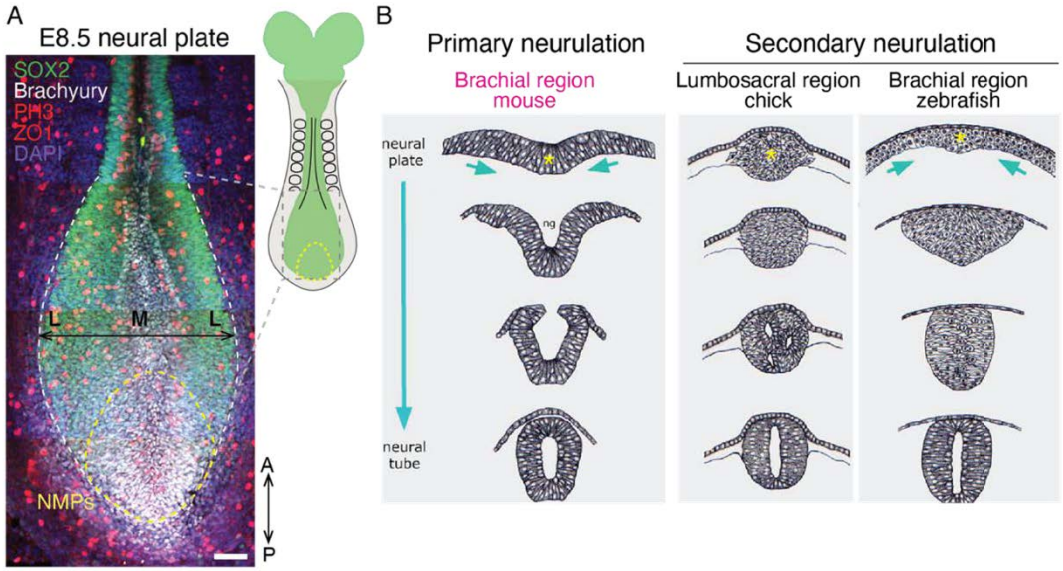

Figure 2. Neural tube morphogenesis in vertebrates. A. E8.5 mouse neural plate marked by the expression of Sox2. Neural plate is highly proliferative, mitotic figures are marked by PH3 expression. Neuromesodermal progenitors (NMPs) localize at the caudal end of the plate and are marked by the co-expression of Sox2 and Brachyury. A, anterior; P, posterior; L, lateral; M, medial**.** Scale bar. 50 μm **B.** Scheme of neural tube morphogenesis in mouse, chich and zebrafish. Green arrowheads indicate epithelia folding. Yellow asterisk indicates the neuroepithelium. (Figure modified from Araya et al., 2016).

Subsequently to primary neurulation taking place from the cranial to the trunk region neural tube as described above, secondary neurulation in mouse and chick starts in the lumbosacral region via aggregation of mesenchymal and neuroepithelial cells (Lowery & Sive, 2004). Secondary neurulation at the lumbosacral region in mouse and chick shares most of the morphogenetic key events that take places during zebrafish neural tube development. In zebrafish, the neuroectodermal cells internalize at the embryo midline originating a rod like structure (Figure. 2B). The formation of the neural keel involves medio-lateral and radial cell intercalations, acquisition of epithelial cell polarity (PAR and adherens junction proteins), oriented cell divisions and the displacement of the mesodermal layer of cells beneath the neural ectoderm(Araya et al., 2014; Geldmacher-Voss et al., 2003; Lowery & Sive, 2004). Next, the lumen is generated from ventral to dorsal direction and deposition of apical and basal markers during cell division is believed to be crucial for this process (Geldmacher-Voss et al., 2003). For instance, lumen formation is greatly impaired in distinct organs in *has* mutant zebrafish where αPKC protein is truncated (Horne-Badovinac et al., 2001).

1.3 Neuroepithelial cell rearrangements

As mentioned in the previous section, neuroepithelial cells exhibit different types of cell rearrangements in the neural plate. Clonal studies in the chick neural tube have suggested that the frequency of cell rearrangements changes over time. This was first observed by Leber & Sanes, 1995 who injected retroviral vectors harbouring the LacZ reporter gene in the chick neural tube between stages Hamburger and Hamilton stage 8 (HH8) and 18 (HH18) and analysed the cell locations at different time points after injection. Analysis of the clones showed that labelling neuroepithelial cells at late stages (between HH15 and HH18) generated clones composed of strands of cells that were in close proximity to each other. By contrast, labelling cells at early stages (between stage HH8 and HH14) produced clones of strands that were more distant. Erskine et al., 1998 observed the same pattern after labelling cells in the neural plate (at HH7-9) or closed neural tube (at HH13-15) using a lipophilic dye (DiA). Clonally related cells marked at early stages spread approximately 92 µm along the DV axis whereas clones labelled at late stages spread approximately 62 µm (Erskine et al., 1998). These results suggest that cell spreading progressively declines during development.

Tracing neural precursor descendants along the mouse central nervous system (CNS) showed the generation of distinct groups of clonally related cells at different regions along the CNS. In particular, clones genetically induced at E9.5 in the spinal cord were coherent (Mathis & Nicolas, 2000), indicating that cell rearrangements are restricted at late stages of mouse neural tube development, and supporting the observations made in the chick neural tube. Together, these findings suggest that cells progressively lose the ability to displace during development.

The study of cell rearrangements in the mouse neural tube has been challenging due to the difficulty of accessing this tissue by live imaging. The spatiotemporal resolution of prior lineage tracing analyses has not been precise enough to result in a full quantitative understanding of the spatiotemporal dynamics of this process during development. Consequently, a quantitative temporal description of mouse neuroepithelial cell rearrangement during mouse neural tube development is not yet established. In addition, it is currently is unknown how the potential temporal changes in cell rearrangements during development are regulated. An-

swering these questions is fundamental to understanding how the properties of the neuroepithelium change over time and what is the potential impact of cell rearrangements for neural tube morphogenesis and pattern formation.

1.4 Neural epithelium topology and interkinetic nuclear movements (IKNM)

Interkinetic nuclear movements (IKNM) is a feature present in different epithelia such as the retina, trachea, brain cortex among others and is known to be an attribute of highly proliferative and pseudostratified epithelia (Norden, 2017). During IKNM nuclei displace from the basal to the apical surface of the epithelium in synchrony with the cell cycle progression. During the G1 phase, nuclei move basally and are located at the basal surface of the epithelium when reaching the S phase. Subsequently nuclei migrate apically during G2 phase and execute mitosis once the nucleus is located at the apical surface (Figure 3A-B).

The molecular mechanisms behind the concerted movement of nuclei with the cell cycle phase have been investigated in different systems that display this phenomenon. For instance, cell cycle progression was found necessary for apical nuclei migration in epithelial cells at the ventricular zone of the mouse dorsal cortex. In the cortex, cells exhibit stochastic back and forth movement during nuclei basal migration whereas apical nuclei displacement is faster and linear (Kosodo et al., 2011). However, when cells were arrested in G1 phase via electroporation and expression of *p18*, a cyclin dependent kinase inhibitor, these G1 arrested cells remained at the basal surface of the epithelium without commencing apical migration (Kosodo et al., 2011). Consistently, when cells were arrested in S phase after Hydroxyurea (HU) treatment, an inhibitor of ribonucleotide reductase that halts DNA replication, arrested cells accumulated basally. Impediment of S/G2 mediated basal to apical migration reduces the apical density of mitotic cells, thereby indirectly affecting basal nuclear movement in G1 (Kosodo et al., 2011).

IKNM has also shown to require cell-cycle dependent microtubule regulation. Cell cycle-dependent regulation by the microtubule nucleation factor Tpx2 facilitates basal to apical nuclei migration in S to G2 phase progression in the mouse dorsal cortex (Kosodo et al., 2011). Similarly, in the chick neural tube, apical nuclear migration in G2 is dependent on microtubules dynamics, while the subsequent rounding of mitotic cells close to the apical surface has been shown to depend on actin polymerisation (Spear & Erickson, 2012). Inhibition of either actin polymerization or Myosin II activity leads to mitosis far from the apical surface (ectopic mitosis) (Spear & Erickson, 2012).

Basal ectopic mitosis is also induced by aPKC overexpression along the neuroepithelial cell cortex. This disrupts the apical distribution of actomyosin and leads to defective integration of the daughter cells in the epithelium, perturbing the normal formation of the neuronal layer (Strzyz et al., 2015). Therefore, the apical location of the nucleus during mitosis in important to ensure tissue integrity during development. It was also found that Cdk1, a cyclin dependent kinase is an important upstream regulator of apical nuclei movement since inhibition of one of its repressors (the Wee1 kinase) during S phase resulted in premature apical displacement (Strzyz et al., 2015). Thus, Cdk1 activity could support the robust apical movement of nuclei to execute mitosis in challenging scenarios where other players have been altered, such microtubule disruption.

A key question for understanding the impact and regulation of IKNM is how this phenomenon is coordinated with the dynamics of the cell cycle and with changes in epithelia architecture. Transformation of the neuroepithelium from a neural plate to a neural tube involves changes in distinct features of the epithelium, one of which is the degree of pseudostratification. The neural epithelium is composed of a single layer of cells with the nuclei located at different positions along the apicobasal axis of the epithelium due to IKNM (Figure 3A-B). Initially, prior to E8.5, the apicobasal axis of cells is short and cells are nearly cuboidal. Subsequently, cells acquire a columnar shape caused by their elongation of cells along the apicobasal axis (Grego-Bessa et al., 2015). In chick and mouse, neural progenitor height increases by about 2.5 fold over a period of two days (from HH13, ~ E8.5 in mouse, to HH23, ~ E10.5 in mouse). This increment of progenitor cell height has been observed to be accompanied by a similar fold increase (2.3 fold) in the number of pseudo-layers (Ferreira et al., 2019). The temporal changes in cell geometry have been linked to changes in major cytoskeleton components such as Myosin II, F-actin and microtubules. This has been observed in the zebrafish retina where F-actin and myosin II localization changes during IKNM, both cytoskeleton proteins were found accumulated basal to the nucleus through interphase whereas during mitosis they re-located at the cell cortex (Norden et al., 2009). The changes in actomyosin localization correlated with differences in cell shape, apical surface area was larger than the basal surface area during mitosis whereas cells were apically constricted during interphase (Yanakieva et al., 2019). Changes in microtubule cellular distribution have also been shown to correlate with changes in cell geometry between the neural plate and keel stages in zebrafish (Jayachandran et al., 2016).

The relationship between IKNM and cell cycle length was examined using a computational model of the cortex neuroepithelium (Kosodo et al., 2011). The model revealed that cell cycle length strongly affects the velocity of apical to basal nuclei migration. As development progresses, the length of the cell cycle in the ventricular zone of the cortex undergoes a significant increase. Specifically, at E11 the cell cycle lasts for 8 hours, whereas at E16 it lasts for approximately 17 hours. This increase correlates with the changes in apicobasal elongation of the cells - at E11 the mean cell height is 40 µm, whereas at E16 is 70 µm (Takahashi et al., 1995). The same relationship is observed in the mouse neural tube where the cell cycle length increases from 12 hours at E8.5 to 20 hours at E11.5, and the apicobasal depth increases from about 40 µm to 100 µm (Kicheva, Bollenbach, Ribeiro, Pérez Valle, et al., 2014). The trend in the chick neural tube is similar (Ferreira et al., 2019; Kicheva, Bollenbach, Ribeiro, Pérez Valle, et al., 2014). This link between the duration of the neuroepithelial cell cycle and the elongation of the apicobasal axis suggests regulatory feedback between the cell cycle temporal dynamics and cell geometry.

A cell-based model of IKNM in the chick neuroepithelium suggested that cell proliferation increases the apicobasal depth of the epithelium and leads to changes in the distribution of the nuclei along this axis, promoting pseudostratification (Ferreira et al., 2019). The study found that IKNM plays a role in mediating apical nuclei crowding and apical mitosis, but it does not affect cell height when cell proliferation is absent. Moreover, it was observed that IKNM helps preserving the apical surface shape of the simulated tissue in the condition where force-mediated apical contractility has caused distortions in shape (Ferreira et al., 2019). The effect of apical cell division in pseudostratification and tissue shape has also been observed in the mouse cochlear duct, where different regions of the epithelium display distinct degrees of pseudostratification due to different levels of proliferation (Ishii et al., 2021). The medial

epithelial layer (MEL) has nuclei allocated at different position along the basal-luminal axis with mitosis actively occurring at the luminal side and strong tissue curvature (Ishii et al., 2021). In contrast, in the lateral epithelial layer (LEL) that is flat, nuclei were similarly aligned along the basal-luminal axis with few divisions taking place apically. Epithelium depth is slightly different between these regions, longer in the MEL (Ishii et al., 2021). Altogether, these results indicate that the major cellular regulators of tissue packing and pseudostratification in epithelia are cell proliferation and cell cycle dependent IKNM and that cell elongation might be controlled by additional cellular mechanisms.

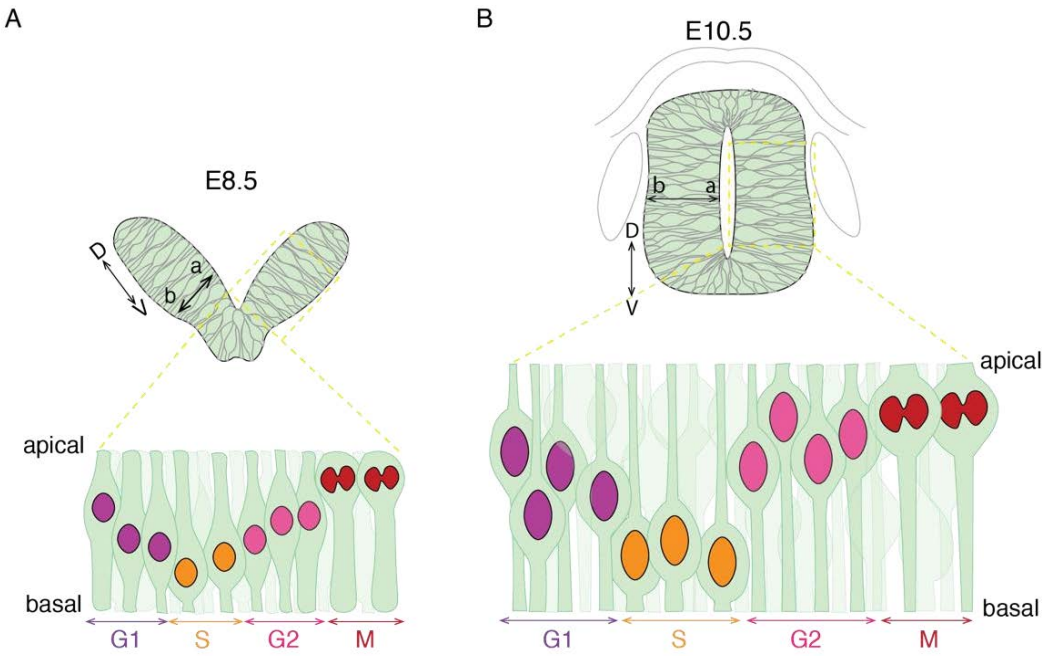

Figure 3. Schematic of IKNM and pseudostratification in the mouse neuroepithelium at different developmental stages. **A.** Schematic of IKNM at E8.5. Nuclei at distinct stages of the cell cycle are indicated in different colors. D, dorsal; V, ventral; a, apical; b, basal. **B.** Schematic of IKNM at E10.5.

1.5 Growth and pattern formation of the neural tube

Throughout the process of neural tube formation, the epithelium undergoes significant growth along various axes. From E8.5 to E11.5 of mouse development, the apicobasal length increases ~2.5-fold, and the DV length increases ~3-fold (Kicheva, Bollenbach, Ribeiro, Pérez Valle, et al., 2014; Kuzmicz-Kowalska & Kicheva, 2021). Extension of the neural tube along the AP axis depends on convergent extension, on the supply of neural progenitor cells from the population of NMP and on cell proliferation (Steventon et al., 2016; Tzouanacou et al., 2009). Similarly, the increase in DV length of the neural tube is driven by a significant increase in progenitor numbers resulting from cell division.

Different modes of cell division have been observed during neural development. Live imaging of GFP labelled progenitors in the chick neural plate allowed to observe they undergo symmetric cell divisions where one progenitor cell give rise to two progenitor daughter cells after cytokinesis rather than one progenitor cell and one differentiated cell (asymmetric division) (Wilcock et al., 2007). The symmetric divisions observed in the chick neural plate do not display a preferred orientation of the mitotic spindle in the plane of the epithelium (Sausedo &

Schoenwolf, 1997). Similarly, in the closed neural tube, cell division can take place parallel or perpendicular to the apical surface of the epithelium without a preferred orientation (Wilcock et al., 2007). The orientation of cell division in particular at late stages is less well understood in the mouse neural tube, because of the difficulty of performing live imaging at late stages in this organism. Nevertheless, current observations support the idea that the changes in epithelium dimensions are independent from the orientation of cell division.

The neural tube growth dynamics changes over time. Neural progenitors, regardless of their type or DV position, proliferate faster at early stages (prior to E9.5) than at late stages (Kicheva, Bollenbach, Ribeiro, Pérez Valle, et al., 2014). In the mouse and chick neural tube signalling by Fgf, Shh and Wnt have been shown to regulate the dynamics of growth. At the early stages of neural tube morphogenesis, Fgf signalling maintains the proliferative state of neural progenitors thereby contributing to the elongation/growth of the neural plate. Distinct Fgfs and Wnts family members are highly expressed in the caudal region of the neural plate, where the NMPs are located (Delfino-Machín et al., 2005; Lunn et al., 2007). Inactivation of Wnt signalling in double *Wnt3*$^{-/-}$, *Wnt8*$^{-/-}$ mutants results in reduced *Fgf8* expression and a narrow neural plate (Cunningham et al., 2015). The effect of Fgf signalling on cell proliferation was demonstrated using live imaging in the chick neural tube. Exposure of the neural tube to Fgf4 lead to increased symmetric divisions, shorter cell cycle length and in several instances to ectopic mitoses (Wilcock et al., 2007). Regulation of cell proliferation by Fgf was found to be mediated by Cyclin D2, which modulates the G1 to S phase transition (Lobjois et al., 2004). Thus, at early stages of neural tube development, Fgfs are important regulators of cell cycle progression.

After neural tube closure, progenitor proliferation depends on Wnt signalling. Several ligands that activate the Wnt signalling cascade are expressed in the chick neural tube. Electroporation of Wnt1 and Wnt3a ligands in the chick neural tube at HH11 increased the rate of neural progenitor division, which lead to tissue bulges and reduction in the number of neurons marked by the expression of neural *Tubulin* (Megason & McMahon, 2002). Based on BrdU labelling analyses, augmented Wnt signalling increased the proportion of cells in S phase at the expenses of the G1 and G2 phases which correlated with the increase in expression of *Cyclin D1*. Wnt control of cell proliferation was found to be mediated by the canonical effector of this signalling pathway, b-catenin (Megason & McMahon, 2002).

Besides Wnt signalling, there is evidence that Shh also regulates growth in the neural tube. Removal of the notochord (notochordectomy), the source that produces Shh during early neural tube development, resulted in reduction of the size, perturbations in the shape of the neural tube, and impeded the formation of the floor plate (Ran Straaten & Hekking, 1991). Targeted genetic disruption of Shh function (Chiang et al., 1996) led to mutant embryos without floor plate, with smaller neural tube and brain, decreased overall body size and cyclopia (Chiang et al., 1996). In contrast, loss of *Patched1* and *Hip1*, which inhibit Shh signalling, generated large mouse neural tubes with expanded floor plates ventral progenitor domains (Jeong & McMahon, 2005). These results suggested that Shh signalling controls not only patterning but also tissue growth.

Further studies of how Shh signalling controls growth observed that several components of the pathway are involved in promoting cell proliferation. Electroporation of a dominant active version of Patched 1, which cannot bind to Shh but can inhibit Smoothened, thus suppressing SHH activity, led to a decreased number of mitotic cells, without affecting the number of post-

mitotic neurons (Cayuso et al., 2006). The number of mitotic cells was restored after co-electroporating a modified version of Gli3, that only contain the DNA binding domain losing the transcriptional repression function (Cayuso et al., 2006). Moreover, constitutive expression of Gli3A transcriptional activator increased the levels of mitosis, the expression of *Cyclin D1* and the size of the treated neural tube (Cayuso et al., 2006). This suggests a direct link between the main effectors of Shh signalling pathway and cell proliferation.

Investigation of the temporal dynamics of neuronal differentiation in the chick neural tube revealed that Shh modifies the mode of division of neural progenitors. Live imaging revealed that symmetric divisions (that generate two progenitors) decline from 82% to 7% while asymmetric divisions (that generate a progenitor and a neuron) increase from 18% to 93% between E9.5 (48hpf) and E10.5 (75hpf) (Saade et al., 2013). This pronounced change in the mode of division correlated with the temporal decline of Shh activity in the *Olig2* domain, which occurs as a result of the temporal adaptation of the pathway (Saade et al., 2013). Increasing Shh activity at E10.5 by electroporating a dominant active form of Smoothened (SmoM2), a transmembrane receptor that initiates Shh intracellular signalling, increased by 2-fold the number of symmetric divisions and significantly reduced the number of neurogenic divisions (Saade et al., 2013). These results suggest that Shh promotes proliferative divisions at early developmental stages to expand the size of the progenitor domain, whereas at E10.5 the decline in Shh signalling facilitates cell cycle exit and neuronal differentiation.

Besides the regulation of tissue growth, Shh, BMP and Wnt signalling also control the formation of gene expression pattern along the neural tube DV axis. These growth factors display opposite graded activities, Shh ventrally, and BMP and Wnt dorsally, that signal progenitor cells to acquire distinct cell identities based on the expression of specific transcription factors (Briscoe & Small, 2015). Progenitor transcriptional signatures lead the specification of 11 different progenitor subtypes that mature into different populations of neurons later in development (Briscoe & Small, 2015). Acquisition of neural progenitor identities in response to morphogens signalling starts from approximately E9.0 to E9.5, when the highest levels of Shh and Bmp activity are observed in the epithelium (Andrews et al., 2017; Balaskas et al., 2012), and it progresses until approximately E12.5. Shh and BMP amplitude progressively decline after their peaks of activities (Balaskas et al., 2012; Tozer et al., 2013). This decline in signalling levels over time suggested that these pathways function as morphogens to specify cell identities only at early developmental stages. This was confirmed by an analysis of the variability in the signalling profiles and the positional information that they contain at different stages, as well as by perturbation experiments (Zagorski et al., 2017). Thus, neural progenitor identities are specified prior to E9.5 in mouse. Subsequently, cell identities are maintained by the gene regulatory network that defines cell fates without the need for ongoing morphogen signalling (Balaskas et al., 2012; Exelby et al., 2021; Kicheva, Bollenbach, Ribeiro, Pérez Valle, et al., 2014).

Despite the extensive knowledge on pattern formation and regulation of growth in the neural tube, many questions remain unanswered. It is for example still unclear how individual cells interpret and integrate the signalling from several morphogen pathways to tune their proliferation rate. It is also not known what is the differential contribution of signalling versus other regulators of cell cycle progression, such as mechanical feedback. Conversely, tissue growth itself influences morphogen gradient formation (Wartlick et al., 2011) and therefore influences the levels of signalling and the establishment of pattern (Lenne et al., 2021).

Displacement of cells within tissues caused by growth or active neighbour exchange could separate cells from the morphogen source and could also could affect morphogen cell mediated diffusion (Kicheva & Briscoe, 2015). This in turn might modify the morphogen local activity and response, thus changing the gradient shape and affecting patterning (Kicheva & Briscoe, 2015). Extensive cell movement due to convergent in the zebrafish hindbrain has shown to improve the sharpness of rhombomeres domain boundaries via changes in cell identity mediated by Fgf signalling gradient and cell sorting (Qiu et al., 2021). How convergent extension in the hindbrain affected the gradient dynamics was not described. Thus, it is still unclear how changes in cell position influence gradient formation during neuroepithelium morphogenesis.

1.6 Coordination between epithelial cell dynamics and tissue morphogenesis

The regulation of tissue morphogenesis is likely to involve cell rearrangements, cell proliferation, cell geometry, and IKNM, as perturbations in the dynamics of any of these processes have been shown to affect the size and shape of the tissue (Brooks et al., 2020; Grego-Bessa et al., 2015; Hoijman et al., 2015; Kidokoro et al., 2018; Ybot-Gonzalez et al., 2007). Studies of embryonic tissues and cultured cell monolayers have shown that tissues displaying high fluctuations in cell shape, frequent cell rearrangements and low cell density have fluid-like characteristics. In contrast, low fluctuations in cell shape, lack of cell rearrangements and high cell density are associated with solid-like characteristics (Figure 4) (Petridou & Heisenberg, 2019). During development and morphogenesis, these material properties of tissues may change, leading to rheological phase transitions.

An example of such rheological transition has been described during the elongation of the body axis in zebrafish. The posterior extension of the presomitic mesoderm (PSM) depends on the continuous incorporation of mesodermal progenitor cells from the neuromesodermal progenitors (NMPs) pool (Steventon et al., 2016). Magnetically responsive oil microdroplets inserted in the MPZ and PSM revealed spatial differences in yield stress, which correspond to the maximal mechanical stress that a material can endure before permanent deformation (Mongera et al., 2018). Low yield stress in the mesodermal progenitor zone (MPZ) was related to the high levels of cell displacement due to active fluctuations in cell-cell contacts whereas high yield stress in the PSM was related to low levels of cell displacement due to minor fluctuation in the cell-cell contacts (Mongera et al., 2018). Moreover, the spatial difference in mechanical integrity was also supported by reduction of the extracellular space between cells from posterior to anterior positions. The tissue mechanical response, the difference in cell density and the dynamics of cell movement showed that PSM has solid-like material properties whereas MPZ has fluid-like. Perturbation of the cell-cell contact dynamics in the MPZ by inhibiting myosin activity decreased cell displacement and increased yield stress driving the tissue rigidification (transition from fluid to solid like state) (Mongera et al., 2018). This change in the material properties of the MPZ affected the normal posterior body axis.

Besides cell density and cell contact dynamics, tissue material properties may be affected by cell divisions. During zebrafish gastrulation at the stage of doming, it was observed that tissue spreading and thinning was mediated by the fluid-like state of the central region of the blastoderm (Petridou et al., 2019). Inducing cell clustering of deep cells reduced the width of the blastoderm and impaired its spreading (Petridou et al., 2019). Deep cells fluidity at the center of the blastoderm was found to be mediated by cell-cell contact disassembly during mitotic rounding and by inactive non-canonical Wnt signalling, which in the marginal cells sustains the establishment of stable and long cell-cell contacts through actomyosin contractility after cleavage (Petridou et al., 2019). The findings of this study demonstrate that non-canonical Wnt dependent cell-cell contact dynamics driven by cell division is what controls the tissue fluidity that is necessary to undergo tissue spreading. Reminiscent to this finding, live imaging of quail embryos, computational modelling and perturbation of cell proliferation revealed that cell rearrangements mediated by cell division fluidizes the quail epiblast promoting vortex-like tissue movements that are essential for the primitive streak formation (Saadaoui et al., 2020)

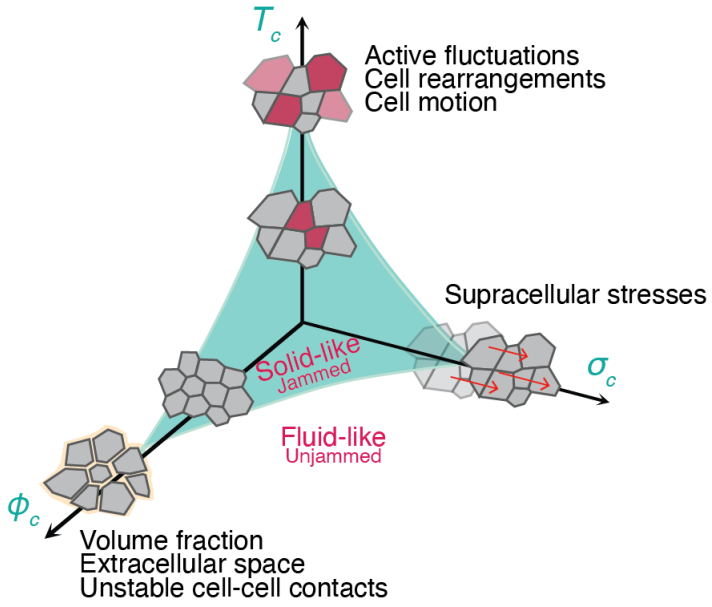

Figure 4. Phase diagram scheme of epithelia physical phase transitions. The physical state of epithelia in embryonic tissues can be influenced by three parameters. Active fluctuations generated by prominent cell motion or cell rearrangements, supracellular stresses originated from tissue tension, and volume fraction determined by the extracellular space between cells that hinders cell contact or unstable cell-cell contacts. Analogous to the biological phase diagram, the physical states of matter are controlled by fluctuations in temperature (T_c), pressure (σ_c) and particle density (ϕ_c). Scheme modified from Lenne & Trivedi, 2022.

In the neural tube, little is known about the dynamics of epithelial cell rearrangements over time and their impact on tissue morphogenesis. Prior studies (described in section 1.3) suggest that extensive cell rearrangements might take place, particularly at early developmental stages. Yet, our quantitative understanding of the extent and properties of these rearrangements is limited. By building a vertex model of mouse neuroepithelium and comparing its output to experimental data, Guerrero et al., 2019 found that the neural tissue grows anisotropically due to oriented T1 transitions. This study also showed that the net rate of tissue growth determines the anisotropy of tissue growth, hence the shape of the tissue. (Guerrero et al., 2019). While Guerrero et al investigated epithelial growth, the did not not explicitly

examine the extent of cell rearrangements, how these rearrangements may change over the course of development, or the factors that regulate the extent of cell rearrangements and tissue material properties. Addressing these questions is crucial to achieve a better understanding of the regulation and impact of tissue material properties during neural tube development.

1.7 Research project aims

In this research study we aimed to quantitatively describe the temporal dynamics of epithelial rearrangements and the apical cell geometry during mouse neural tube development. We focused on the developmental stages between E8.5 (the onset of neural tube development) and E11.5, when pattern formation and motor neuron differentiation is complete.

Our main goal was to understand what factors regulate the extent of cell rearrangements in the neural tube. We aimed to distinguish the contribution of cell proliferation, cell differentiation and cell mechanical forces. To this end, we designed experimental approaches that allow us to measure these factors and combined them with a computational vertex model of the mouse neuroepithelium. We further designed perturbation experiments to test the predictions of the model and validate conclusions.

Finally, we aimed to gain an insight into the relationship between the extent of cell rearrangements, tissue morphogenesis and pattern formation. More specifically, we addressed the questions: what is the impact of cell rearrangements on tissue shape? What is the impact on the precision of gene expression boundaries? How do regulators of morphogenesis, such as PCP signalling, affect cell rearrangements in the neural tube?

Chapter 2. Cell cycle dynamics control fluidity of the developing mouse neuroepithelium

This chapter contains the published manuscript:

Bocanegra-Moreno, L., Singh, A., Hannezo, E., Zagorski, M., Kicheva, A. (2023). Cell cycle dynamics control fluidity of the developing mouse neuroepithelium. Nature Physics. https://doi.org/10.1038/s41567-023-01977-w

Details on methods used in this study as well as references are found in the published manuscript.

nature physics

Article

https://doi.org/10.1038/s41567-023-01977-w

Cell cycle dynamics control fluidity of the developing mouse neuroepithelium

Received: 13 June 2022

Accepted: 1 February 2023

Published online: 06 April 2023

Check for updates

Laura Bocanegra-Moreno[1], Amrita Singh[1], Edouard Hannezo[1], Marcin Zagorski[2] ✉ & Anna Kicheva[1] ✉

As developing tissues grow in size and undergo morphogenetic changes, their material properties may be altered. Such changes result from tension dynamics at cell contacts or cellular jamming. Yet, in many cases, the cellular mechanisms controlling the physical state of growing tissues are unclear. We found that at early developmental stages, the epithelium in the developing mouse spinal cord maintains both high junctional tension and high fluidity. This is achieved via a mechanism in which interkinetic nuclear movements generate cell area dynamics that drive extensive cell rearrangements. Over time, the cell proliferation rate declines, effectively solidifying the tissue. Thus, unlike well-studied jamming transitions, the solidification uncovered here resembles a glass transition that depends on the dynamical stresses generated by proliferation and differentiation. Our finding that the fluidity of developing epithelia is linked to interkinetic nuclear movements and the dynamics of growth is likely to be relevant to multiple developing tissues.

Cells within developing tissues reorganize at the same time as tissue growth takes place. The extent and dynamics of cell rearrangements can substantially change during tissue development[1,2], reflecting solid–fluid transitions in the physical properties of tissues. In most cases, these transitions have been proposed to result from alterations in cell density, cell motility, internal myosin- and/or cadherin-mediated adhesion forces at cell junctions, or external mechanical forces[2–8]. Cell rearrangements have also been shown in theory and in some experimental situations to depend on active stresses within tissues, such as the ones generated by cell division[9–12]. Yet, in many cases, the dynamics of cell rearrangements and the factors that control them are poorly understood.

The spinal cord of amniotes develops from a flat epithelial sheet—the neural plate—that folds to form a closed neural tube[13]. These morphogenetic changes are accompanied by cell intercalations and convergent extension, which are mediated by planar cell polarity and actomyosin-dependent contractility of the apical adherens junctions, as well as basolateral protrusive activity[14,15]. However, whether these are the only factors contributing to cell rearrangements in the neuroepithelium is an open question. Furthermore, the quantitative dynamics of cell rearrangements during development remain unclear. Here we use highly resolved clonal analysis to measure the rate of cell rearrangements in the mouse neuroepithelium over time, thus inferring the long-term rheological properties of the tissue. We further propose a theoretical framework for how active stresses generated during tissue growth contribute to cell rearrangements.

Cell rearrangements decline over time

To quantitatively measure cell rearrangements in the neural tube without the risk of perturbing the native mechanical environment of embryo growth in utero, we used clonal labelling to track how the positions of daughter cells that are initially adjacent change with respect to each other over time (Fig. 1a). A key aspect to achieve reliable tracing is the sparseness of labelling. Mosaic analysis with double markers (MADM)[16,17] is a two-colour labelling system known for its sparseness. Therefore, we used Sox2–CreERT2-induced MADM recombination (Fig. 1a and Supplementary Fig. 1a,b) to label cells with very low probability—we detected between one and five clones per spinal cord (Fig. 1c).

We induced MADM clonal labelling by injecting pregnant mothers with tamoxifen at embryonic days E8.5, E9.5 and E10.5, and harvested the embryos 24 h later. The cytosolic fluorescent reporters allow the labelled cells to be detected at the apical surface of the epithelium

[1]Institute of Science and Technology Austria, Klosterneuburg, Austria. [2]Institute of Theoretical Physics and Mark Kac Center for Complex Systems Research, Jagiellonian University, Krakow, Poland. ✉e-mail: marcin.zagorski@uj.edu.pl; anna.kicheva@ist.ac.at

https://doi.org/10.1038/s41567-023-01977-w

(Fig. 1b,d). In addition, immunostaining for the tight junction marker ZO1 allows us to segment individual cells and precisely determine the number and neighbour relationships of the labelled cells.

We focused our analysis on clones in the dorsal (pD) and intermediate (pI) progenitor domains, which span more than half the D–V length of the neural tube (Fig. 1b). The mean clone sizes of MADM clones decline from 4.1 ± 0.3 cells per clone at E8.5 to 2.1 ± 0.1 cells per clone at E10.5 (Supplementary Fig. 1c). This reflects a twofold decline in the tissue growth rate (from 0.087 ± 0.009 h^{-1} to 0.046 ± 0.004 h^{-1}), which is consistent with previous estimates[18] (Supplementary Fig. 1d and Methods). The clone size distribution at E8.5 further shows that 2, 4 and 8 cell clones are the most abundant, indicating that cells divide up to three times and without substantial progenitor loss (Supplementary Fig. 1e). At E9.5 and E10.5, larger clones are progressively under-represented, consistent with a longer cell cycle length and loss of progenitors due to terminal differentiation at these stages. Together, these observations indicate that the MADM clones accurately reflect the dynamics of tissue growth.

We next analysed the clonal shapes to estimate the extent of cell rearrangements. In many tissues, such as the *Drosophila* wing disc or mouse skin, uniform tissue growth with minimal cell rearrangements results in the formation of coherent clones[19,20]. By contrast, cell rearrangements cause clone fragmentation, where subsets of labelled cells are surrounded by non-labelled neighbours. We, therefore, used the number of fragments per clone as a readout of cell rearrangements. To exclude the effects of clone size, we measured the fragments for clones of a given size. The number of fragments linearly depends on the clone size for small clone sizes (≤4 cells) for which reliable statistics can be obtained (Fig. 1e). This allows us to define the fragmentation coefficient ϕ as the slope of a linear fit to the number of fragments as a function of clone size (for clone sizes ≤4 cells). We found that MADM clones labelled at E9.5 and E10.5 had very few fragments, corresponding to $\phi = 0.11$ (95% confidence interval (CI) of 0.08 and 0.15) and 0.25 (95% CI of 0.21 and 0.30), respectively. By contrast, clones labelled at E8.5 were highly fragmented with $\phi = 0.61$ (95% CI of 0.55 and 0.68) (Fig. 1e).

Consistent with their higher fragmentation, clones labelled at E8.5 had dispersed at a larger maximum distance from the clone centroid, namely, 10.2 ± 1.4 µm, whereas clones labelled at E9.5 and E10.5 dispersed up to 3.3 ± 0.4 and 3.0 ± 0.8 µm, respectively (Supplementary Fig. 1f). The dispersal of cells was nearly isotropic with respect to the clone centre, with the exception of clones in the motor neuron progenitor (pMN) domain, which have a larger A–P/D–V aspect ratio compared with clones in other domains at E10.5 of development (Supplementary Fig. 1g). This effect is consistent with previous observations and is related to the differentiation dynamics in the pMN domain[21]. Altogether, these results indicate that cell rearrangements occur frequently before E9.5 and significantly decline at later stages.

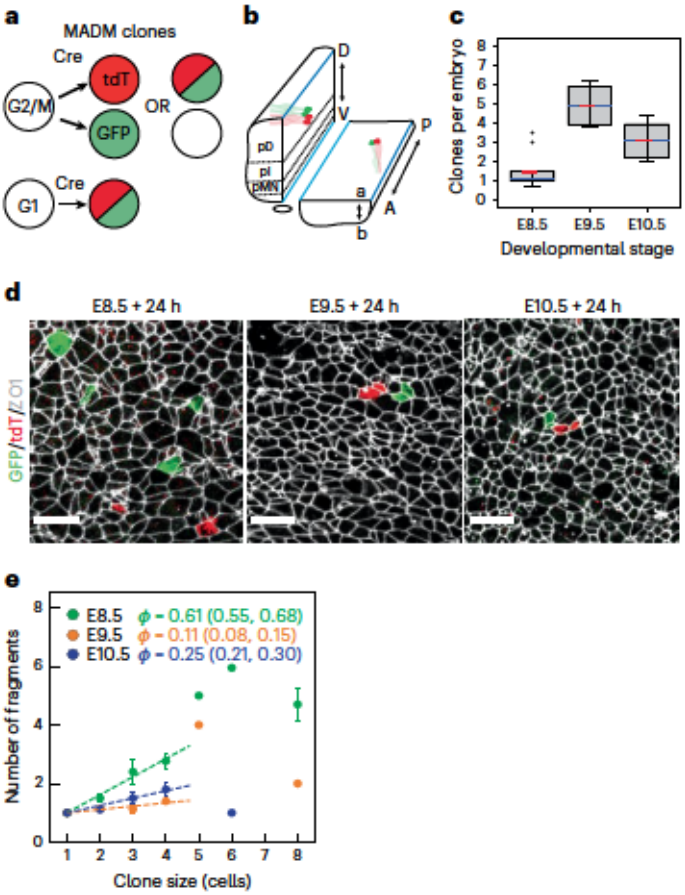

Fig. 1 | Clonal analysis reveals the dynamics of cell rearrangements in the developing spinal cord. a, Clones generated with MADM labelling can comprise cells labelled with EGFP, tdTomato (tdT) or both depending on the type of recombination (Methods). **b**, To analyse the cellular and clonal shapes at the apical surface, the neural tube was opened by dissection along the dorsal and ventral midlines (blue lines). D–V patterning results in the formation of distinct progenitor domains along the D–V axis: pD, pI and pMN are denoted. A, anterior; P, posterior; a, apical; b, basal; D, dorsal; V, ventral. **c**, Mean number of MADM clones per embryo across litters ($n = 10$, 4 and 6 litters at E8.5, E9.5 and E10.5, respectively). 25–75 percentile (box), median (blue), mean (red), highest/lowest observations without outliers (whiskers). Two sided t-tests: $P = 0.005$ (E8.5 versus E9.5); $P = 0.051$ (E9.5 versus E10.5); $P = 0.011$ (E8.5 versus E10.5). **d**, MADM clones induced at the indicated stages and analysed 24 h later. Scale bars, 10 µm. **e**, Mean number of fragments per clone for a given clone size ± s.e.m. Clones analysed 24 h after injection at the indicated stages. Both EGFP and tdTomato cells were included in the analysis. Corresponding fragmentation coefficient ϕ with 95% CI was obtained using linear fit to the data for clones ≤4 cells (dashed lines). Sample sizes (for **c** and **e**). E8.5, $n = 46$ clones; E9.5, $n = 87$ clones; E10.5, $n = 94$ clones (Supplementary Table 1).

Tissue fluidity at high junctional tension and contractility

To investigate how the high extent of cell rearrangements at early developmental stages is achieved, we used a two-dimensional vertex model of the apical surface of the neuroepithelium[21,22]. In this model, polygonal cells change neighbours by a process called T1 transition, in which an edge initially shared between two adjacent cells collapses and subsequently reforms in a different orientation, leading to the separation of the cells. The packing geometry of cells in vertex models depends on the normalized tension (λ) and normalized contractility (Γ) parameters. In the classical vertex model formulation[22], cells have a constant target area. By contrast, in our model, the target area depends on the cell cycle time[21]. This reflects the fact that cells in pseudostratified neural epithelia undergo interkinetic nuclear movements (IKNMs) during the cell cycle. In these movements, the position of the nucleus along the apicobasal axis of cells may affect the apical cell surface area. To verify that the IKNM effect we implemented in the model reflects the actual apical-area cell cycle dynamics in the tissue, we measured the distribution of cell areas as a function of cell cycle phase at E8.5 and E10.5. To do this, we used short (20–30 min) EdU pulse labelling to mark the S-phase nuclei, 2 h EdU pulse to mark the G2 nuclei and phospho–histone 3 staining to mark cells undergoing mitosis (Fig. 2a and Methods). We combined EdU/pH3 immunostaining with sparse mosaic cytosolic tdTomato labelling to identify individual cell bodies, and with ZO1 immunostaining to measure the apical surface areas that correspond to specific nuclei. This analysis confirmed that the position of the nucleus relative to the apical surface changes with the cell cycle at both E8.5 and E10.5, reflecting the fact that the nuclei undergo IKNM (Fig. 2b). Furthermore, consistent with the model, we found that cells

in mitosis have more than twofold higher mean apical cell area than cells in S phase, whereas the mean apical areas of cells in S and G2 phases were similar (Fig. 2c).

In other epithelia, fluctuations in the levels of myosin activity at cell junctions cause variation in the line tension and edge lengths of cells on a timescale of seconds to minutes[23]. We reasoned that a similar effect might occur in the neuroepithelium. We, therefore, introduced line-tension fluctuations in the model as an Ornstein–Uhlenbeck process. To this end, we introduced a noise term in Λ, drawn from a Gaussian distribution with characteristic deviation time σ and temporal correlation time τ (Methods). Increasing values of σ shifted the distribution of edge length fluctuations in the simulations (Fig. 2d). Hence, to obtain an experimental estimate of σ, we performed short-term live imaging of ZO1–GFP-expressing neuroepithelia at E8.5 and E10.5 of development (Methods and Supplementary Video 1). Although this procedure requires neural-tube dissection and the tissues can only be maintained live for 1–2 h, this approach provides an estimate of the variations in edge lengths that occur on shorter timescales. We observed that the distribution of edge length deviation during a 20 min interval corresponds most closely to simulations with $\sigma = 0.02$ at both E8.5 and E10.5 (Fig. 2d); hence, we used this value of σ in our subsequent analysis.

To determine the model parameters that reproduce the experimentally observed clone fragmentation, we performed a systematic screening of the intermediate region of the Λ–Γ parameter space, where the network configuration is expected to be the most similar to epithelial tissues[22,24] (Supplementary Table 2). We used a proliferation rate of 0.09 h^{-1} (equivalent to a cell cycle length of ~8 h), which corresponds to the experimentally measured value at E8.5 (ref. 18 and Supplementary Fig. 1d). We traced clones in silico for 16 h, which corresponds to the duration of Cre activity in experiments (Supplementary Fig. 1b and Methods). The model revealed that the fragmentation coefficient varies across the (Λ,Γ) parameter space (Fig. 3a). In particular, ϕ changes non-monotonically along the Λ axis: it decreases, reaches a local minimum and subsequently increases with increasing values of Λ (Fig. 3a). To qualitatively capture these differences, we defined an arbitrary threshold value of $\phi = 0.3$, which subdivides the parameter space into three subregions. We refer to these as regions A, B and C (Fig. 3a). Regions A and C have high fragmentation ($\phi \geq 0.3$) and high T1 transition rate, whereas region B has low fragmentation ($\phi < 0.3$) and low T1 transition rate (Fig. 3a,b and Supplementary Videos 2–4). To further characterize the differences between regions, we compared the profiles of the self-overlap function[25,26], which quantifies the fraction of cells that remain within approximately a cell radius of their relative initial position in the tissue. We found that these profiles are distinct in regions A and C compared with region B (Extended Data Fig. 1). Differences in the shape of the self-overlap function have been associated with glassy dynamics in vertex models[26], suggesting that the differences between regions A, C and B represent transitions between fluid-like and solid-like states. Previous studies of vertex models have revealed that a density-independent fluid-to-solid phase transition[1,7,22] characterized by a change in cell shape index occurs in a similar position in the parameter space to the transition between regions A and B that we observe. By contrast, the high rate of T1 transitions in region C has not been previously observed and is surprising, given that the ground state of the model in this region is solid[22,24].

The high fragmentation coefficient that we observed at E8.5 (Fig. 1e) is consistent with both high fragmentation regions A and C. Hence, more than one mechanism, captured by either region A or C, could explain how the high fragmentation rates are achieved at early developmental stages. To distinguish potential mechanisms and understand how fragmentation is achieved in the E8.5 neural tube, we compared the cell shapes in simulations of regions A versus C (Fig. 3c–f and Supplementary Fig. 2). Several first-order descriptors of cell shapes (Supplementary Table 3) were similar between regions A and C. For instance, these regions were characterized by high cell shape index and low packing order, measured by the fraction of hexagons, which are indicators of tissue fluidity[7] (Fig. 3d,e). By contrast, a subset of cell shape descriptors differed between regions A and C. These included the coefficients of variation (CV) of the cell area, perimeter and elongation, as well as the area-ratio slope (Supplementary Fig. 2). The most striking difference between regions A and C was that only region C had high cell area CV, whereas in region A, the cell areas were nearly uniform (Fig. 3f).

Comparisons of cell shapes between model and experimental data have been used to infer the mechanical parameters of tissues[27,28]. Therefore, to determine the (Λ, Γ) parameter region characteristic of the E8.5 neuroepithelium, we immunolabelled the tight junctions in E8.5 neural plates and segmented the cell shapes (Fig. 3g). We found that for most cell shape descriptors, the best correspondence between data and simulations is in region C (Extended Data Fig. 2). A simultaneous comparison of a set of several descriptors confirmed that the best match to the experimental data is in region C (Fig. 3h). This suggests that the high fluidity of E8.5 epithelium is achieved in the regime of high junctional tension and contractility characteristic of region C. This is consistent with observations that the maintenance of high junctional tension is needed for proper neural tube closure at early developmental stages[29,30].

IKNM fluidizes the neuroepithelium

High fluidity in region C has not been previously observed; hence, we investigated how the high level of cell rearrangements in this region arises. Because the implementation of an IKNM effect and Λ noise are distinct features of our model, we first compared how the rate of T1 transitions depends on these features (Fig. 4a). In the absence of any cell divisions and noise, T1 transitions are not observed. In the absence of cell divisions, in the presence of only junctional noise with $\sigma = 0.02$, the rate of T1 transitions in region C was also zero, similar to what is expected from the solid ground state of the network in this parameter region. The implementation of cell division by IKNM without Λ noise resulted in a low T1 rate (<0.1 $cell^{-1}\,h^{-1}$). A classical implementation of cell divisions without an IKMN effect, but with linear cell area increase during the cell cycle, both with or without Λ noise, also resulted in a low T1 rate (<0.1 $cell^{-1}\,h^{-1}$) (Fig. 4a and Supplementary Fig. 3a,b). By contrast, the IKNM effect and Λ noise together increased the T1 rate to 0.37 ± 0.02 $cell^{-1}h^{-1}$ and resulted in levels of clone fragmentation that are comparable with the experimentally observed value. This indicates that junctional noise on a timescale of minutes and fluctuations induced by IKNM (on a longer timescale of minutes to hours) cooperate to induce an increase in T1 rates that effectively fluidizes the tissue.

To further explore how IKNM is associated with T1 transitions, we analysed the quartets of adjoining cells undergoing T1 transitions in simulations. This revealed that T1 quartets have a distinct distribution of mean cell areas compared with random quartets of cells (Supplementary Fig. 3c). In particular, T1 quartets have, on average, one large cell and three smaller cells. Consistent with this distribution, a fraction of T1 transitions were followed by cell division of the largest cell in the simulations (Supplementary Fig. 3d). Nevertheless, the majority of T1 events did not coincide with cell divisions and could be either preceded or followed by cell divisions (Supplementary Fig. 3e). Consistent with this, we observed examples of T1 transitions occurring before cell division, after cell division, coincident with division or in the absence of cell division in short-term live-imaging experiments of mouse embryos expressing ZO1–GFP (Supplementary Fig. 4a–d). Furthermore, cell divisions that we observed in time-lapse imaging of neural epithelia mosaically expressing membrane-localized GFP ($n = 17$ dividing cells; Extended Data Fig. 3) were not associated with the separation or rearrangement of daughter cells within at least 30 min after cytokinesis. In addition, treatment with calyculin A, which leads to basolateral enrichment of F-actin (Supplementary Fig. 4e) and has been shown to increase junctional stability at mitosis and prevent

https://doi.org/10.1038/s41567-023-01977-w

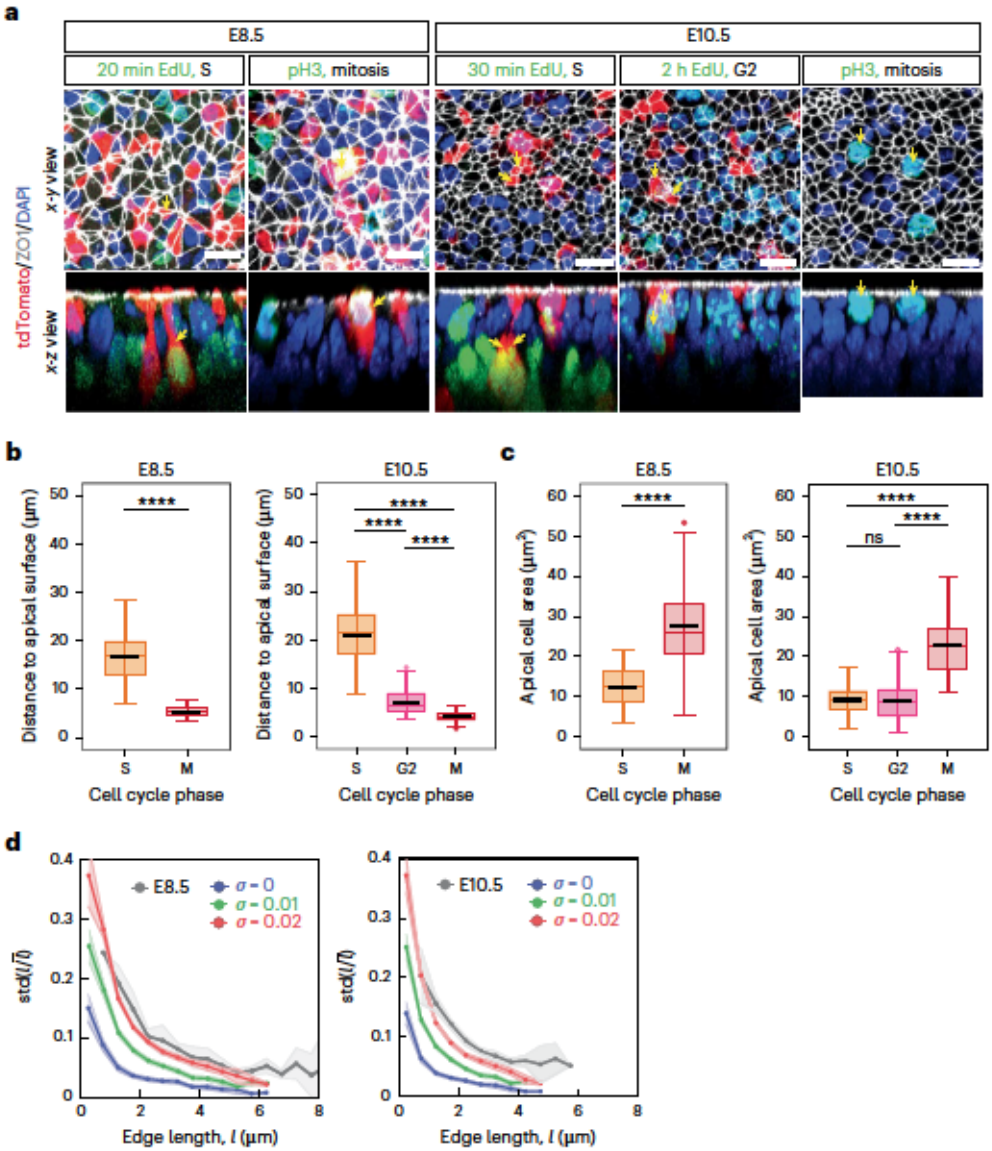

Fig. 2 | IKNM and cell edge fluctuations in the neuroepithelium at E8.5 and E10.5 of development. a, Apical (x–y) and orthogonal (x–z) views of neuroepithelial cells in S, G2 and M phases at E8.5 and E10.5. EdU pulses with defined length and pH3 staining were used to distinguish nuclei in the indicated cell cycle phases. Sparse tdTomato labelling was used to track the cell bodies and associate nuclei with the respective apical surfaces (yellow arrows). Scale bars, 10 μm. **b**, Distance from nuclei centres to the apical surface (ZO1). Mitotic nuclei are close to the apical surface (ZO1), whereas S and G2 nuclei are located more basally. **c**, Apical area of cells in the indicated cell cycle phases. In **b** and **c**, 25–75 percentile (box), median (coloured line), mean (black line), highest/lowest observations without outliers (whiskers). Pairwise comparisons two-sided t-test: ****$P < 0.0001$; ns, not significant, $P > 0.05$. Sample sizes (number of cells): E8.5, S ($n = 172$); M ($n = 179$); E10.5, S ($n = 197$); G2 ($n = 147$), M ($n = 144$) (Supplementary Table 1). **d**, Standard deviation of the relative edge length ($l/\bar{l}$) over a 20 min time interval as a function of absolute edge length l (binned in 0.5 μm bins) for simulations with different levels of noise ($\sigma = 0$, 0.01 and 0.02 with $n = 1{,}900$, 1,827 and 1,687 edges, respectively; Methods) and in time-lapse images of ZO1–GFP-expressing neuroepithelia (E8.5, $n = 309$; E10.5, $n = 387$; Supplementary Table 1). Shaded regions, 95% CI.

direct daughter-cell separation on cytokinesis[11] (Methods), does not affect clone fragmentation in the neural tube (Supplementary Fig. 4f). Altogether, these observations suggest that cell rearrangements are not driven by the mitotic cell or its daughter cells in a direct cell autonomous manner.

To further investigate how IKNM influences cell rearrangements, we asked if the high cell area heterogeneity in the presence of IKNM (Fig. 4b) is sufficient to account for the increased cell rearrangements in region C. To address this possibility, we simulated a tissue without IKNM, in which the cell area grows linearly during the cell cycle, but with target cell areas drawn from a random distribution with CV comparable with the experimentally measured one (linear + A0 noise condition (Methods)). These simulations show that increasing the target cell area heterogeneity is not sufficient to increase the rate of T1 transitions (Fig. 4b,c). An alternative possibility is that the specific kinetics of cell area increase during the cell cycle generated by IKNM leads to a higher rate of T1 transitions. Consistent with this idea, the apical target area that increases exponentially over the cell cycle can generate increased T1 transitions. Furthermore, the sharper the increase in exponential growth rate, the higher is the area heterogeneity and higher is the rate of T1 transitions (Fig. 4a,b). Altogether, this analysis suggests that the specific cell area dynamics during the cell cycle, that is, the sustained low cell area during interphase and rapid increase at mitosis, are crucial for cell rearrangements in region C.

https://doi.org/10.1038/s41567-023-01977-w

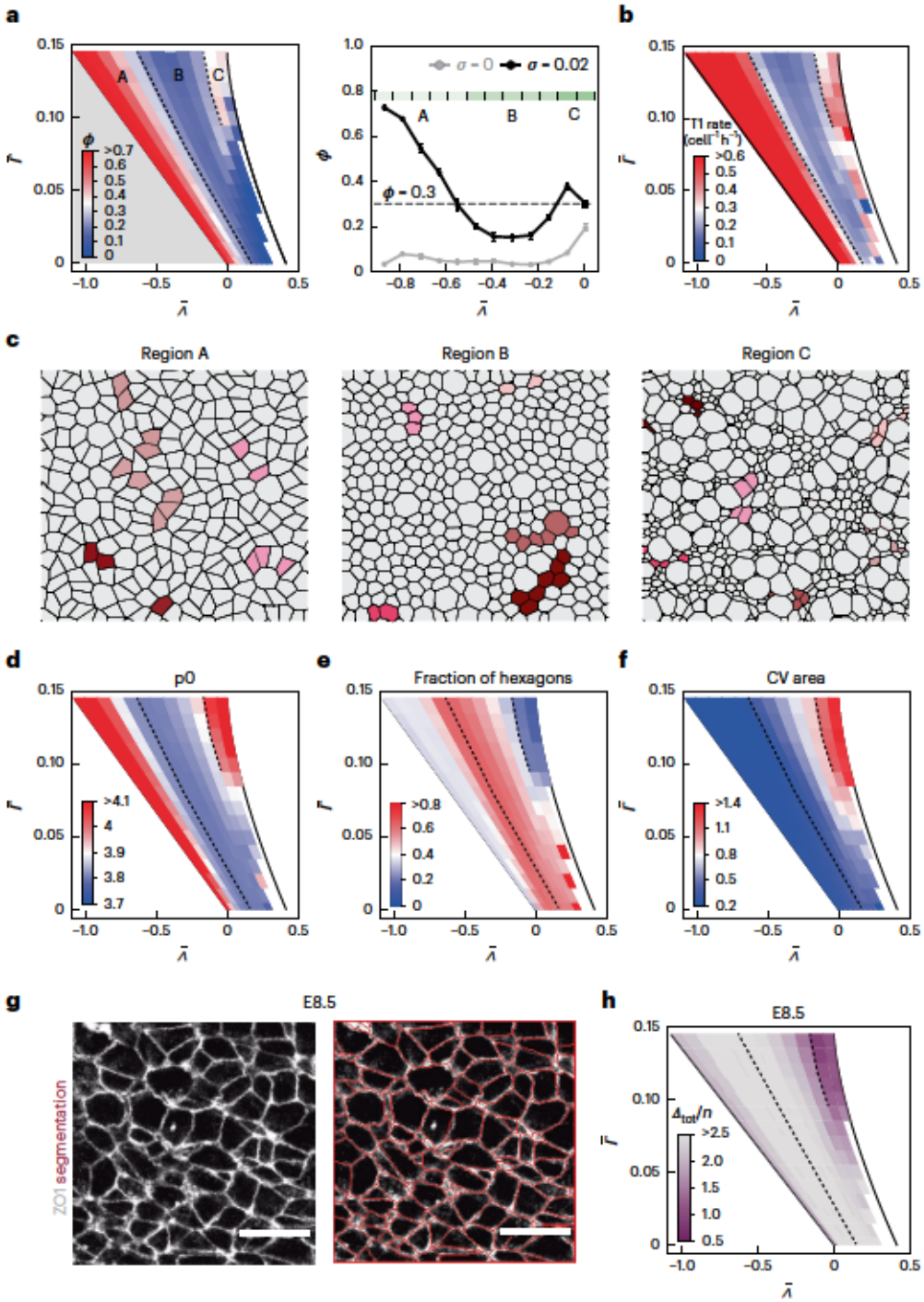

Fig. 3 | Novel regime of extensive cell rearrangements at high tension and contractility in the early-stage neuroepithelium. a, Left: fragmentation coefficient ϕ for different values of $\bar{\Lambda}$ and $\bar{\Gamma}$, $k_p = 0.09\ h^{-1}$, $k_n = 0\ h^{-1}$, $\sigma = 0.02$. The dashed lines correspond to $\phi = 0.3$ and delineate regions A, B and C. The grey region corresponds to the fluid ground state of the model, and the white region denotes an unstable region due to area collapse. Right: also, ϕ for $\bar{\Gamma} = 0.12$. Error bars, standard error; $n = 10$ simulations. The green-shaded regions denote regions A, B and C. Also, ϕ for simulation with no noise ($\sigma = 0$) is shown for comparison. **b**, Mean rate of T1 transition events ($cell^{-1}\,h^{-1}$) across the $(\bar{\Lambda}, \bar{\Gamma})$ parameter space. **c**, Snapshots cropped from simulations of regions A, B and C ($\bar{\Gamma} = 0.12$ and $\bar{\Lambda} = -0.711, -0.393$ and -0.074, respectively). $k_p = 0.09\ h^{-1}$, $k_n = 0\ h^{-1}$. Example clones are displayed in different colours. Note that the shape of the simulated tissues changes over time (Supplementary Videos 2–4). **d**–**f**, Mean cell shape index (**d**), fraction of hexagons (**e**) and coefficient of variation of apical cell areas (**f**) for ten simulations per $(\bar{\Lambda}, \bar{\Gamma})$ parameter set. **g**, Apical view of the epithelium with ZO1 immunostaining. Cell segmentation (red traces). Scale bars, 10 µm. **h**, Difference between the cumulative distribution of cell shape descriptors p_0, ϵ, α, hex, p_{0CV}, ϵ_{CV}, A_{CV} and P_{CV} (Supplementary Table 3) in the simulations and experimental data.

Consistent with the model, our experimental data from EdU- and pH3-labelling experiments show that cells in G2 have similar apical areas to cells in the S phase, but lower than cells in mitosis (Fig. 2c). This argues against a linear increase in cell area during the cell cycle and suggests that the apical cell area rapidly increases during cell division. Time-lapse imaging of neural epithelia expressing membrane GFP confirmed that the subapical cell area increases several times within less than 60 min before cytokinesis (Extended Data Fig. 3). These kinetics

https://doi.org/10.1038/s41567-023-01977-w

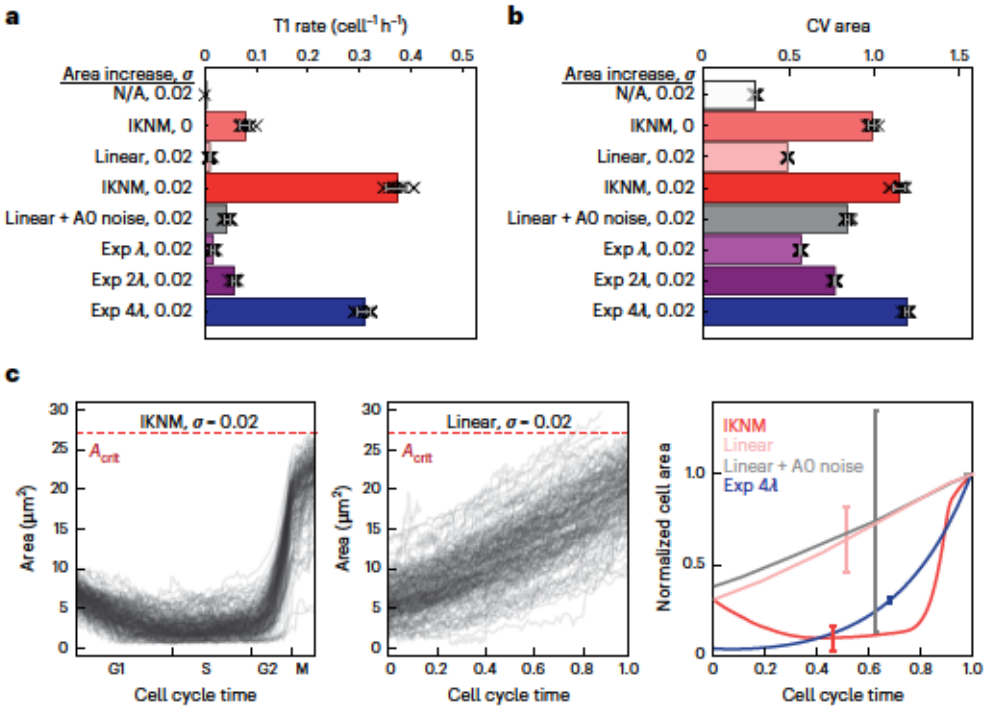

Fig. 4 | Tissue fluidization at high contractility/tension by cell cycle-dependent cell area dynamics. a,**b**, T1 rate (**a**) and mean cell area CV (**b**) for simulations with different modes of cell area increase during the cell cycle and different levels of noise (σ) as indicated. N/A indicates no division; IKNM, cell cycle-dependent target area; linear, linear area increase; linear + A0 noise, linear area increase with A0 noise; exp $n\lambda$, exponential increase with rate $n\lambda$, where n is indicated (Methods). Error bars, standard deviation from ten simulations per condition. Region C ($\tilde{\Lambda} = -0.074$, $\tilde{\Gamma} = 0.12$). Double-sided t-tests for all conditions compared with the default: $P < 0.0001$. **c**, Apical area of 200 randomly selected individual cells in simulations with conditions: IKNM with $\sigma = 0.02$ (left); linear with $\sigma = 0.02$ (middle). The mean cell area during the cell cycle (normalized to the maximum) is shown in **c** (right) for the indicated conditions with $\sigma = 0.02$; sample sizes (number of cells), IKNM ($n = 4{,}625$); linear ($n = 3{,}880$); linear + A0 noise ($n = 3{,}984$); exp 4λ ($n = 12{,}725$). The cell cycle time is normalized from cell birth to cell division (end of mitosis). Error bars, standard deviation.

are similar to the rapid increase in apical area observed before cell division in simulations (Fig. 4c). Altogether, these data support the results of the model and indicate that the kinetics of cell area variability that fluidizes the neuroepithelium is driven by the cell cycle and reflects the changing apicobasal nucleus position during IKNM.

Cell cycle dynamics influence cell rearrangements

Despite the presence of IKNM throughout development, the extent of clone fragmentation declines after E8.5, which raises the question of how this change is regulated. One possibility is that the mechanical parameters (Λ and/or Γ) change over time, such that the tissue ends up in the solid-like region B at later stages. To test this possibility, we performed laser ablation of individual cell junctions in E8.5 and E10.5 neural tubes which expressed ZO1–GFP (Fig. 5a,b, Supplementary Videos 6 and 7 and Methods). We observed no significant difference in the initial recoil velocity of vertices following laser ablation between the two developmental stages, suggesting that the active tension at these stages is similar (Fig. 5c). Further supporting this conclusion, an analysis of the cell shapes in neuroepithelia from E9.5, E10.5 and E11.5 embryos revealed that the experimentally observed cell shapes are consistent with parameter values characteristic of region C (Supplementary Fig. 5). These results suggest that changes in Λ and Γ are not the major factors underlying the change in tissue fluidity over time.

The impact of IKNM on clone fragmentation revealed by our model suggests that the cell division rate could be critical for regulating the extent of cell rearrangements by controlling the level of active stresses that generate fluctuations in the tissue. Between E8.5 and E10.5 of development, the proliferation rate decreases and terminal differentiation commences[18], which lowers the net tissue growth rate by about twofold (Supplementary Fig. 1d). To test whether this could lead to tissue solidification, we lowered the proliferation rate in the vertex model simulations from 0.09 to 0.03 h^{-1}. This resulted in a strong decline in the fragmentation coefficient of clones throughout most of the (Λ,Γ) parameter space (Fig. 5d and Supplementary Fig. 6a). In region C, ϕ declined by about twofold and a corresponding decline in T1 rates was observed (Supplementary Fig. 6b), whereas the cell area CV was reduced to a lesser extent and remained significantly higher than in region B (Supplementary Fig. 6c). This reduction in fragmentation coefficient in the model is reminiscent of the experimentally observed reduction in ϕ (Fig. 1e), suggesting that the decreasing rate of proliferation over time is a key driver of the decline in cell rearrangements.

This analysis predicts that artificially lowering the proliferation rate would lead to a lower level of cell rearrangements. To test this, we induced Confetti clones at E7.5 and then cultured the embryos from E8.5 in the presence of cell cycle inhibitors L-mimosine or aphidicolin for 42 h (Fig. 5e and Supplementary Fig. 7a). As expected, these treatments resulted in reduced mean clone sizes compared with control embryos (Fig. 5f and Supplementary Fig. 7b). Crucially, a comparison of the inhibitor-treated with vehicle-treated control embryos showed that for a given clone size, the number of fragments per clone was significantly reduced in both L-mimosine- and aphidicolin-treated conditions (Fig. 5g and Supplementary Fig. 7c). These results are in agreement with the model prediction and confirm that the proliferation rate has a profound influence on the extent of cell rearrangements in the neuroepithelium.

Besides the rate of proliferation, the overall rate of tissue growth can also be affected by cell loss. From E9.5 to E10.5 of development, terminal differentiation in the pMN domain results in the loss of progenitors from the neuroepithelium and also contributes to lowering

https://doi.org/10.1038/s41567-023-01977-w

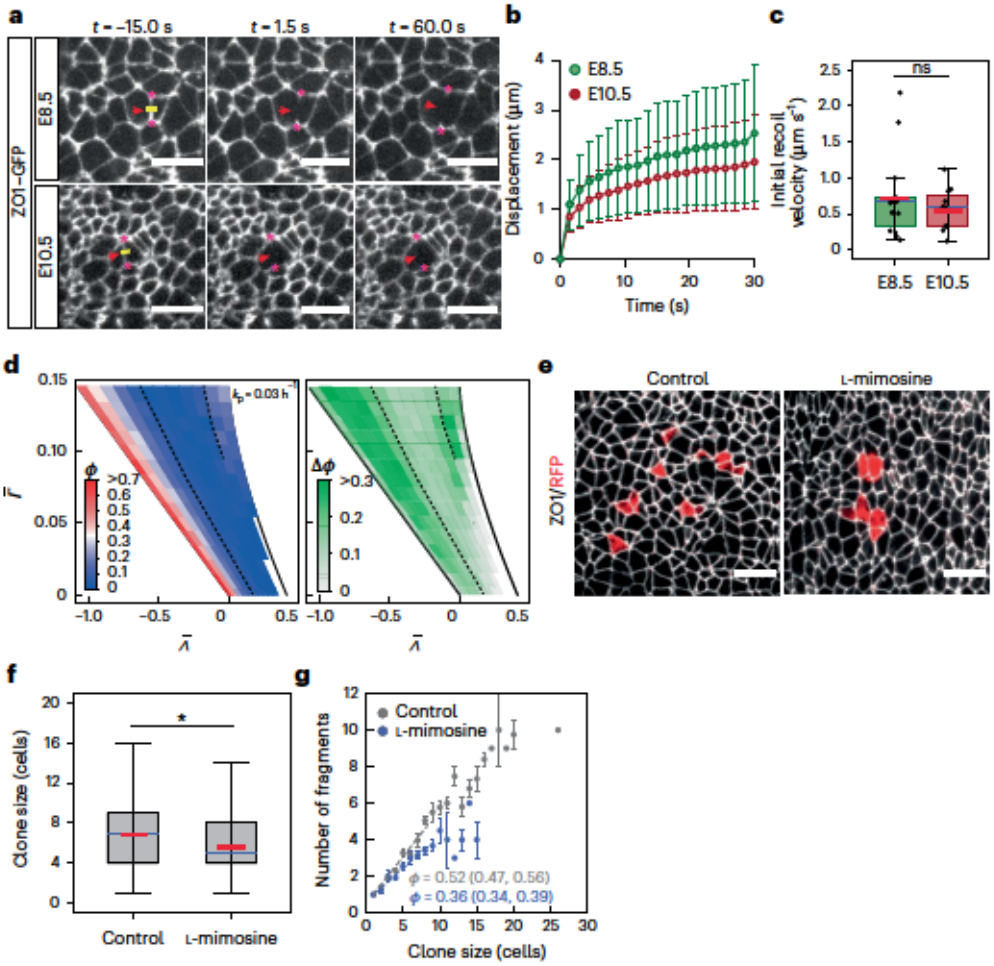

Fig. 5 | Extent of cell rearrangements depends on proliferation rate. a, Laser ablation of apical junctions at E8.5 and E10.5. Apical view, anterior left, dorsal up. The laser cut was performed at $t = 0$ s along the yellow line. The vertex positions (asterisks) were tracked to measure the recoil velocity. Scale bars, 10 μm. **b**, Mean displacement of the vertices over time. Error bars, 95% CI. **c**, Initial recoil velocity of vertices after laser ablation at the indicated stages (Methods). Mann–Whitney test; $P > 0.05$ (with and without outliers). Samples sizes in **b** and **c** are as follows: E8.5 ($n = 14$ ablations); E10.5 ($n = 11$ ablations) (Supplementary Table 1). 25–75 percentile (box), median (blue), mean (red), highest/lowest observations without outliers (whiskers). **d**, Left: fragmentation coefficient (ϕ) for simulations with low proliferation rate $k_p = 0.03\ h^{-1}$. Right: difference in ϕ between high ($0.09\ h^{-1}$; Fig. 3a) and low ($0.03\ h^{-1}$) k_p. **e**, Confetti clones (red) induced at E7.5, embryos cultured from E8.5 for 42 h with vehicle or 210 μM L-mimosine. ZO1 immunostaining, white. Scale bars, 10 μm. **f**, Clone size quantification for **e**. Mann–Whitney test (two sided); $^*P = 0.019$. Box plots as in **c**. Sample sizes are as follows: control ($n = 382$ clones); L-mimosine ($n = 155$ clones). **g**, Mean number of fragments per clone for the experiment in **e** and **f**. Corresponding fragmentation coefficient ϕ (95% CI) was obtained using a linear fit to the data for clones ≤8 cells (dashed lines). Error bars, s.e.m.; sample size as shown in **f**.

the growth rate in this domain[18]. To test the effect of progenitor cell loss by terminal differentiation on cell rearrangements, we modelled cell loss in silico by randomly assigning a zero target area to a fraction of cells (Methods). These simulations showed that cell loss leads to a decrease in clone fragmentation throughout the $(\bar{\lambda}, \Gamma)$ parameter space (Supplementary Fig. 7d). Consistent with this prediction, Confetti clones in the pMN domain have significantly lower fragmentation coefficients than clones in the pD domain, where the differentiation rate is lower in this time interval (Supplementary Fig. 7e). This indicates that in addition to decreasing the proliferation, the increasing terminal differentiation rate also contributes to reduce the extent of cell rearrangements in the neural epithelium over developmental time. Altogether, these observations strongly suggest that the increasing solidification of the mouse neuroepithelium over time is controlled by the observed changes in cell cycle dynamics over time.

Changes in the tissue growth rate have previously been linked to alterations in anisotropic growth and tissue morphogenesis[21,31]. To understand the consequences of reduced proliferation and therefore cell rearrangements for tissue morphogenesis, we treated E8.5 embryos with aphidicolin for 8 h. This resulted in striking changes in the shape of the neural plate, where the treated embryos had an increased ratio of anterior–posterior to dorsoventral length of the neural plate (Supplementary Fig. 8). This result is consistent with previous predictions of our model[21] and indicates that there is an inherent link among tissue fluidity, growth rate and tissue shape.

Conclusion

Morphogenetic processes have been recently linked to transitions in the material properties of tissues[32]. Here we demonstrate that in the mouse neural tube epithelium, there is a significant decline in tissue fluidity around E9.5 of development. Our data suggest that this decline resembles a glass transition, controlled by changes in active stresses within the tissue. We show that in the neuroepithelium, active stresses are generated by IKNM during the cell cycle. Consequently, the proliferation rate determines the extent of cell rearrangement and tissue fluidity.

Previous studies have shown that tissue rheology can change in the absence of noise or fluctuations[3,4,33,34]. In many cases, transitions

in fluidity have been linked to changes in cell density or in mechanical properties, such as cell adhesion, cortical tension and contractility[2,3,5,6,33,35,36]. Tissue fluidity can also decline as a result of T1 delay times or nonlinear junction behaviours[37–39]. By contrast, the role of cell divisions, apart from a few experimental examples[3,10,11] and theoretical predictions[9,40–43], has been largely underappreciated. Slowing down of growth is a hallmark of development and has been measured in multiple tissues[44–46]. Our findings, therefore, suggest that increases in tissue rigidity over developmental time could be a natural consequence of the cell cycle dynamics in many tissues.

IKNM is the characteristic of many epithelia[47–49], and hence, our finding that IKNM fluidizes the epithelia might be relevant to other tissues besides the neural tube. Our analysis indicated that IKNMs exert their effect on cell rearrangements by affecting the apical surface-area kinetics of cells, which results in large cell area variation. Interestingly, in the *Drosophila* wing disc, the presence of smaller-than-normal mutant cells has been shown to induce clonal fragmentation[19]. Yet, in our analysis, imposing 'static' cell area variation did not lead to high clonal fragmentation, indicating a distinct mechanism where the kinetics of cell area changes are crucial for epithelial rearrangements.

Online content

Any methods, additional references, Nature Portfolio reporting summaries, source data, extended data, supplementary information, acknowledgements, peer review information; details of author contributions and competing interests; and statements of data and code availability are available at https://doi.org/10.1038/s41567-023-01977-w.

References

1. Wang, X. et al. Anisotropy links cell shapes to tissue flow during convergent extension. *Proc. Natl Acad. Sci. USA* **117**, 13541–13551 (2020).
2. Mongera, A. et al. A fluid-to-solid jamming transition underlies vertebrate body axis elongation. *Nature* **561**, 401–405 (2018).
3. Petridou, N. I., Grigolon, S., Salbreux, G., Hannezo, E. & Heisenberg, C. P. Fluidization-mediated tissue spreading by mitotic cell rounding and non-canonical Wnt signalling. *Nat. Cell Biol.* **21**, 169–178 (2019).
4. Park, J. A. et al. Unjamming and cell shape in the asthmatic airway epithelium. *Nat. Mater.* **14**, 1040–1048 (2015).
5. Zhou, J., Kim, H. Y. & Davidson, L. A. Actomyosin stiffens the vertebrate embryo during crucial stages of elongation and neural tube closure. *Development* **136**, 677–688 (2009).
6. Kim, S., Pochitaloff, M., Stooke-Vaughan, G. A. & Campàs, O. Embryonic tissues as active foams. *Nat. Phys.* **17**, 859–866 (2021).
7. Bi, D., Lopez, J. H., Schwarz, J. M. & Manning, M. L. A density-independent rigidity transition in biological tissues. *Nat. Phys.* **11**, 1074–1079 (2015).
8. Bi, D., Yang, X., Marchetti, M. C. & Manning, M. L. Motility-driven glass and jamming transitions in biological tissues. *Phys. Rev. X* **6**, 021011 (2016).
9. Ranft, J. et al. Fluidization of tissues by cell division and apoptosis. *Proc. Natl Acad. Sci. USA* **107**, 20863–20868 (2010).
10. Devany, J., Sussman, D. M., Yamamoto, T., Manning, M. L. & Gardel, M. L. Cell cycle–dependent active stress drives epithelia remodeling. *Proc. Natl Acad. Sci. USA* **118**, e1917853118 (2021).
11. Firmino, J., Rocancourt, D., Saadaoui, M., Moreau, C. & Gros, J. Cell division drives epithelial cell rearrangements during gastrulation in chick. *Dev. Cell* **36**, 249–261 (2016).
12. Matoz-Fernandez, D. A., Martens, K., Sknepnek, R., Barrat, J. L. & Henkes, S. Cell division and death inhibit glassy behaviour of confluent tissues. *Soft Matter* **13**, 3205–3212 (2017).
13. Sausedo, R. A., Smith, J. L. & Schoenwolf, G. C. Role of nonrandomly oriented cell division in shaping and bending of the neural plate. *J. Comp. Neurol.* **381**, 473–488 (1997).
14. Williams, M., Yen, W., Lu, X. & Sutherland, A. Distinct apical and basolateral mechanisms drive planar cell polarity-dependent convergent extension of the mouse neural plate. *Dev. Cell* **29**, 34–46 (2014).
15. Nishimura, T., Honda, H. & Takeichi, M. Planar cell polarity links axes of spatial dynamics in neural-tube closure. *Cell* **149**, 1084–1097 (2012).
16. Zong, H., Espinosa, J. S., Su, H. H., Muzumdar, M. D. & Luo, L. Mosaic analysis with double markers in mice. *Cell* **121**, 479–492 (2005).
17. Hippenmeyer, S. et al. Genetic mosaic dissection of Lis1 and Ndel1 in neuronal migration. *Neuron* **68**, 695–709 (2010).
18. Kicheva, A. et al. Coordination of progenitor specification and growth in mouse and chick spinal cord. *Science* **345**, 1254927 (2014).
19. Ramanathan, S. P., Krajnc, M. & Gibson, M. C. Cell-size pleomorphism drives aberrant clone dispersal in proliferating epithelia. *Dev. Cell* **51**, 49–61.e4 (2019).
20. Dekoninck, S. et al. Defining the design principles of skin epidermis postnatal growth. *Cell* **181**, 604–620.e22 (2020).
21. Guerrero, P. et al. Neuronal differentiation influences progenitor arrangement in the vertebrate neuroepithelium. *Development* **146**, dev176297 (2019).
22. Farhadifar, R., Röper, J.-C., Aigouy, B., Eaton, S. & Jülicher, F. The influence of cell mechanics, cell-cell interactions, and proliferation on epithelial packing. *Curr. Biol.* **17**, 2095–2104 (2007).
23. Curran, S. et al. Myosin II controls junction fluctuations to guide epithelial tissue ordering. *Dev. Cell* **43**, 480–492.e6 (2017).
24. Staple, D. B. et al. Mechanics and remodelling of cell packings in epithelia. *Eur. Phys. J.* **33**, 117–127 (2010).
25. Keys, A. S., Abate, A. R., Glotzer, S. C. & Durian, D. J. Measurement of growing dynamical length scales and prediction of the jamming transition in a granular material. *Nat. Phys.* **3**, 260–264 (2007).
26. Sussman, D. M., Paoluzzi, M., Cristina Marchetti, M. & Lisa Manning, M. Anomalous glassy dynamics in simple models of dense biological tissue. *EPL* **121**, 36001 (2018).
27. Kursawe, J., Baker, R. E. & Fletcher, A. G. Approximate Bayesian computation reveals the importance of repeated measurements for parameterising cell-based models of growing tissues. *J. Theor. Biol.* **443**, 66–81 (2018).
28. Ishihara, S. & Sugimura, K. Bayesian inference of force dynamics during morphogenesis. *J. Theor. Biol.* **313**, 201–211 (2012).
29. Butler, M. B. et al. Rho kinase-dependent apical constriction counteracts M-phase apical expansion to enable mouse neural tube closure. *J. Cell Sci.* **132**, jcs230300 (2019).
30. Nikolopoulou, E., Galea, G. L., Rolo, A., Greene, N. D. E. & Copp, A. J. Neural tube closure: cellular, molecular and biomechanical mechanisms. *Development* **144**, 552–566 (2017).
31. Leise, W. F. & Mueller, P. R. Inhibition of the cell cycle is required for convergent extension of the paraxial mesoderm during *Xenopus* neurulation. *Development* **131**, 1703–1715 (2004).
32. Petridou, N. I. & Heisenberg, C. Tissue rheology in embryonic organization. *EMBO J.* **38**, e102497 (2019).
33. Barriga, E. H., Franze, K., Charras, G. & Mayor, R. Tissue stiffening coordinates morphogenesis by triggering collective cell migration in vivo. *Nature* **554**, 523–527 (2018).
34. Yan, L. & Bi, D. Multicellular rosettes drive fluid-solid transition in epithelial tissues. *Phys. Rev. X* **9**, 11029 (2019).
35. Garcia, S. et al. Physics of active jamming during collective cellular motion in a monolayer. *Proc. Natl Acad. Sci. USA* **112**, 15314–15319 (2015).
36. David, R. et al. Tissue cohesion and the mechanics of cell rearrangement. *Development* **141**, 3672–3682 (2014).

37. Erdemci-Tandogan, G. & Lisa Manning, M. Effect of cellular rearrangement time delays on the rheology of vertex models for confluent tissues. *PLoS Comput. Biol.* **17**, e1009049 (2021).
38. Das, A., Sastry, S. & Bi, D. Controlled neighbor exchanges drive glassy behavior, intermittency, and cell streaming in epithelial tissues. *Phys. Rev. X* **11**, 041037 (2021).
39. Krajnc, M., Stern, T. & Zankoc, C. Active instability and nonlinear dynamics of cell-cell junctions. *Phys. Rev. Lett.* **127**, 198103 (2021).
40. Krajnc, M., Dasgupta, S., Ziherl, P. & Prost, J. Fluidization of epithelial sheets by active cell rearrangements. *Phys. Rev. E* **98**, 022409 (2018).
41. Czajkowski, M., Sussman, D. M., Marchetti, M. C. & Manning, M. L. Glassy dynamics in models of confluent tissue with mitosis and apoptosis. *Soft Matter* **15**, 9133–9149 (2019).
42. Nematbakhsh, A. et al. Multi-scale computational study of the mechanical regulation of cell mitotic rounding in epithelia. *PLoS Comput. Biol.* **13**, e1005533 (2017).
43. Malmi-Kakkada, A. N., Li, X., Samanta, H. S., Sinha, S. & Thirumalai, D. Cell growth rate dictates the onset of glass to fluidlike transition and long time superdiffusion in an evolving cell colony. *Phys. Rev. X* **8**, 21025 (2018).
44. Lange, C. & Calegari, F. Cdks and cyclins link G_1 length and differentiation of embryonic, neural and hematopoietic stem cells. *Cell Cycle* **9**, 1893–1900 (2010).
45. Wartlick, O. et al. Dynamics of Dpp signaling and proliferation control. *Science* **331**, 1154–1159 (2011).
46. Marcon, L., Arqués, C. G., Torres, M. S. & Sharpe, J. A computational clonal analysis of the developing mouse limb bud. *PLoS Comput. Biol.* **7**, e1001071 (2011).
47. Strzyz, P. J., Matejcic, M. & Norden, C. Heterogeneity, cell biology and tissue mechanics of pseudostratified epithelia: coordination of cell divisions and growth in tightly packed tissues. *Int. Rev. Cell Mol. Biol.* **299**, 89–118 (2016).
48. Cammarota, C. M. & Bergstralh, D. Cell division: interkinetic nuclear… mechanics. *Curr. Biol.* **30**, R759–R761 (2020).
49. Kirkland, N. J. et al. Tissue mechanics regulate mitotic nuclear dynamics during epithelial development. *Curr. Biol.* **30**, 2419–2432.e4 (2020).

Methods

Experiments

Mouse strains and generation of clones. All the animal procedures were performed in accordance with the relevant regulations and were approved under the license BMWFW-66.018/0006-WF/V/3b/2016 from the Austrian Bundesministerium für Wissenschaft, Forschung und Wirtschaft. The following strains were previously described: MADM-11^{TG} and MADM-11^{GT} (ref. 17), Rosa26–Confetti (Brainbow-2.1 (ref. 50)), Sox2–CreERT2 (ref. 51), mTmG (ref. 52), R26–ZO1–GFP (ref. 53), Rosa26–tdTomato (ref. 54). To generate MADM clones in MADM$^{TG/GT}$ trans-heterozygous Sox2–CreERT2-expressing embryos, MADM-11$^{TG/TG}$ mice were bred to MADM-11$^{GT/GT}$ and Sox2–CreERT2/+, and pregnant females were injected with 3 mg per mouse of tamoxifen. To generate Confetti clones, heterozygous Sox2–CreERT2 mice were bred to heterozygous Rosa26–Confetti and pregnant mothers were injected with 0.75 mg per mouse of tamoxifen. Tamoxifen stock was prepared fresh in sunflower oil.

The first time point where we observe labelled cells is 8 h after tamoxifen injection (Supplementary Fig. 1b), reflecting the time it takes for the nuclear translocation of Cre and subsequent onset of reporter expression. Thus, the time of Cre activity in the 24 h tracing experiments (Fig. 1) is considered to be 16 h.

Immunohistochemistry, EdU incorporation and imaging. For E9.5 and later stages, embryos were bisected along the roof plate before fixation and along the floor plate before immunostaining. Embryos were fixed in 4% paraformaldehyde and subsequently in methanol. Primary and secondary antibody incubations were 24 h each. Washes in phosphate-buffered saline with 0.1% Tween were 10 h each. The brachial region was flat mounted with grease spacers between slide and coverslip. Primary antibodies used were mouse anti-ZO1 (Invitrogen, 1:90), goat anti-Olig2 (R&D Systems, 1:100), sheep anti-GFP (AbD Serotec, 1:1,000), rabbit anti-RFP (Rockland, 1:2,000), mouse anti-Nkx2.2 (DSHB, 1:20), rat anti-pH3 (Sigma,1:1,000), goat anti-SOX2 (R&D Systems,1:100), rabbit anti-Brachyury (Abcam, 1:100). Secondary antibodies used were donkey anti-mouse Alexa Fluor 647 and donkey anti-goat FITC (Jackson Immuno, 1:250), donkey anti-rabbit Cy3 and donkey anti-rat Cy3 (Jackson Immuno, 1:1,000), donkey anti-sheep FITC (Jackson Immuno, 1:250).

For MADM clone analysis, embryos were immunostained against ZO1, RFP, GFP and Nkx2.2. Clones located within 25 µm dorsal to the Nkx2.2 domain boundary were considered to be pMN clones. For Confetti clone analysis, embryos were immunostained against ZO1 and Olig2. To stain actin filaments, the following steps of the protocol were modified: embryos were fixed in 4% paraformaldehyde overnight, methanol fixation was omitted and Alexa Fluor 488 Phalloidin (Thermo Fisher Scientific, 1:100) was added together with the secondary antibody.

For EdU-labelling experiments, Sox2–CreERT2 mice were bred to ROSA26–tdTomato. Pregnant mice were intraperitoneally injected with 3 mg tamoxifen at E6.5 and with 0.5 mg EdU in phosphate-buffered saline (stock, 2.5 mg ml^{-1}) on the day of the experiment. For S-phase labelling, mice were sacrificed 20 min after EdU injection at E8.5 and 30 min after injection at E10.5. To label cells in G2, mice were sacrificed 2 h after EdU injection. The embryos were dissected, fixed and immunostained against ZO1 and RFP, as described above. Subsequently, the incorporated EdU was detected using the Alexa Fluor 488 Click-iT EdU imaging kit and protocol (Invitrogen, C10337).

Imaging was performed using a 40×/1.3 numerical aperture oil objective on an LSM880 inverted confocal microscope. Images of the apical surface capturing the entire dorsoventral length of the epithelium were acquired through tile scanning with *Z* slices 0.8 µm apart. The tiles were configured in the form of a grid and overlapped 10%. Subsequently, the tiles were stitched using the BigStitcher plugin in Fiji version 2.9 (ref. 55).

Mouse embryo culture and inhibitor treatments. To combine clone tracing with mouse embryo culture and inhibitor treatments, heterozygous Sox2–CreERT2 mice were bred to Rosa26–Confetti. To induce sparse labelling (see the 'Clone identification and fragmentation coefficient estimation' section), pregnant mothers were injected with 0.75 mg per mouse of tamoxifen at E7.5. After 24 h, at E8.5, embryos were dissected and cultured with their yolk sac intact in temperature-controlled roller culture[56] (5% CO_2 and 20% O_2). The embryo culture medium consisted of 1:1 rat serum: dissection medium[57] (Gibco DMEM/F12 without phenol red (Thermo Fisher), 10% Gibco foetal bovine serum (Thermo Fisher), 1× penicillin–streptomycin (Sigma)). To perturb proliferation, embryos were cultured in the presence of 210 µM L-mimosine (Sigma) or 800 nM aphidicolin (Sigma) for 42 h. Calyculin A (Merck Millipore) was used at a final concentration of 0.6 nM for 42 h of culture. After culture, the embryos were harvested and processed for imaging, as described above.

Laser ablation. Embryos heterozygous or homozygous for R26–ZO1–GFP were collected at E8.5 and E10.5 of development. To perform laser ablation, whole E8.5 embryos or dissected flat-mounted E10.5 brachial neural tubes were immobilized for live imaging in glass-bottom dishes (Ibidi) in embryo culture medium (see 'Mouse embryo culture and inhibitor treatments' section) supplemented with 8 mg ml^{-1} fibrinogen (Millipore). Thrombin (0.5 U µl^{-1}, Sigma Aldrich) was added to form a fibrin gel[18]. The samples were kept in an environmental chamber with 5% CO_2 at 37 °C. Laser ablation was performed on an Andor spinning-disc system with inverted Axio Observer Z1, C-Apochromat 63×/1.2 water-immersion objective (Carl Zeiss) using a 355 nm pulsed UV-A nanolaser (Teem Photonics) at 1.8–1.9% laser power with 25 pulses (2 shots µm^{-1}) at 1,000 Hz. Junction ablation was performed approximately at the centre of the cell edge between two vertices along a 2 µm line oriented along the A–P axis. Edges oriented dorsoventrally and located at intermediate dorsoventral positions were selected for the experiment. Images were collected with 250 ms exposure time and frame rate of 1.5 s. To determine the recoil velocities, the positions of the vertices were manually tracked over time in Fiji. The initial recoil velocity was defined as the distance between the vertices at t1 minus the distance at t0 (before the cut), divided by the time interval between t0 and t1 (1.5 s).

Live imaging. To image the apical surface of the neuroepithelium at the level of tight junctions, embryos heterozygous or homozygous for ZO1–EGFP were collected at E8.5 and E10.5. Whole E8.5 embryos and bisected E10.5 brachial neural-tube regions were positioned on 35 mm glass-bottom dishes (Ibidi) in an embryo culture medium (see the 'Mouse embryo culture and inhibitor treatments' section) and immobilized with coverslips on silicon grease spacers. Imaging of the ZO1–GFP-labelled apical surfaces was performed on an inverted LSM800 confocal microscope using a 40×/1.2× water objective. The *Z* stacks were acquired with *Z* slices 0.75 µm apart for a period of about 1–2 h.

Imaging of the cell membranes (marked by membrane GFP) at the subapical level was performed using E10.5 Sox2–CreERT2/+, mTmG/+ embryos of mothers injected with 1 mg tamoxifen 24 h before dissection. Brachial neural-tube regions were dissected and prepared for imaging the same way as that for laser ablation experiments. The *Z* stacks were acquired with *Z* slices 0.7 µm apart.

Data analysis

Clone identification and fragmentation coefficient estimation. Images were processed in Fiji. Labelled progenitor cells were manually marked at their apical surface at the level of ZO1 staining. Fragments were defined as groups of adjacent cells that share an edge or a vertex. Clones were defined as groups of labelled progenitor cells in close proximity of each other (<25 µm to the nearest labelled cell).

In the case of MADM clones, G2 recombination followed by the X segregation of chromosomes in mitosis produces a GFP- and RFP-expressing daughter cell (Fig. 1a). Both GFP- and RFP-expressing cells were included in defining a clone. G2–Z segregation produces an unlabelled and a GFP/RFP-coexpressing daughter cell. G1 recombination produces a GFP/RFP-coexpressing cell. In our dataset, we found an increasing proportion of GFP/RFP-coexpressing cells over time (Supplementary Fig. 1a), which correlates with the increasing relative G1 duration over time[18]. This suggests that the majority of GFP/RFP-coexpressing clones result from G1 recombination. We, therefore, also included GFP/RFP-coexpressing clones in the analysis. MADM clones and the fragments they contain were manually identified from images.

In the case of Confetti clones, only the RFP, YFP and CFP reporters, which can be detected at the apical surface, were used for the analysis, whereas clones labelled by the nuclear GFP were excluded. The sparseness of labelling in the experiments was as follows: 322 ± 38, 366 ± 39 and 235 ± 36 cells mm^{-2} for CFP, RFP and YFP, respectively (mean ± standard error of the mean (s.e.m.) for 54 images is given). To identify Confetti clones, the cell coordinates were recorded and subsequently analysed using a custom-built Python script, similar to the one reported elsewhere[18]. CFP, RFP and YFP channels were separately analysed. The labelled cells were assigned to the same fragment if the distance between them was <5 µm and to the same clone if they were <25 µm apart. These assignments were consistent with the visual identification of fragments and clones, except in occasional cases where the clone size was unreasonably large. Labelled postmitotic neurons that have delaminated from the neural epithelium were excluded from the analysis.

We determined the fragmentation coefficient ϕ by fitting $f = \phi s + b$ to the respective dataset, where f is the mean number of fragments for a given clone size, s is the size of the clone in cells and b is an offset parameter that is chosen in such a way that the line crosses through the point (1, 1), reflecting the fact that single-cell clones have one fragment by definition. For MADM clones analysed 24 h after tamoxifen injection, reliable statistics could be obtained for clones with four cells or less; hence, only these clone sizes were used for estimating ϕ. In mouse embryo culture experiments, Confetti clones were analysed 64 h after tamoxifen injection. In this case, reliable statistics could be obtained for clone sizes of ≤8 cells and these were used to estimate ϕ.

Growth rate estimation. The growth rate of MADM clones k_g was inferred from the mean clone size s as $k_g = \ln(s)/\Delta t$, where $\Delta t = 16$ h is the time interval of Cre activity in the experiments (Supplementary Fig. 1b–d and Methods).

Spread and anisotropy of clones. To estimate the spread of clones, the coordinates of cell centres in a clone were used to determine the clone centroid. The maximum spread of the clone was quantified as the distance between the clone centroid and furthest cell centre. To estimate the mean maximum spread for a given developmental stage, clones of all sizes were taken into account (including single-cell clones).

Clone anisotropy was quantified by drawing a bounding rectangle around the clone, using the apical cell outlines, marked by ZO1, to demarcate the cells. Images are always oriented so that the vertical axis is aligned with the tissue D–V axis. The aspect ratio of the clone is then given by the D–V to A–P side lengths of the bounding rectangle. Note that quantifying the clone shape at the apical surface, rather than the cell bodies or nuclei, avoids potential artefacts of tissue mounting, where the clone shape could be affected by the misalignment of the apical and basal surfaces of the neural epithelium.

To quantify the self-overlap function in simulations, we adapt the definition from other work[25,26] for a growing tissue. The self-overlap function is defined as $Q_s(t) = \frac{1}{N}\sum_{k=1}^{N} w(|\tilde{r}_k(t) - \tilde{r}_k(0)|)$, where $\tilde{r}_k(t)$ is the position of the centre of mass of the kth cell at time t, w is a window function that gives 1 for $|\tilde{r}_k(t) - \tilde{r}_k(0)| \le \tilde{R}_{cell}$ and 0 otherwise, and N is the number of cells. The $\tilde{R}_{cell}$ value is the characteristic length that corresponds to the initial cell radius in the reference frame defined below. To correct for growth, we consider every cell trajectory in a reference frame that is centred at the initial position of that cell and normalized by the fastest growing dimension. In practice, we apply the following two steps: (1) for every newborn cell with position (r_{D-V}, r_{A-P}) at time $t = 0$, we shift the corresponding cell trajectory to start in $(r_{D-V}, r_{A-P}) \to (0, 0)$; (2) we then normalize the cell position over time by dividing its position by the D–V and A–P extensions of the growing tissue with the correction from the anisotropic growth, that is, $\tilde{r}_k(t) = \left(\frac{r_{D-V}}{L_{D-V}}, \frac{r_{A-P}}{L_{A-P}}\left\langle\frac{L_{A-P}}{L_{D-V}}\right\rangle\right)$, where L_{D-V} and L_{A-P} are the respective tissue dimensions at time t, and $\left\langle\frac{L_{A-P}}{L_{D-V}}\right\rangle$ is the average A–P/D–V ratio for a given simulation. The $\tilde{R}_{cell}$ value is defined as $\frac{\sqrt{\langle A\rangle}}{2}/L_{D-V}$, where $\langle A\rangle$ is the average cell area at time $t = 0$, and L_{D-V} is taken at $t = 0$.

Segmentation of cell shapes. Apical surfaces immunostained for ZO1 of the E8.5, E9.5, E10.5 and E11.5 neural tubes were segmented using the Tissue Analyzer plugin[58] in Fiji. The cell outlines were automatically identified and manually checked for correctness. This plugin provided the description of a polygonal mesh including the vertices and edges of cell outlines as well as the number and identity of cell neighbours. The cell area was calculated using a standard formula for the area of the n-gon and cell perimeter as a sum of the length of polygon edges. The cell elongation was calculated as done elsewhere[21,27].

In the EdU- and pH3-labelling experiments, the distance between the nucleus centre and ZO1-labelled junctional level was measured using Imaris 9.1 (Oxford Instruments) from confocal Z stacks. To associate EdU-labelled nuclei with the corresponding apical surfaces of cells, cells that expressed cytosolic tdTomato and therefore allowed tracing the cell body were used for the analysis.

Cell areas in the EdU experiment (Fig. 2) and membrane-GFP-expressing embryos in live imaging (Extended Data Fig. 3) were quantified using Imaris 9.1. For this, the cells were segmented using a watershed function. Subsequently, the cell area was estimated from the segmented cell volume within the relevant Z slice divided by the voxel depth. For the EdU experiments, the relevant Z slice is the one marked by the ZO1 expression. For the membrane-GFP-expressing embryos, the cell areas were quantified at the Z position corresponding to 2.1–2.8 µm below the apical cell membrane.

To quantify the variation in edge length over time, time-lapse images of ZO1–GFP-expressing neural tubes were segmented in Fiji in the same way as the fixed images. To avoid large fluctuations in edge length that arise as a result of cell divisions, T1 transitions or segmentation errors, we only quantified the edges that could be tracked throughout the duration of the experiment and were at least one cell away from the cells undergoing large fluctuations.

Simulations

Vertex model description and implementation. The vertex model used in this study is based on another work[21] and was implemented here using Python 3.7. Briefly, the following energy function is minimized in every simulation step:

$$E = \sum_{\alpha} \frac{K_\alpha}{2}\left(A_\alpha - A_\alpha^0(t)\right)^2 + \sum_{ij} \Lambda_{ij} l_{ij} + \sum_{\alpha} \frac{\Gamma_\alpha}{2} L_\alpha^2 \qquad (1)$$

where $\alpha = 1, \ldots, N_c$ enumerates all the cells; $i = 1, \ldots, N_v$ enumerates all the vertices; K_α is the elasticity coefficient; A_α is the area of cell α; $A_\alpha^0(t)$ is the preferred area of cell α at time t; Λ_{ij} is the line-tension coefficient associated with the cell edge between i and j of length l_{ij}; and Γ_α is the contractility coefficient of cell α with perimeter L_α. We assume that the parameters are the same for each cell ($K_\alpha = K, \Gamma_\alpha = \Gamma$) and for each edge ($\Lambda_{ij} = \Lambda$) if no noise in the line tension is considered. The preferred cell area $A_\alpha^0(t)$ is a piecewise linear function reflecting the effect of IKNM

on the apical cell area in the four phases of the cell cycle (G1, S, G2 and M; also see below). Adopting the same notation as previous studies[21,22], we use the normalized parameters as $\bar{\Lambda} = \frac{\Lambda}{K(A^0)^{3/2}}$ and $\bar{\Gamma} = \frac{\Gamma}{KA^0}$, where A^0 is the average target area during the cell cycle.

The motion of vertices is determined from the first-order kinetics: $\frac{dr_i}{dt} = -\frac{1}{\mu}\frac{\partial E}{\partial r_i}$, where r_i is position of vertex i and μ is the drag coefficient. Tissue growth was considered to be anisotropic with drag coefficients μ' and μ'' in the D–V and A–P directions, respectively[21].

The following changes were made in the current version of the model:

Implementation of junctional noise. We considered that fluctuations in the internal line tension follow an Ornstein–Uhlenbeck process, namely, $\frac{d\Lambda_{ij}}{dt} = -\frac{1}{\tau}\left(\Lambda_{ij} - \Lambda_{ij}^0\right) + \xi_{ij}(t)$, where $\xi_{ij}(t)$ is white, uncorrelated noise with $\langle \xi_{ij}(t) = 0 \rangle$ and $\langle \xi_{ij}(t)\,\xi_{kl}(t') \rangle = \frac{2\sigma^2}{\tau}\delta_{ik}\delta_{jl}\delta(t-t')$. We used the following discretization[23]:

$$\Lambda_{ij}(t+\Delta t) = \Lambda_{ij}(t) - \frac{\Delta t}{\tau}\left(\Lambda_{ij}(t) - \Lambda_{ij}^0\right) + \sqrt{\frac{2\sigma^2\Delta t}{\tau}}\overline{\xi_{ij}}(t) \qquad (2)$$

where Δt is a time step used in the simulation, τ is the line-tension correlation time, σ is the intrinsic line-tension deviation, $\Lambda_{ij}^0 = \Lambda$ is a reference line tension that corresponds to the line tension without noise and $\overline{\xi_{ij}}(t)$ is drawn from the Gaussian distribution $N(0,1)$.

Implementation of T1 and T2 transitions. The T1 transition is defined elsewhere[21]. In particular, when an edge between two neighbouring cells is shorter than a predefined small length l_{T1}, this edge is replaced with a new edge that is perpendicular to the old edge and has a length $l_{new} = 1.01 l_{T1}$. Using this definition, we observed that for negative line tension or in the presence of line-tension fluctuations, immediately after a T1 transition, the new edge can shrink instead of extending, thus leading to a reverted T1 transition. This can occur multiple times at a given edge, and hence, we call this an oscillatory T1 transition.

One strategy to partly mitigate the occurrence of oscillatory T1 transitions is to increase the l_{new}/l_{T1} ratio[59]. However, particularly in region A, the oscillatory T1 transitions are generic and increasing l_{new}/l_{T1} does not result in decreasing the number of oscillatory T1 transitions. Therefore, we approached this instead by keeping track of the oscillatory T1 transitions and subtracting them from the overall count of T1 events in our statistics. More specifically, we track how many T1 transitions occurred for every edge, using the dictionary data structure in Python. If repeated T1 transitions occurred n_{T1} times between time t_0 and t_{nT1}, their contribution to the T1 unique rate, namely, $T1_{UNQ}$, was considered to be $1/n_{T1}$ for times between t_0 and t_{nT1}.

T2 transitions are defined in another work[21]. In particular, cells in which the area becomes very small have shrinking edges. This results in sequential T1 transitions, which finally lead to a double-sided cell with zero area. Such cells are removed from the simulation by merging the two vertices that delimit the double-sided cell into one vertex. The last T1 transition that results in a double-sided cell is counted as a T2 transition, and is not included in the overall number of T1 transition events. All the T1, $T1_{UNQ}$ and T2 rates are estimated in time windows of $\Delta t = 2$ h by the dividing number of respective events with the average number of cells in this time window. The T1 rate reported in the main text as well as in Figs. 3b and 4a and Supplementary Fig. 6b is defined as the T1 unique rate.

Cell removal from the tissue through differentiation is implemented similar to another work[21] with the additional requirement that if the cell was randomly selected for differentiation, the line-tension coefficients Λ_{ij} for this cell are no longer fluctuating and have assigned a positive value of $\Lambda_{ij} = 0.2$, which fosters shortening of all the edges of this cell.

Cell lineage tracing. To efficiently analyse in silico clonal populations, the complete information about cell lineage, that is, daughter-cell identifiers and division times, are stored. For the analysis of clone fragmentation in silico, we used all the clones per simulation and ten independent simulations per parameter set.

Parameters of the model. The used parameters are summarized in Supplementary Table 2. The default proliferation rate in the model $k_p = 0.09\ h^{-1}$ has been chosen to match with the experimentally observed tissue growth rate (Supplementary Fig. 1d): it results in mean sizes of simulated clones of three to four cells (depending on the exact value of $\bar{\Lambda}$ and $\bar{\Gamma}$), which is similar to the clone sizes observed in injection at E8.5 (Supplementary Fig. 1c). The specific proliferation (k_p) and differentiation (k_n) rates used in the simulations are given in the corresponding figure legends. The critical area A_c has been set to 27 μm² so that the range of cell areas in the simulations (Supplementary Fig. 2a) is comparable with the range of areas measured in the experiments (Supplementary Fig. 5b). Furthermore, $A_c = 27$ μm² results in a very close agreement between the mean edge length in simulations and in the E10.5 experimental data (1.47 ± 0.01 μm and 1.43 ± 0.01 μm (mean ± s.e.m.), respectively; Fig. 2d). The length of a simulation step $\Delta t = 0.29$ s has been chosen such that the model has high temporal resolution and includes on the order of 10^5 simulation points per cell cycle (10^5 points correspond to 8 h). The units of force are arbitrary. Every data point across the $(\bar{\Lambda}, \bar{\Gamma})$ parameter space was obtained by pooling together cells from ten independent simulations for a given set of parameters $(\bar{\Lambda}, \bar{\Gamma}, k_p, k_n)$.

Vertex model initialization and in silico clone tracing. The vertex model is initiated with a regular hexagonal lattice of ten rows with ten cells per row. In the initial simulation phase, the tissue grows for 16 h with $\bar{\Lambda} = -0.184$, $\bar{\Gamma} = 0.07$, $k_p = 0.09\ h^{-1}$, $k_n = 0\ h^{-1}$ and $\sigma = 0$. In our default simulations, we used distinct drag viscosities for the D–V and A–P dimensions, resulting in rectangular tissues with A–P/D–V length ratios of <1 at the end of the simulations (Supplementary Videos 2–4). After the initial simulation phase, the number of cells is 460 ± 19 (mean ± standard error), the time is set to 0 and the parameters are modified to the target simulation parameters. The tissue is then allowed to grow with the target simulation parameters for 8 h. Subsequently, clones are labelled and clonal populations of cells are tracked for 16 h.

Analysis of cell area heterogeneity and kinetics. To investigate the area variability of cells undergoing a T1 transition, we defined quadruplets of neighbouring cells, designated as A, B, C and D, where A and B share a common edge and C and D do not (Supplementary Fig. 4c). We further define the cell names based on the cell area such that area of A < area of B and area of C < area of D. If the common edge between A and B shrinks below l_{T1}, a T1 transition takes place, as a result of which A and B are no longer adjacent, whereas C and D become new neighbours. For comparison, 'random' quadruplets are generated by randomly finding A and B cells separated by a common edge, and finding cells C and D that are adjacent to A and B, but not to each other. Note that because the polygonal mesh has no rosettes, that is, each vertex has three edges associated with it, the assignment of a quadruplet to an edge is unique.

Cell area kinetics during cell cycle and cell division. The iKNM is approximated as a linear combination of two terms, one corresponding to a linear increase in cell volume and the other interpolating for the change in apical cell surface as a function of the age of a cell:

$$A_\alpha^0(t) = \frac{1}{2}(g_\alpha \Delta t + 1)(\rho_\alpha(\Delta t)^2 + 1) \qquad (3)$$

where g_α is the growth rate of the cell α, $\Delta t = t - t_{new}$ is the age of the cell that divided at t_{new} and $\rho_\alpha(\Delta t)$ is a piecewise linear function

representing the apical–basal position of the nucleus as a function of Δt and cell cycle phase[21]. This function equals to zero in the S phase of the cell cycle in which the nucleus stays basal, and its value is 1 during mitosis when the nucleus is apical. The exact form of $\rho_\alpha(\Delta t)$ is defined elsewhere[21]. The growth rate g_α is drawn from a normal distribution with mean equal to $1/t_T$, where t_T is the total cell cycle time, and standard deviation $\sigma_g = 0.45/t_T$. Negative growth rates are not allowed. In the simulation, the proliferation is defined as $\lambda = \ln(2)/t_T$. The cell divides when the cell is in the M phase, that is, $\frac{\Delta t}{t_T} > 0.9$, and the cell volume exceeds a critical value, namely, $A_\alpha^0(t) > A_C$. The cell divides by introducing a new edge that splits this cell into two daughter cells that enter the next cell cycle[21].

To study how the cell area kinetics affects T1 transitions, we use different forms of $A_\alpha^0(t)$ and different levels of line-tension noise σ. In Fig. 4, different conditions for area kinetics are defined as follows:

'N/A', no division, $\sigma = 0.02$

'IKNM', $A_\alpha^0(t)$ as in equation (3), $\sigma = 0$;

'Linear', cell divisions without IKNM (that is, $\rho_\alpha(\Delta t) = 1$ in equation (3)), $\sigma = 0.02$;

'IKNM', default condition with $A_\alpha^0(t)$ as in equation (3) and Λ noise as in equation (2) with $\tau = 37$ s, $\sigma = 0.02$;

'Linear + A0 noise', apical–basal position of nucleus in equation (3) is replaced with $\rho_\alpha(\Delta t) = z$, where z is drawn from a uniform distribution ranging from 0 to 2; $\sigma = 0.02$;

'exp λ', 'exp 2λ', 'exp 4λ', a linear increase in cell area is replaced with an exponential increase, that is, $A_\alpha^0(t) = \frac{1}{2}(\exp(g_\alpha \Delta t) + 1)$; λ, 2λ and 4λ correspond to $g_\alpha = 1, 2$ and 4, respectively; $\sigma = 0.02$.

Comparison between model and data. To estimate σ from the experimental data, simulations were adjusted to generate 48 frames every 25 s, so that the timescale is comparable with the live-imaging experiment and similar to the correlation time $\tau = 37$ s. Simulations were initialized for 16 h with initialization parameters followed by 8 h with target parameters and defined magnitude of noise ($\sigma = 0$, 0.01 and 0.02). After that, the edges were tracked and filtered to avoid segmentation errors or fluctuations due to divisions and T1 transitions influencing the outcome. In particular, the edges were selected only if the two cells connected by an edge did not divide or undergo a T1 transition for the tracking interval of 48 frames. Furthermore, only the tracked edges that shared their two vertices with other tracked edges were analysed.

For every edge, the relative edge length is defined as $\tilde{l} = l/\bar{l}$, where l is the edge length at a particular time and $\bar{l}$ is the mean edge length throughout the time interval. The standard deviation of the relative edge lengths $\mathrm{std}(l/\bar{l})$ over time changes with the absolute edge length (Fig. 2d) in a manner that depends on the value of σ. This was used to compare the simulations with the experimental data for different σ values.

To compare the cell shapes between vertex model simulations and experimental data, we use the cumulative distance between the model and experimental data including the following non-dimensional descriptors $D \in \{p_0, \epsilon, \alpha, hex, p_{0CV}, \epsilon_{CV}, A_{CV}, P_{CV}\}$ (Supplementary Table 3). For each descriptor D, we calculate a difference $D_\Delta = \left|\overline{D_{exp}} - \overline{D_{sim}}\right| / \widehat{\sigma_D}$, where $\overline{D_{exp}}$ is the mean value of D obtained for all the cells in the simulation for a given set of parameters $(\bar{\Lambda}, \bar{\Gamma}, k_p, k_a)$ at final time, $\overline{D_{sim}}$ is the mean value of D estimated for the segmented data at a specific developmental stage and $\widehat{\sigma_D}$ is the standard deviation of $\left|\overline{D_{exp}} - \overline{D_{sim}}\right|$ over all the samples. The cumulative distance Δ_{tot}/n is then defined as the sum of differences D_Δ for all the descriptors, normalized to the number of descriptors, that is, $\frac{\Delta_{tot}}{n} = \frac{1}{\text{number of descriptors}} \sum_D D_\Delta$.

The z score for a given cell shape descriptor is defined as $z = \left(\overline{D_{sim}} - \overline{D_{exp}}\right) / \sigma_{\overline{D_{exp}}}$, where $\sigma_{\overline{D_{exp}}}$ is the standard deviation of the mean $\overline{D_{exp}}$ estimated for different experimental images (Supplementary Table 1). In Extended Data Fig. 2, we report the absolute value of z score.

Software and code

The vertex model code used in this study is available via GitHub at https://github.com/mpzagorski/vertex_model_python_3. The code is modified from another work[21] to include an adaptation to Python 3.7, implementation of junctional noise, handling oscillatory T1 transitions and cell lineage tracing (Methods). Custom code in Mathematica 12.1 (Wolfram) was used to analyse the results of the vertex model, estimate fragmentation coefficient, cell shape descriptors, and comparison between simulation and experimental data. Supplementary Videos 2–4 are generated using custom Mathematica 12.1 code by post-processing the results of the vertex model simulation.

Reporting summary

Further information on research design is available in the Nature Portfolio Reporting Summary linked to this article.

Data availability

Source data are available for this paper. All other data that support the plots within this paper and other findings of this study are available from the corresponding authors upon reasonable request.

Code availability

The vertex model code used in this study is available via GitHub at https://github.com/mpzagorski/vertex_model_python_3. Other code supporting the analysis in this paper is available from the corresponding authors on reasonable request.

References

50. Livet, J. et al. Transgenic strategies for combinatorial expression of fluorescent proteins in the nervous system. *Nature* **450**, 56–62 (2007).
51. Arnold, K. et al. Sox2+ adult stem/progenitor cells are important for tissue regeneration and survival of mice. *Cell Stem Cell* **9**, 317–329 (2011).
52. Muzumdar, M. D., Tasic, B., Miyamichi, K., Li, L. & Luo, L. A global double-fluorescent Cre reporter mouse. *Genesis* **45**, 593–605 (2007).
53. Katsunuma, S. et al. Synergistic action of nectins and cadherins generates the mosaic cellular pattern of the olfactory epithelium. *J. Cell Biol.* **212**, 561–575 (2016).
54. Madisen, L. et al. A robust and high-throughput Cre reporting and characterization system for the whole mouse brain. *Nat. Neurosci.* **13**, 133–140 (2010).
55. Schindelin, J. et al. Fiji: an open-source platform for biological-image analysis. *Nat. Methods* **9**, 676–682 (2012).
56. Balaskas, N. et al. Gene regulatory logic for reading the Sonic Hedgehog signaling gradient in the vertebrate neural tube. *Cell* **148**, 273–284 (2012).
57. Udan, R. S., Piazza, V. G., Hsu, C., Hadjantonakis, A. & Dickinson, M. E. Quantitative imaging of cell dynamics in mouse embryos using light-sheet microscopy. *Development* **141**, 4406–4414 (2014).
58. Aigouy, B. et al. Cell flow reorients the axis of planar polarity in the wing epithelium of *Drosophila*. *Cell* **142**, 773–786 (2010).
59. Kursawe, J., Baker, R. E. & Fletcher, A. G. Impact of implementation choices on quantitative predictions of cell-based computational models. *J. Comput. Phys.* **345**, 752–767 (2017).

Acknowledgements

We thank S. Hippenmeyer for the reagents and C. P. Heisenberg, J. Briscoe and K. Page for comments on the manuscript. This work was supported by IST Austria; the European Research Council under Horizon 2020 research and innovation programme grant no. 680037

and Horizon Europe grant 101044579 (A.K.); Austrian Science Fund (FWF): F78 (Stem Cell Modulation) (A.K.); ISTFELLOW postdoctoral program (A.S.); Narodowe Centrum Nauki, Poland SONATA, 2017/26/D/NZ2/00454 (M.Z.); and the Polish National Agency for Academic Exchange (M.Z.).

Author contributions

L.B.-M. performed the experiments and quantified and analysed the data. A.S. performed and analysed the laser ablation experiments. M.Z. performed the computational analysis. L.B.-M., A.S., E.H., M.Z. and A.K. designed the experiments. A.K., E.H. and M.Z. analysed and interpreted the results. A.K. conceived the project and wrote the paper.

Competing interests

The authors declare no competing interests.

Additional information

Extended data is available for this paper at https://doi.org/10.1038/s41567-023-01977-w.

Supplementary Information The online version contains supplementary material available at https://doi.org/10.1038/s41567-023-01977-w.

Correspondence and requests for materials should be addressed to Marcin Zagorski or Anna Kicheva.

Peer review information *Nature Physics* thanks Asako Shindo, Reza Farhadifar and the other, anonymous, reviewer(s) for their contribution to the peer review of this work.

https://doi.org/10.1038/s41567-023-01977-w

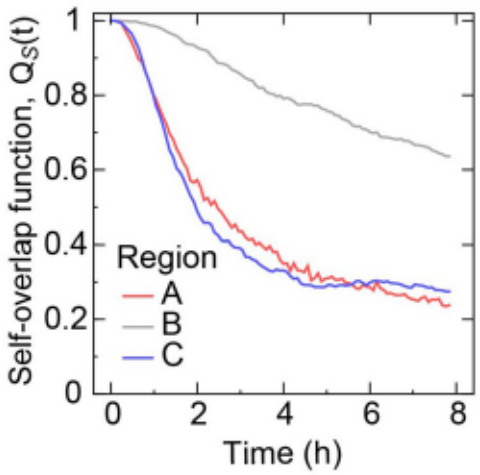

Extended Data Fig. 1 | Self-overlap function for regions A, B, C. $Q_s(t)$ quantifies the fraction of cells that remain within a characteristic distance (approximately one cell radius) after time t, after the displacement due to growth has been accounted for (Methods). Thus, fewer cells have changed their relative position in the tissue in region B compared to regions A and C. Single simulation for each region at $\bar{\Gamma} = 0.12$ and varied line tension $\bar{\Lambda} = -0.711$ (Region A, n = 702 cells), $\bar{\Lambda} = -0.393$ (Region B, n = 2546 cells), and $\bar{\Lambda} = -0.074$ (Region C, n = 1805 cells). Only cells that have not divided within 8 h are considered.

https://doi.org/10.1038/s41567-023-01977-w

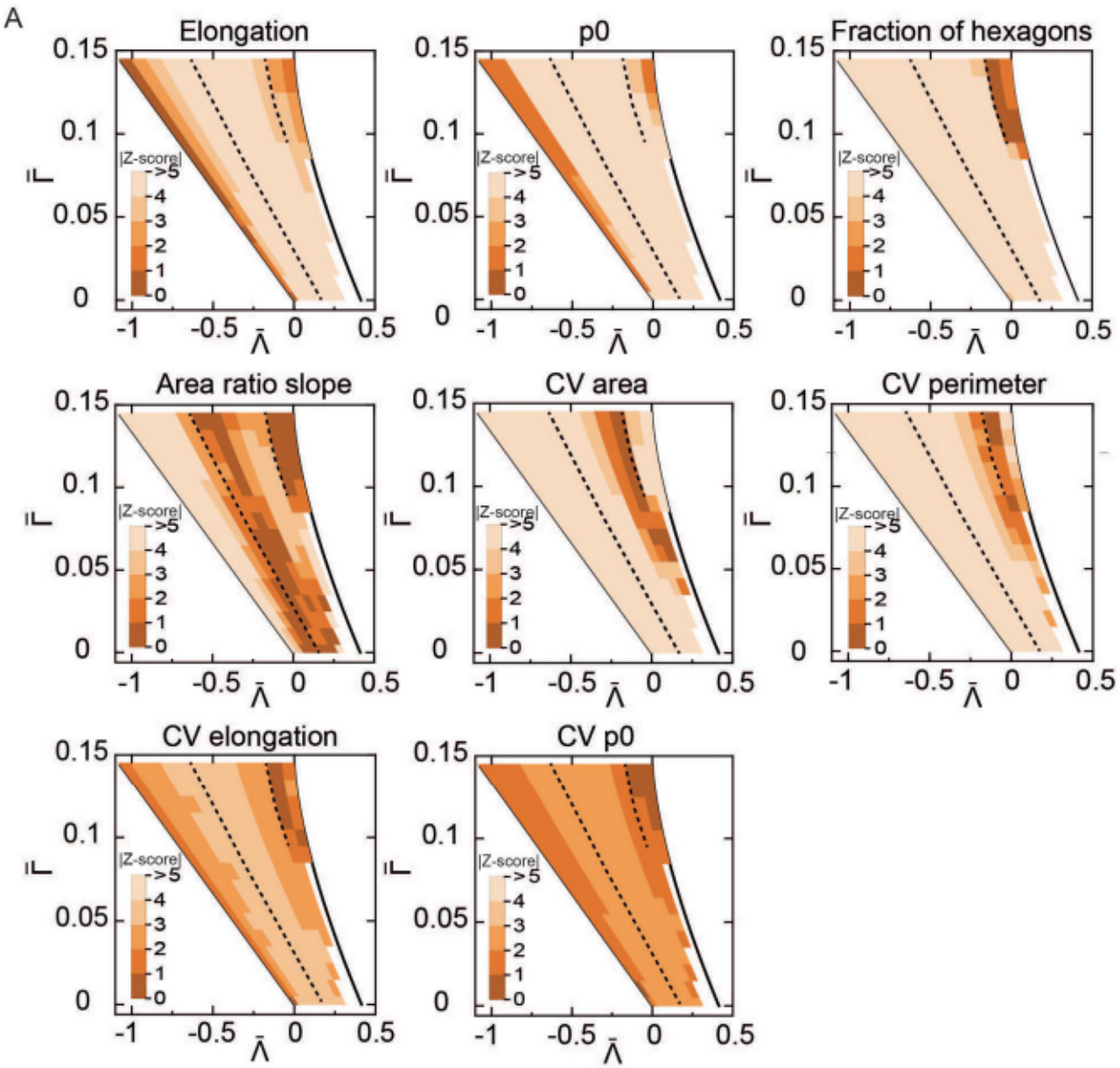

Extended Data Fig. 2 | Comparison of cell shape descriptors between experimental data at E8.5 and simulations. Difference (absolute Z-score values) between experimental data at E8.5 and simulations in units of standard deviations of the experimental data separately for each cell shape descriptor (defined in Table S3) across the $(\bar{\Lambda},\bar{\Gamma})$ parameter space (see Methods). Low values indicate good agreement between simulation and experimental estimates. The dashed lines correspond to $\phi = 0.3$ and delineate regions A, B and C (see Fig. 3A).

https://doi.org/10.1038/s41567-023-01977-w

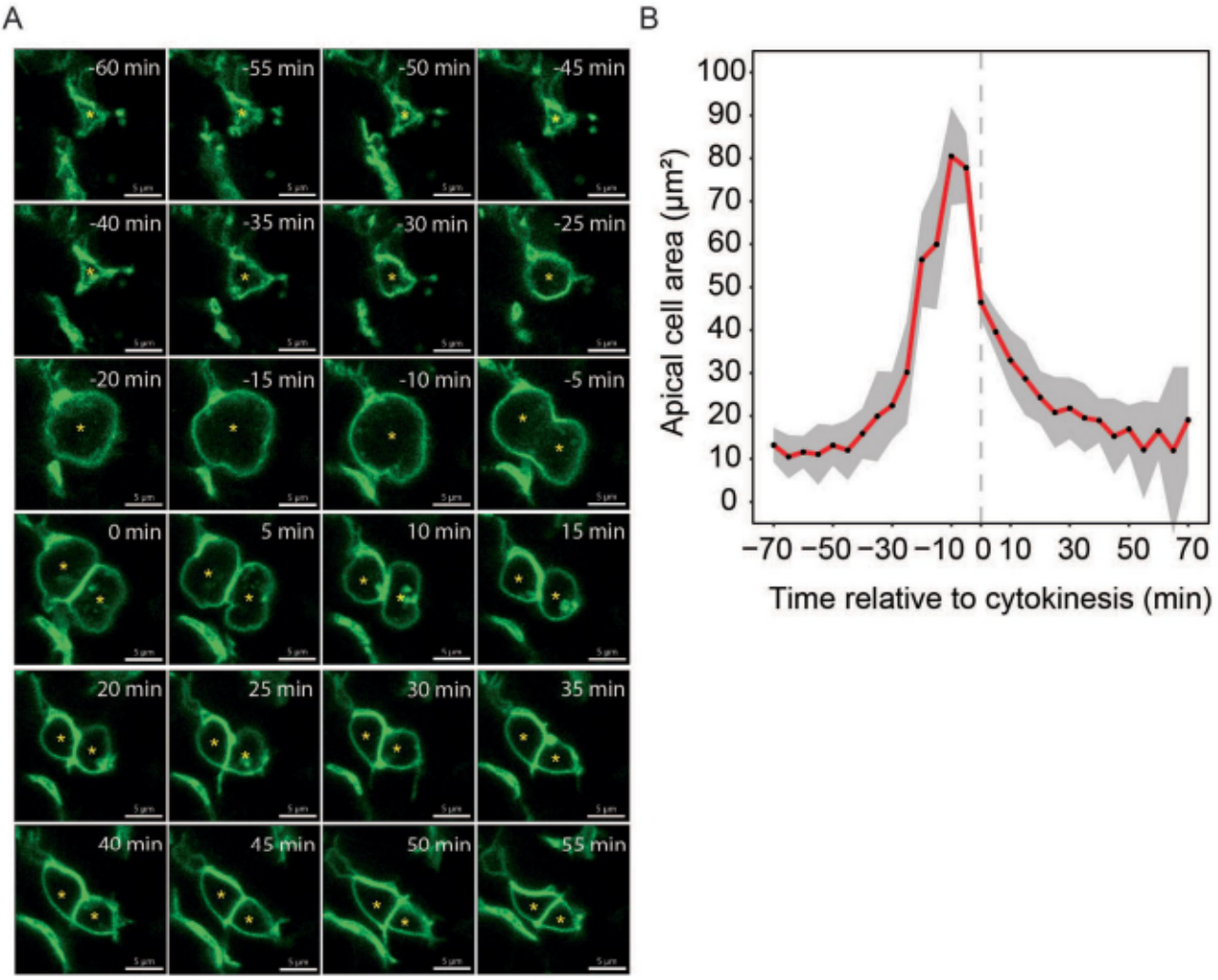

Extended Data Fig. 3 | Cell area of neural progenitors at cell division. **A.** Snapshots from confocal time lapse imaging (Supplementary Video 5) of neuroepithelial cells expressing membrane GFP at E10.5. The first subapical z-section (shown) was used for tracing and quantification. Asterisk marks a dividing cell and its daughters. Scale bars, 5 µm. **B.** Mean cell area over time quantified from time-lapse movies such as the one shown in A. n = 17 cells from 3 embryos, shaded regions 95% confidence intervals. Time = 0 is the first time point where two distinct daughter cells were detected. Dividing cells rapidly increase their apical area prior to mitosis.

Table of Contents

Supplementary figures

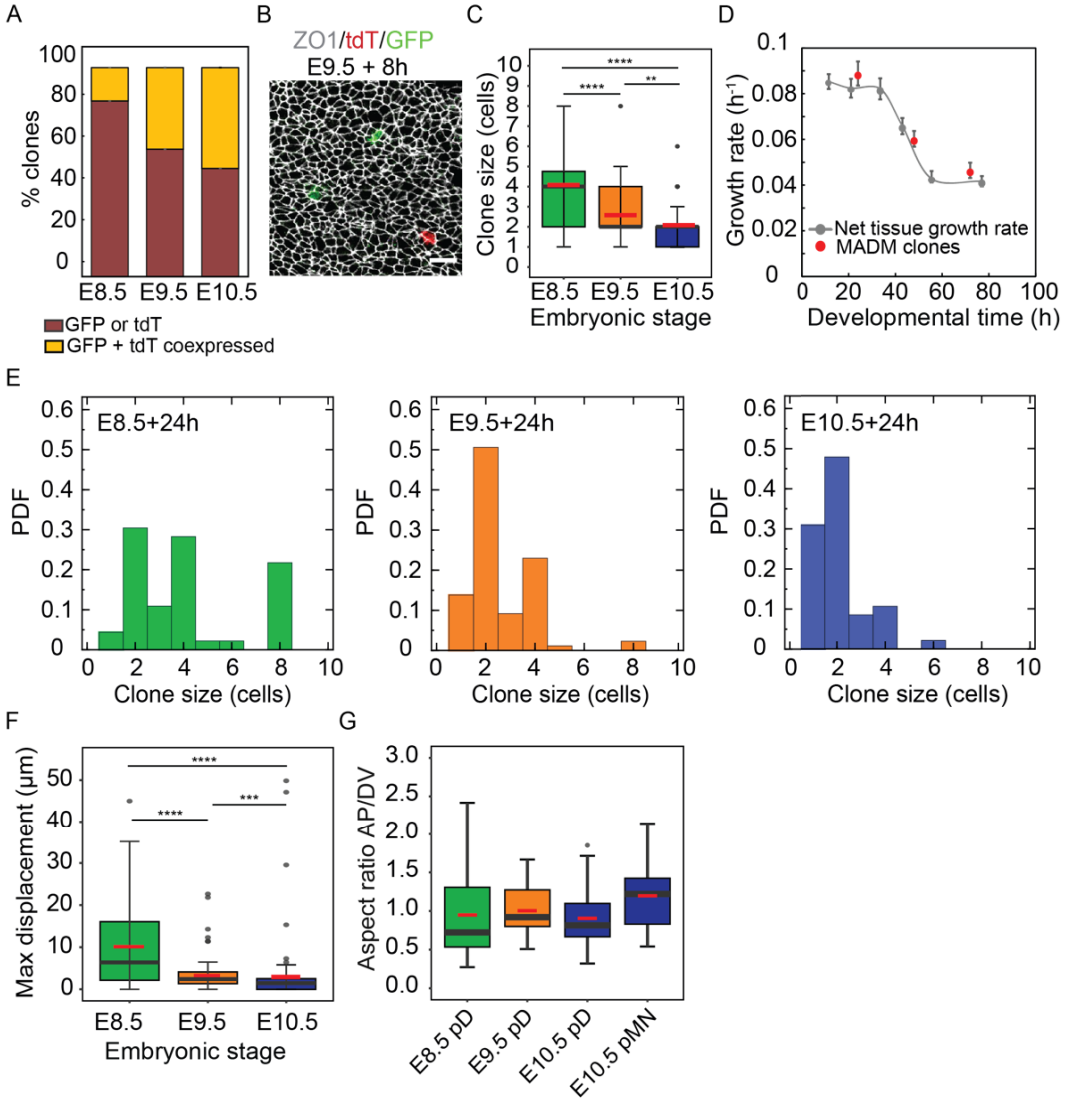

Figure S1. MADM clonal labelling in the mouse spinal cord. A. Fraction of MADM clones resulting from G2-X segregation (brown, daughter cells express either GFP or tdTomato), or G2-Z or G1 recombination (yellow, daughter cells co-express GFP and tdTomato). **B.** Confetti clones after 8h of tamofixen induction at E9.5. Immunostaining against RFP, EGFP and ZO1. Scale bar, 10 µm. **C.** Mean sizes of MADM clones induced at the indicated stages and analyzed 24h later. 25-75th percentile (box), median (black), mean (red), highest/lowest observations without outliers (whiskers). Mann-Whitney test (two-sided): *P* values = 0.0001 (E8.5 vs E9.5), 9.4e-09 (E8.5 vs E10.5), 0.0024 (E9.5 vs E10.5). Sample sizes in C-F (number of clones): E8.5 n = 46, E9.5 n = 87, E10.5 n = 94 (see also Table S1). **D.** Growth rate measured from the net growth rate of the tissue in (Kicheva, Bollenbach, Ribeiro, Valle, et al., 2014) (grey) and predicted from the mean MADM clone size (red, Methods). Error bars, mean ± SEM. **E.** Clone size distributions at different stages. **F.** Maximum displacement of labelled cells from the clone centroid for clones induced at E8.5, E9.5 and E10.5 (values correspond to 3.1±0.4, 1.1±0.1 and 1.2±0.3 cell diameters, respectively). Mann-Whitney test (two-sided) *P* = 3.3e-05 (E8.5 vs E9.5), 8.4e-09 (E8.5 vs E10.5), 0.0006 (E9.5 vs E10.5). Box-and-whisker plots as in C. **G.** AP/DV aspect ratio of clones at different stages and domains. Clones in the p3 domain and floor plate were excluded from analysis. Mann-Whitney test (two-sided) *P* > 0.05 for all pairwise comparisons. Sample sizes: n= 31, 57, 56, 6 clones (left to right; Table S1). Box plots as in C.

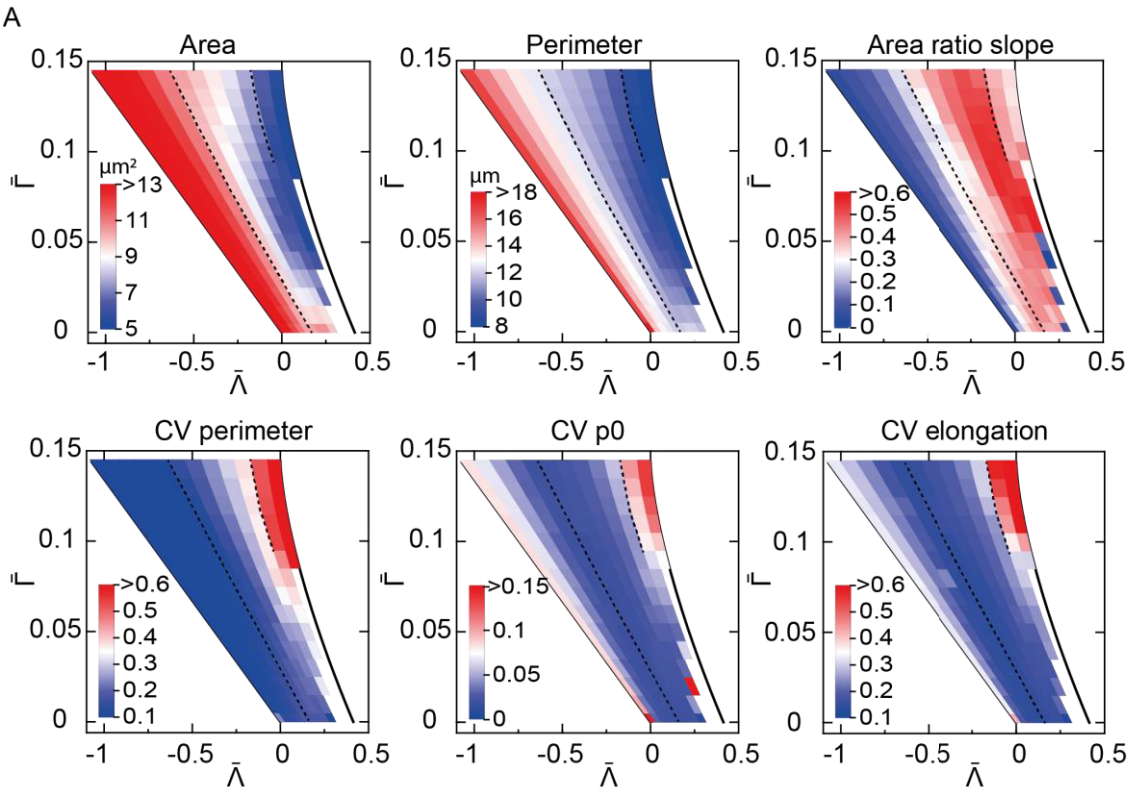

Figure S2. Cell shape descriptors in simulations. A. Mean value of the indicated cell shape descriptors (defined in Table S3) for simulations performed at different values of $\overline{\Lambda}$ and $\overline{\Gamma}$ for proliferation rate k_p = 0.09h^{-1} and differentiation rate k_n = 0. The mean value was color-coded with scale indicated in insets of respective panels. The mean was estimated from all cells pooled together from 10 simulations for each pair of ($\overline{\Lambda}$, $\overline{\Gamma}$) at the final time.

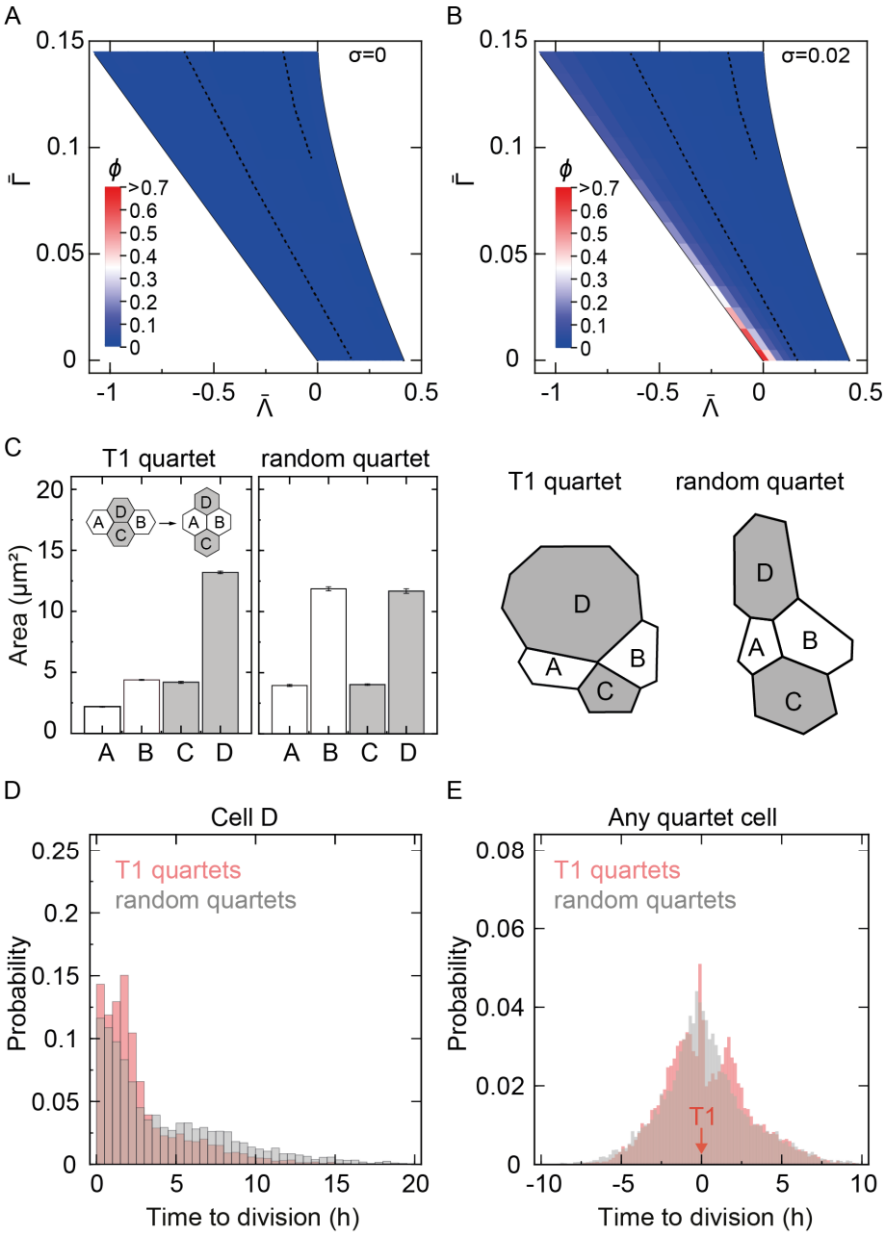

Figure S3. Relationships between T1 transitions and cell divisions in simulations. A-B. Simulations without IKNM effect (linear area increase, k_p = 0.09h^{-1}) result in non-fragmented clones. Coefficient of fragmentation for model without line tension noise (σ = 0) (A) and with σ = 0.02 (B). Dashed lines indicate the boundaries of regions A, B and C as in Fig. 3A. **C.** Mean apical cell area of cells in T1 or randomly selected quartets in simulations of region *C*. Cells in the quartets are designated A, B, C, D as indicated in the schematic and are further ordered by size (apical area), so that A<B, C<D. On the right are examples of T1 and random quartets. Error bars, SEM from 10 independent simulations with >6000 quartets each. For all pairwise comparisons between T1 and random quartets, two-sided *t*-test $P < 0.05$. **D.** Distribution of time intervals from the T1 event (or a random time point in random quartets) to cell division of the largest cell, cell D. **E.** Distribution of time intervals between T1 event (or random time point) and cell division of any cell in the quartet. Simulation parameters $\bar{\Gamma}$ = 0.12 and $\bar{\Lambda}$ = -0.074 (Region C). The T1 events (n=7387) and random quartets (n=5986) were considered in a 16h time window with 8h buffer intervals to avoid boundary effects.

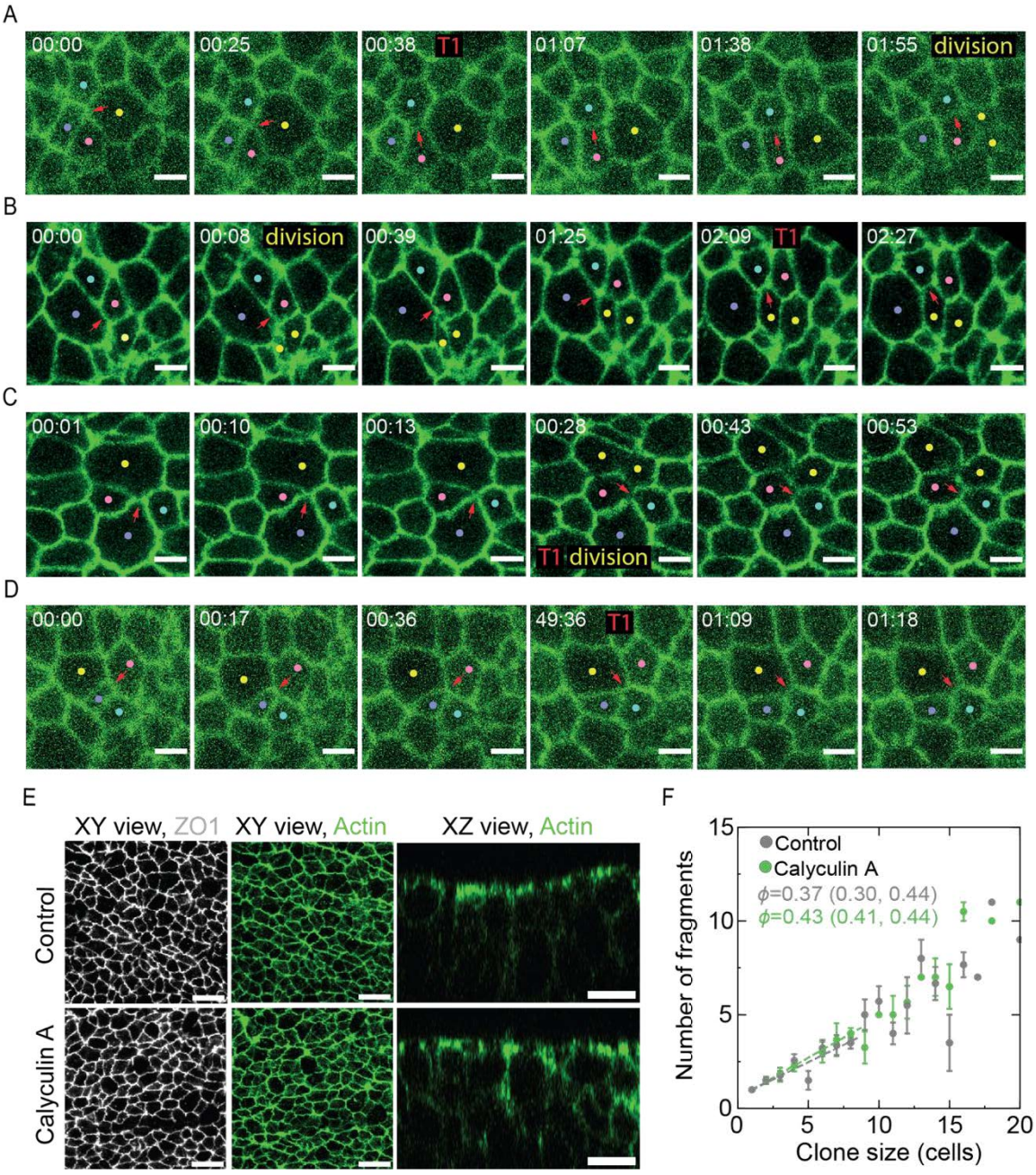

Figure S4. Relationship between cell divisions and cell rearrangements in the neural tube. A-D. Examples of time-lapse imaging of ZO1-GFP (green) expressing neural plates at E8.5. Time is shown as hh:mm. The time points of T1 transitions and cell divisions (cytokinesis) are indicated. Cell participating in the T1 transition are marked with dots, the T1 junction that changes orientation is indicated with a red arrow. The dividing cell is marked in yellow. In D, the yellow cell increases in area but does not divide in the time interval of the video. Scale bars, 5 µm. **E.** Apical view of neural epithelium treated with 0.6nM of Calyculin A or vehicle from E8.5 for 42 hours. After culture the tissue was stained for F-Actin and ZO1. Increase in the level of actin was observed along the basolateral sides of Calyculin A treated cells. Scale bars, 10 µm. **F.** The fragmentation of Confetti clones upon Calyculin A treatment is similar to control. The fragmentation coefficient ϕ (95% CI) was obtained using linear fit to the data for clones ≤8 cells (dashed lines). Sample sizes: Control n= 87, Cal A n = 69 clones. Error bars, SEM.

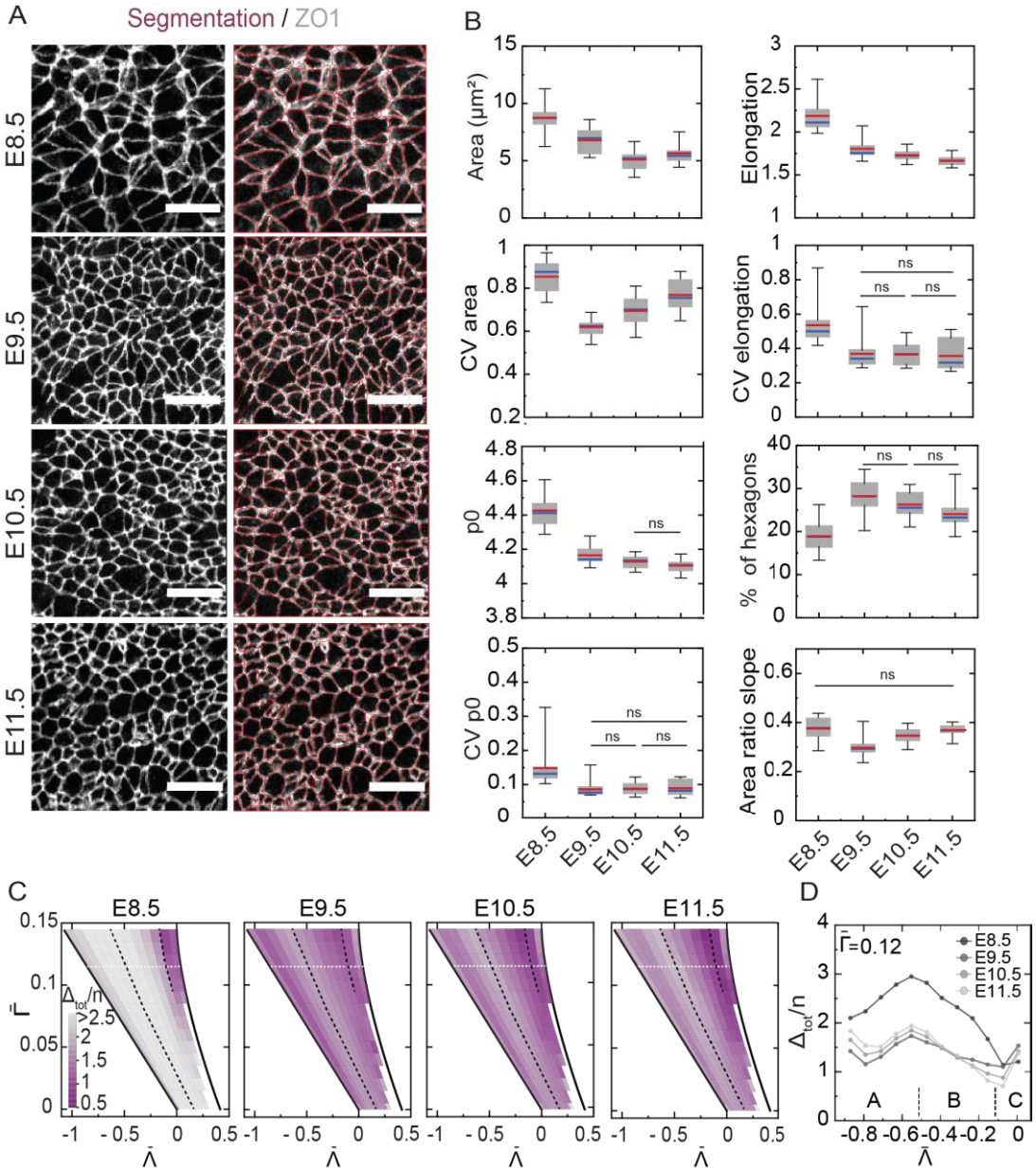

Figure S5. Cell shapes at different stages of neural tube development. A. Top, apical view of the epithelium with ZO1 immunostaining (white). Bottom, cell segmentation (red traces). Scale bars, 10 µm. **B**. Quantification of the indicated cell shape descriptors at different stages. 25-75th percentile (box), median (blue), mean (red), upper/lower fence are max/min. For all pairwise comparisons, two-sided *t*-tests were $P < 0.05$, except for the cases that are shown as ns ($P > 0.05$). Samples sizes (number of cells): E8.5 n= 6929, E9.5 n= 2433, E10.5 n= 5520, E11.5 n= 3583 (see also Table S1). **C-D.** Difference between the cumulative distribution of cell shape descriptors p_0, ϵ, α, hex, $p_{0_{CV}}$, ε_{CV}, A_{CV}, and P_{CV} (defined in Table S3) in simulations and experimental data (color-coded). In D, the values are shown numerically for $\bar{\Gamma} = 0.12$ (white dashed line in C). Black dashed lines – borders between regions A, B, C as defined in Fig. 3A.

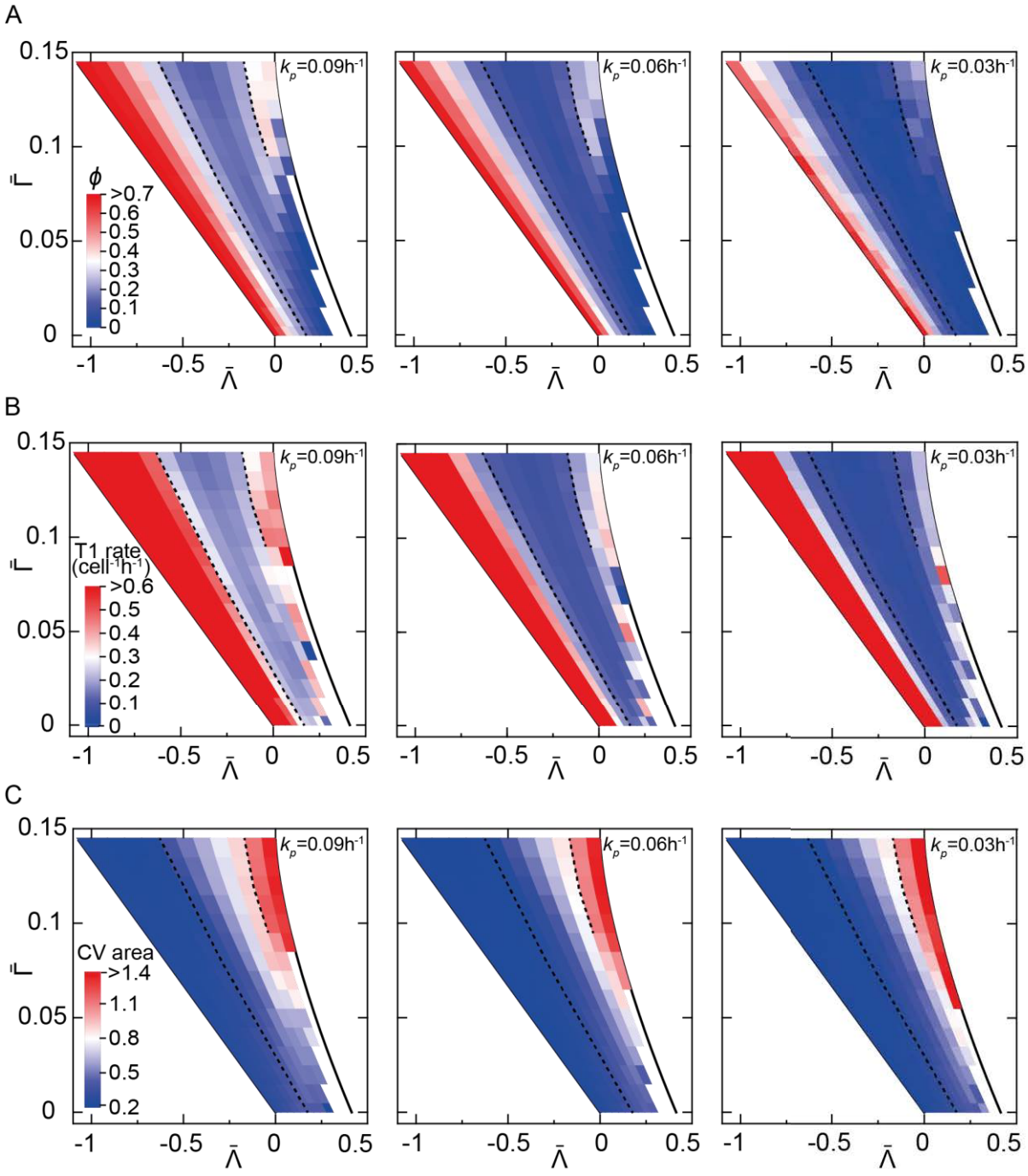

Figure S6. Fragmentation coefficient, T1 rate and cell area CV for different proliferation rates. A. Fragmentation coefficient at different values of $\bar{\Lambda}$, $\bar{\Gamma}$ for high (k_p = 0.09h^{-1}), intermediate (k_p = 0.06h^{-1}) and low (k_p = 0.03h^{-1}) rates of proliferation. Differentiation rate k_n = 0. **B.** Rate of T1 transitions with the same set of parameters as in A. **C.** The coefficient of variation of cell areas with the same set of parameters as in A. The estimates are mean values from 10 simulations for each pair of ($\bar{\Lambda}$, $\bar{\Gamma}$) at the final time.

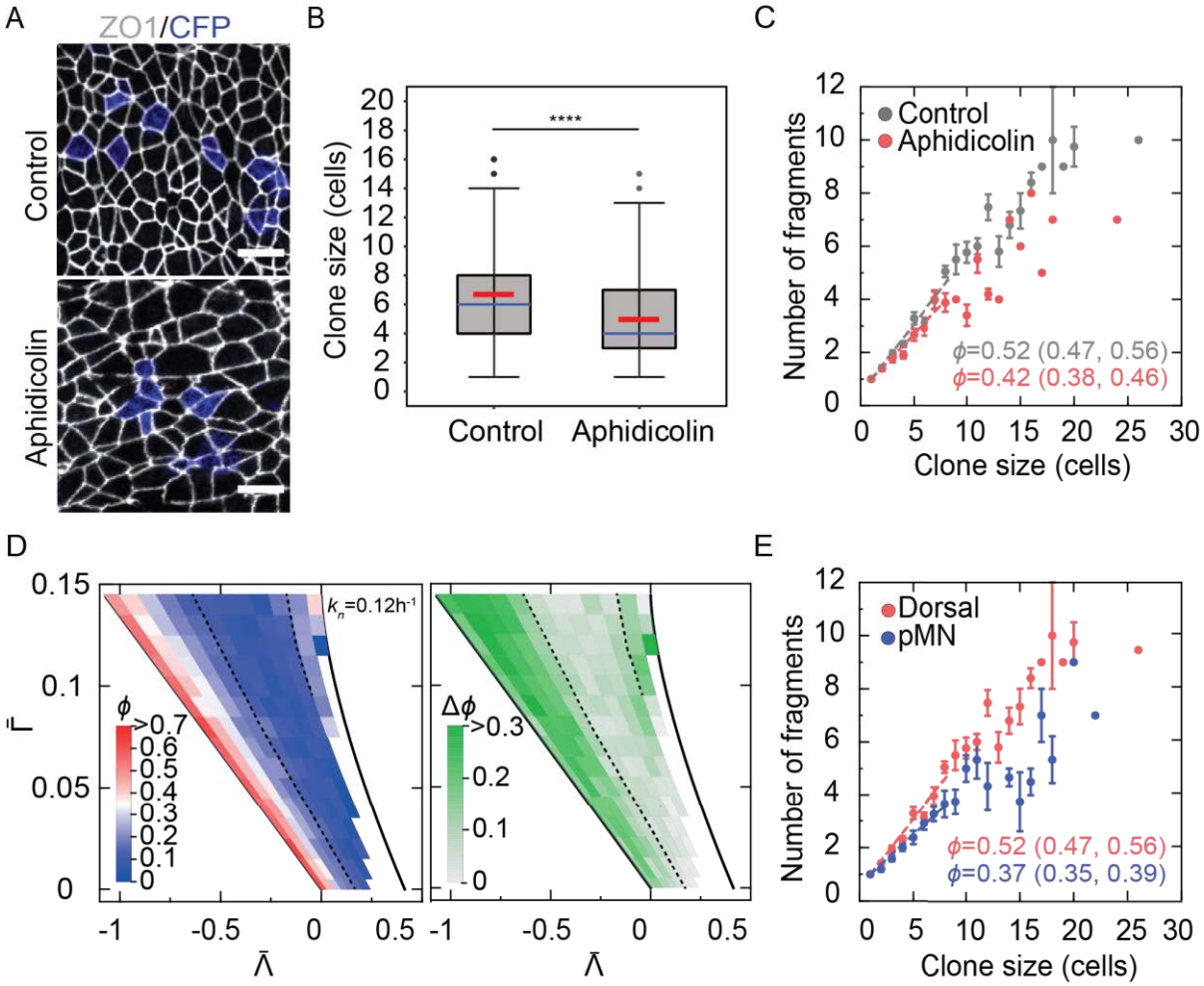

Figure S7. Cell proliferation and differentiation affect clone fragmentation. **A.** Confetti clones (CFP) from embryos injected with tamoxifen at E7.5 and cultured *ex utero* from E8.5 for 42h with 800nM aphidicolin or control medium. Scale bars, 10 µm. **B.** Clone size for the conditions in A. 25-75th percentile (box), median (blue), mean (red), highest/lowest observations without outliers (whiskers). Mann-Whitney test (two-sided), *P* = 3e-05. Samples sizes (B,C): Control n = 382 clones, Aphidicolin n = 185 clones (see also Table S1). **C.** Mean number of fragments per clone for a given clone size for control vs aphidicolin treated embryos. The fragmentation coefficient ϕ (95% CI) was obtained using linear fit to the data for clones ≤8 cells (dashed lines). Error bars, SEM. **D**. ϕ for simulations with high differentiation rate k_n = 0.12h^{-1} and k_p = 0.09h^{-1} (left). Right, difference in ϕ between k_n = 0 (Fig. 3A) and k_n = 0.12h^{-1}. **E.** Mean number of fragments per clone $\pm$ SEM for Confetti clones in the dorsal (n = 319 clones) vs pMN (n = 190 clones) domain of embryos from the control condition in Fig. 5E-G. The fragmentation coefficient ϕ (95% CI) was obtained using linear fit to the data for clones ≤8 cells (dashed lines).

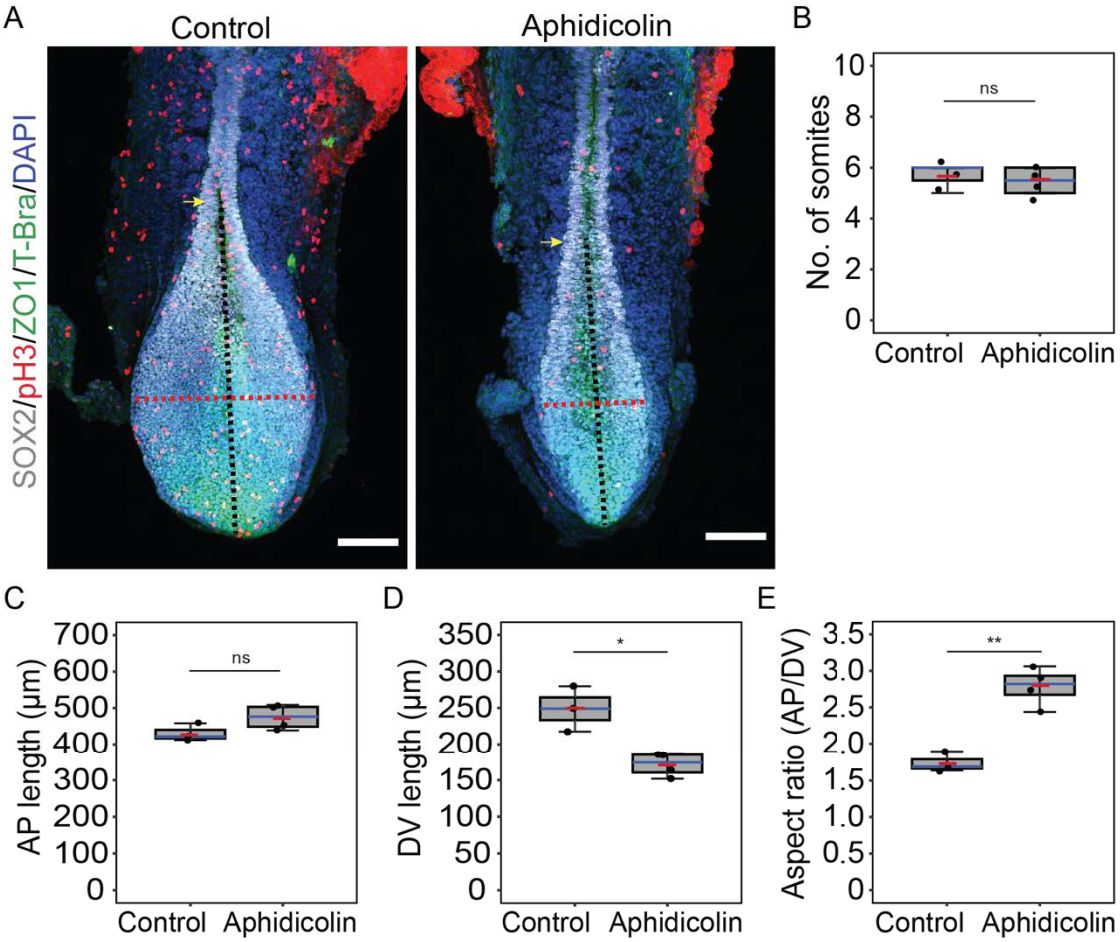

Figure S8. The proliferation rate affects tissue morphogenesis. A. Neural plate and trunk region of E8.5 embryos treated with vehicle or 5μM aphidicolin for 8 hours. Yellow arrow indicates the border of the last formed pair of somites. Scale bar, 100 μm. Anterior, up; dorsal view. **B.** Number of somites in the analysed embryos. (B-E) 25-75th percentile (box), median (blue), mean (red), highest/lowest observations without outliers (whiskers). Two-sided *t*-test ns, *P* = 0.72. **C.** Anterior-posterior length of the neural plate, measured along the black dashed line in A (from the somite border to the caudal tip). Two-sided *t*-test ns, *P* = 0.1. **D.** Dorso-ventral length of the neural plate measured along the red line in A (maximum width). Two-sided *t*-test *P* = 0.033. **E.** Aspect ratio of the neural plate (AP/DV lengths). Two-sided *t*-test *P* = 0.0014. Sample size (B-E): Control n = 3 embryos, Aphidicolin n = 4 embryos.

Supplementary tables

Table S1. Sample sizes. Number of features and number of embryos these features were quantified from.

A. Number of MADM clones used to quantify ϕ at the indicated stages (relevant to Fig. 1 and Fig. S1A-F).

Condition	Number of clones	Number of embryos	Number of litters
MADM E8.5 + 24h	46	27	10
MADM E9.5 + 24h	87	19	4
MADM E10.5 + 24h	94	32	6

B. Quantification at distinct cell cycle phases at E8.5 and E10.5 (relevant to Fig. 2A-C).

Stage	**Cell cycle phase**	**Number of cells**	**Number of embryos**
E8.5	S	172	5
E8.5	M	179	6
E10.5	S	197	6
E10.5	G2	147	5
E10.5	M	144	4

C. Edge length fluctuations in time-lapse images of ZO1-GFP embryos (relevant to Fig. 2D).

Stage	**Number of edges**	**Number of embryos**
E8.5	309	3
E10.5	387	3

D. Quantification of cell shape descriptors in Fig. 3G-H and S5.

Stage	**Number of segmented cells**	**Number of images**	**Number of embryos**
E8.5	6929	16	4
E9.5	2433	11	4
E10.5	5520	21	10
E11.5	3583	13	7

E. Laser ablation of cell bonds performed at E8.5 and E10.5 (relevant to Fig. 5A-C).

Stage	**Number of ablated junctions**	**Number of embryos**
E8.5	14	8
E10.5	11	7

F. Confetti clones analysed upon inhibition of cell proliferation (relevant to Fig. 5E-G and Fig. S7A-C).

Condition	Number of clones	Number of embryos
L-mimosine	155	7
Control	382	12

Aphidicolin	185	12
Control	382	12

G. Aspect ratio of MADM clones at different developmental stages (relevant to Fig. 1SG)

Stage	Number of clones	Number of embryos
E8.5 pD	31	18
E9.5 pD	57	17
E10.5 pD	56	30
E10.5 pMN	6	6

H. Number of Confetti clones analyzed upon Calyculin A treatment (relevant to Fig. S4E-F).

Condition	Number of clones	Number of embryos
Calyculin A	69	7
Control	87	6

I. Number of Confetti clones analyzed in the pD and pMN domain of the neural tube (relevant to Fig. S7E).

Domain	Number of clones	Number of embryos
pD	319	7
pMN	190	7

J. Neural plate dimensions upon inhibition of cell proliferation (relevant to Fig. S8).

Condition	Number of embryos
Aphidicolin	3
Control	4

Table S2. Vertex model parameters in simulations

Parameter	Description	Value
Δt	Simulation time step	0.29 s
Δl	Simulation length unit	4.6 μm
K	Elasticity	1 au
$\bar{\Lambda}$	Normalized line tension	$\bar{\Gamma}$= 0, 0.01, …, 0.14 for each $\bar{\Gamma}$ there are 10 equally spaced $\bar{\Lambda}$ that are delimited by: $-4\sqrt{2}3^{1/4}\bar{\Gamma} < \bar{\Lambda} < \frac{2\sqrt{6}}{27}(\sqrt{3} - 12\ \bar{\Gamma})^{3/2}$
$\bar{\Gamma}$	Normalized contractility	
A_c	Critical cell area	27 μm^2
l_{T1}	T1 transition length threshold	0.046 μm
l_{new}	Edge length after T1 transition	1.01l_{T1}
μ	Medium viscosity	0.12 K μm^2 s
μ''/μ'	AP to DV drag viscosity ratio	50
t_T	total cell cycle time	8 h, 12 h, 20 h
k_p	proliferation rate, $\ln 2/t_T$	0.09 h^{-1}, 0.06 h^{-1}, 0.03 h^{-1}
k_n	terminal neuronal differentiation rate	0, 0.12 h^{-1}
σ	magnitude of noise in internal line tension	0, 0.02
τ	internal line tension correlation time	37 s
σ_g	standard deviation of cell growth rate (see eq. 3)	0.45 $/t_T$

Table S3. Cell shape descriptors and their definition

Descriptor symbol	Name	Definition
A	Cell area	Apical surface area of the cells at the level of tight junctions (μm^2)
P	Cell perimeter	Perimeter of the cells at the level of tight junctions (μm)
p_0	Cell shape index	$p_0 = P/\sqrt{A}$
ε	Cell elongation	$\sqrt{v1/v2}$, where $v1$ and $v2$ are the eigenvalues of the second moment matrix of the vertices of the cell, $v1 \geq v2$
A_{CV}	Cell area CV	Coefficient of variation of *A*
P_{CV}	Cell perimeter CV	Coefficient of variation of *P*
$p_{0\ CV}$	Cell shape index CV	Coefficient of variation of p_0
ε_{CV}	Cell elongation CV	Coefficient of variation of ε
hex	Fraction of hexagons	Ratio of hexagons to all polygons in the tissue
α	Area ratio slope	Determined from a fit $\frac{\langle A_n \rangle}{\langle A \rangle} = \alpha(n-3) + b$, where $\langle A_n \rangle$ is the mean area of n-sided cells and n is the number of sides, $4 \leq n \leq 8$

Chapter 3. Supplementary results

3.1 Cellular distribution of the actomyosin network at different stages of neural tube development

The force inference we performed by comparing different cell shape descriptors between *in silico* and *in vivo* epithelia revealed that neuroepithelium topological configuration is generated in a mechanical regimen with high line tension and contractility over development. In epithelia the molecular machinery in charge of generating mechanical forces within cells is the actomyosin network, which is composed of crosslinked fibers of F-actin and the motor protein myosin II. The dynamics of the actomyosin network can induce apical cell contraction and/or generate cell-cell adhesive tension that is transmitted by adherens junctional proteins such as ZO1 (Heisenberg & Bellaïche, 2013).

In order to assess whether the actomyosin network supported the generation of high tissue tension and contractility in the neuroepithelium during development, we analysed the cellular distribution of F-actin and phosphorylated myosin II (pMLC) in transverse sections of the neuroepithelium at E8.5 and E11.5. We observed enrichment of F-actin and pMLC in the apical surface of the epithelium, marked by the expression of ZO1, at both stages (Figure 5A-B). In spite of the apical accumulation of these cytoskeleton proteins some differences are observed in their junctional arrangement, F-actin localizes over several junctions at E8.5 but not at E11.5 and pMLC signal is not only junctional but also puncta are found in the intracellular space at E8.5 but not at E11.5 (Figure 5A-B). We think these differences could be associated with the temporal changes in cell geometry that we described in the Chapter 2. F-actin and pMLC cellular localization as well as the measurement of junctional tension we present in the Chapter 2 support the conclusion that high line tension and contractility facilitates neural tube morphogenesis.

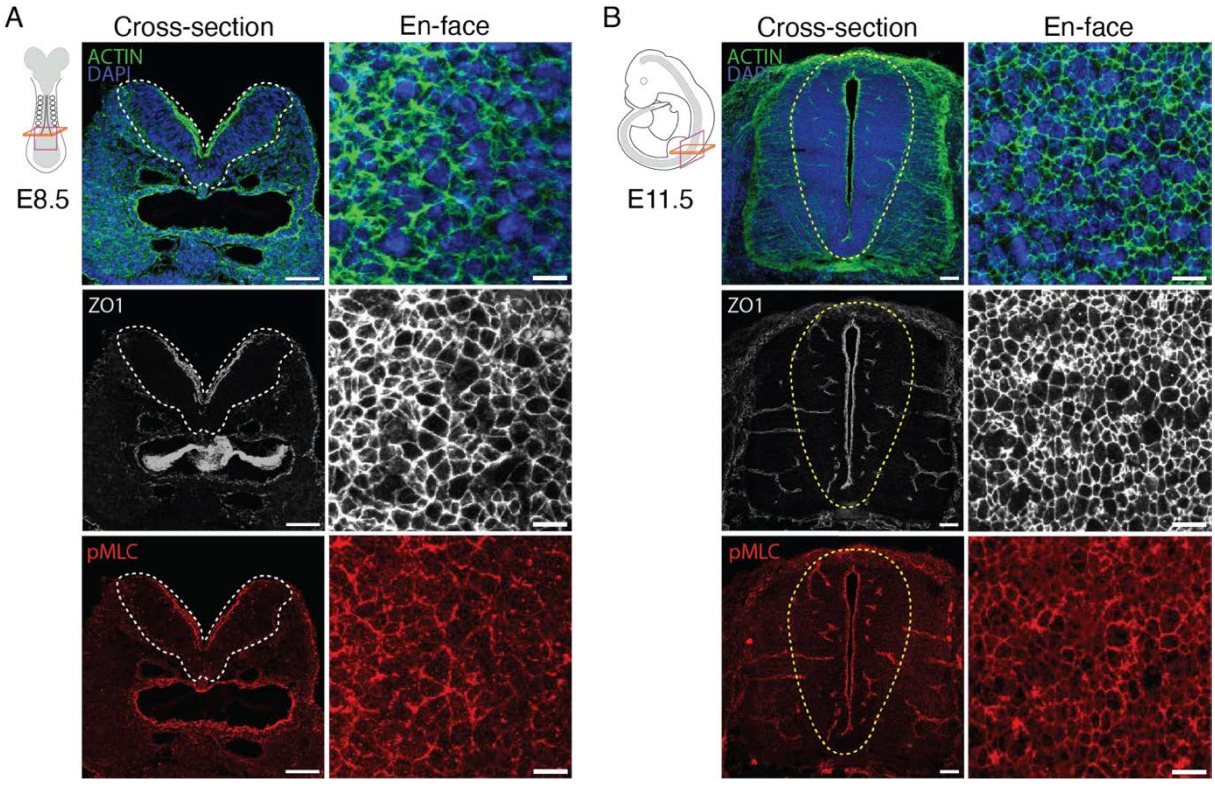

Figure 5. F-actin and pMLC localize at the apical surface of the neuroepithelium during development. **A.** Left panel, cross-sectional view of E8.5 neural plate stained for Actin, ZO1 and pMLC. Scale bar, 50 μm. Neuroepithelium is outlined by the white dashed line. Right panel, En-face view of the neuroepithelium at E8.5 stained for the same cytoskeleton proteins that in the left panel. Scale bar, 10 μm. Actin and pMLC are apically accumulated. Apical surface of the cells is marked by the expression of the ZO1, an adherens junction protein. **B**. Left panel, cross-sectional view of E11.5 neural tube stained for Actin, ZO1 and pMLC. Scale bar, 50 μm. Neural progenitors are outlined by the yellow dashed line. Right panel, En-face view of the neuroepithelium at E11.5 stained for the same cytoskeleton proteins that in the left panel. Scale bar, 10 μm. F-actin apical distribution appear to be different between stages. At E8.5 F-actin forms belts across several junctions, whereas at E10.5 the localization is restricted to singles junctions. At E8.5 pMLC not only display strong signal at the apical junctions but also puncta are observed within the cytoplasm, whereas at E11.5 puncta of pMLC are absent.

3.2 Effect of cell rearrangements on tissue patterning

Our clonal analysis revealed that the frequency of cell rearrangements is high at E8.5 and it rapidly declines 24 hours after (E9.5). This decrease of cell rearrangements coincides with the establishment of gene expression domains that have precise boundaries along the DV axis of the neural tube. The domain proportions are modulated by the net growth rate of the tissue and the gene expression boundaries are refined over time through morphogen dependent gene regulatory networks (Balaskas et al., 2012; Exelby et al., 2021; Kicheva & Briscoe, 2015). Zagorski et al., 2017 reported that upon integration of Shh and BMP opposing gradients domain boundaries could display a margin of error of less than 3 cell diameters. Taking into account these observations, we wondered whether cell rearrangement could influence progenitor domain boundaries establishment during mouse neural tube development.

In order to investigate the impact of cell rearrangement dynamics in patterning, we used the vertex model to simulate a tissue that after growing to a certain initial size, it had two marked domains separated by a straight boundary. Then, domains grew to a given final size either with high proliferation rate (0.09 h^{-1}), hence high rate of cell rearrangements, or with low proliferation rate (0.03 h^{-1}), hence low rate of cell rearrangements. We quantified the boundary imprecision by measuring the deviation of the domain boundary from a straight line ("wiggliness") or as the number of cells that become separated from the correct domain ("islands") (Figure 6A). We observed that both boundary wiggliness and the number of cell islands was higher in the tissue simulated with high rate of proliferation, thus high rate of T1 transitions, in comparison with the tissue simulated with low proliferation rate (Figure 6B-C). These results suggests that the decline in cell rearrangements at later developmental stages may help to achieve the observed boundary precision in the neural tube (Zagorski et al., 2017).

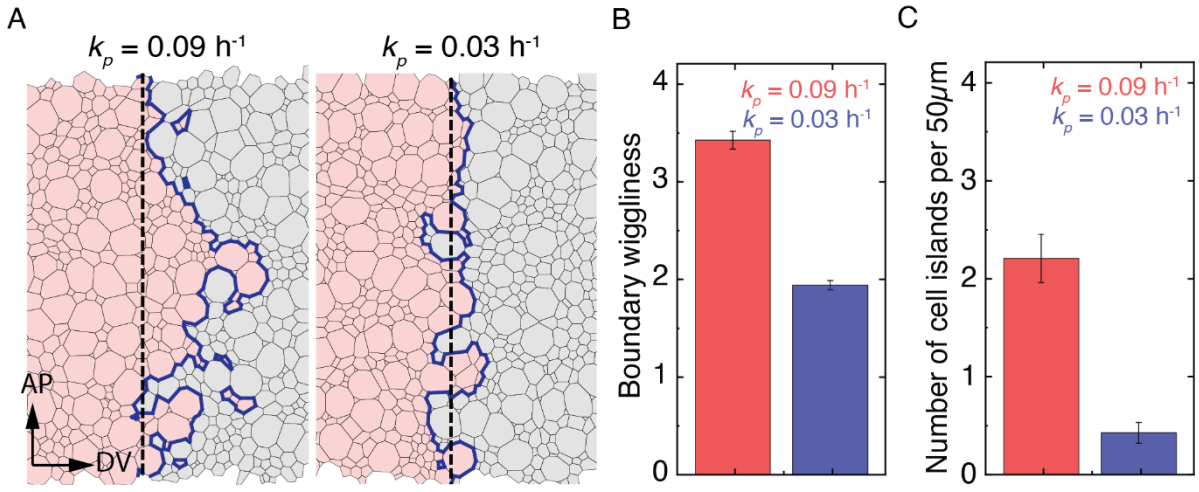

Figure 6. The rate of cell rearrangements influences boundary precision. A. Snapshots of domain boundaries in region C ($\bar{\Lambda}$ = -0.74, $\bar{\Gamma}$ = 0.12) for high and low proliferation rate (k_p = 0.09h^{-1} and 0.03h^{-1}, respectively) at the end of the simulations. Dashed line, AP_{length}. Blue line, outer boundary of the red/gray domain. **B.** Boundary wiggliness after 16h simulation, region C. **C.** Number of islands per 50 μm in region C.

3.3 Characterization of PCP signalling deficiency in the brachial neural tube

As described in the section 1.2, PCP signalling is fundamental for the proper extension and closure of the neuroepithelium during neural tube development. To understand the effects of PCP signalling in mouse neural tube morphogenesis, *Vangl2* mutants have been of particular interest, because neural tube closure in these is impaired at the first point of zippering, leaving the brachial and lumbar neural tube open during development (Greene et al., 1998). This mutant mouse is also called Lpt (Loop tail) given the kinked or curly phenotype observed in adult stages. The effect of Vangl2 mutation during neural tube development has been analysed at different embryonic stages. At E8.5, Lpt neural plate is reported broader and flatter with disrupted medial hinge point (MHP), when compared to wild type embryos. However, Shh expression domain was not affected in the Lpt mutant neural plate (Greene et al., 1998). At E9.5 and E10.5, besides the improper closure, the floor plate is enlarged and displays a broader domain of Shh expression, Pax6 expression is moderately extended dorsally, whereas Pax3 does not show any difference (Greene et al., 1998). The neural tube closure defect observed in mice with the loop tail phenotype is thought to be caused by decreased levels of neighbour exchanges within the neuroepithelium. This defect prevents the correct extension and bending of the epithelium at the midline, which in turn hinders normal neural fold elevation and apposition (Greene et al., 1998; Williams et al., 2014; Ybot-Gonzalez et al., 2007). The mesoderm adjacent to the neural tube does not display strong malformation in Lpt mice, suggesting that it is unlikely that it is involved in the neural tube defect (Greene et al., 1998).

The reported decline in cell rearrangements in the Lpt mutant provides an opportunity to experimentally investigate the potential impact of these events on tissue patterning. Although it is known that convergent extension, which involves neighbor exchange events, is responsible for the closure defect in these mutants, the quantitative contribution of cell rearrangements to this defect remains unclear. Therefore, we aimed to characterize the dynamics of the brachial neuroepithelium in Lpt homozygous mutants (*Vangl2*$^{Lp/Lp}$) by quantifying the coefficient of clone fragmentation to measure cell rearrangements, the rate of proliferation and the DV pattern at different stages during neural tube development.

We first collected embryos at E9.5 and E10.5, and observed that the neural tube was opened from approximately the cervical region of the prospective spinal cord until the last caudal zipping point at both stages, as expected (Figure 7A). The AP elongation of the body axis illustrated by the number of somites, was significantly smaller in the Lpt homozygous mutants (Lpt hom) in comparison with their wild type (wt) litter mates (Figure 7B). We did not observe any difference in somite morphology between the mutants and wild type embryos. These results illustrate that abrogation of PCP signalling substantially affects the body axis elongation, as has been described in previous studies (Mahaffey et al., 2013; McGreevy et al., 2015).

Changes in tissue dimensions in the Lpt mutant were also apparent in transverse sections through the brachial region of the neural tube (Figure 8A-B). We found a small increase in the apicobasal height of Lpt hom neuroepithelium at E10.5 but not E9.5 (Figure 8C, F). Crucially, at both stages there was a significant increase in the DV length of the Lpt neural tubes, measured along the apical surface. The DV length of Lpt hom neuroepithelium was 1.7-fold bigger at E9.5 and 2.5-fold bigger at E10.5 than the wild type (Figure 8C, F), indicating that while the AP axis in Lpt mutants is shorter, their DV axis is larger than the wild type litter mates.

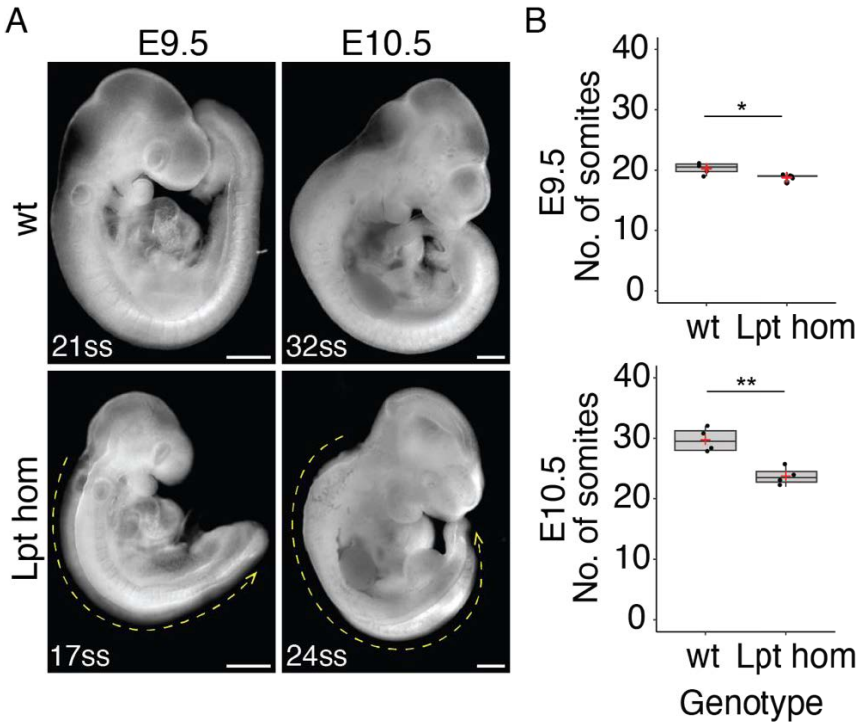

Figure 7. PCP signalling inhibition affects body axis elongation. A. Wild type and Lpt homozygous (hom) mutant embryos collected at E9.5 and E10.5. Lpt hom embryos displayed opened neural tube from the cervical region to the posterior end of the neural tube (yellow dashed arrow). Scale bar 500 µm. **B.** Comparison of the number of somites in wild type and Lpt hom embryos at E9.5 (4 embryos per genotype) and E10.5 (4 embryos per genotype). Boxplots show the 25-75% quartiles median (black), mean (red crosses). Two-sided t-tests at E9.5 *P = 0.048 and at E10.5 **P = 0.0045.

To assess the effect of the Lpt mutation on DV patterning, we collected transverse sections from the neural tube at the forelimb level and immunostained them for transcription factors that characterize the neural progenitor domains along the DV axis: pd1-pd3 domains are marked by the expression of *Olig3;* the entire dorsal domain (pD) is marked by *Pax3*; p3 to p2 ventral domains are marked by the expression of *Nkx6.1*; pMN by Olig2, p3 by *Nkx2.2*, and floor plate by *Foxa2* (Figure 8A-B). We found that the dorsal and ventral domains in the Lpt mutant embryos were specified normally, all the domains marked by the expression of different set of transcription factors as described above were present in mutant and wild type neural tubes (Figure 8A-B). Then, by measuring the area of the progenitor domains relative to the *Sox2* positive area that spans the entire length of the DV axis, we observed that the domain proportions in the Lpt mutant neural tube were very similar to wild type. We observed a slight increase in the relative sizes of dorsal domains in Lpt mutants (Figure 8D, G). Because we noticed substantial variation in the DV size of the Lpt hom neuroepithelium between embryos and even sometimes between the neural tube halves within a single embryo, it will be necessary to increase the sample size in order to validate these observations. Nonetheless, our preliminary results suggest that morphogen signalling adapts to the change in the DV axis size in the Lpt mutant neuroepithelium to generate patterning with correct proportions.

Greene et al., 1998 reported enlargement of the floor plate in the Lpt hom mutant embryos marked by the expression of *Netrin 1*, however our preliminary quantifications do not show this difference in the floor plate relative size at E9.5 or E10.5. This discrepancy could be explained by the location at which the transverse sections were analysed between our study

and their study. Greene et al., 1998 used transverse sections at mid-axial (thoracic) levels along the AP axis at E9.5, whereas we used sections at the level of the brachial neural tube. Furthermore, they do not present an estimate of the floor plate domain size relative to size of the DV axis of Lpt mutant epithelium, which we have shown in this study to be larger than that of the wild type epithelium.

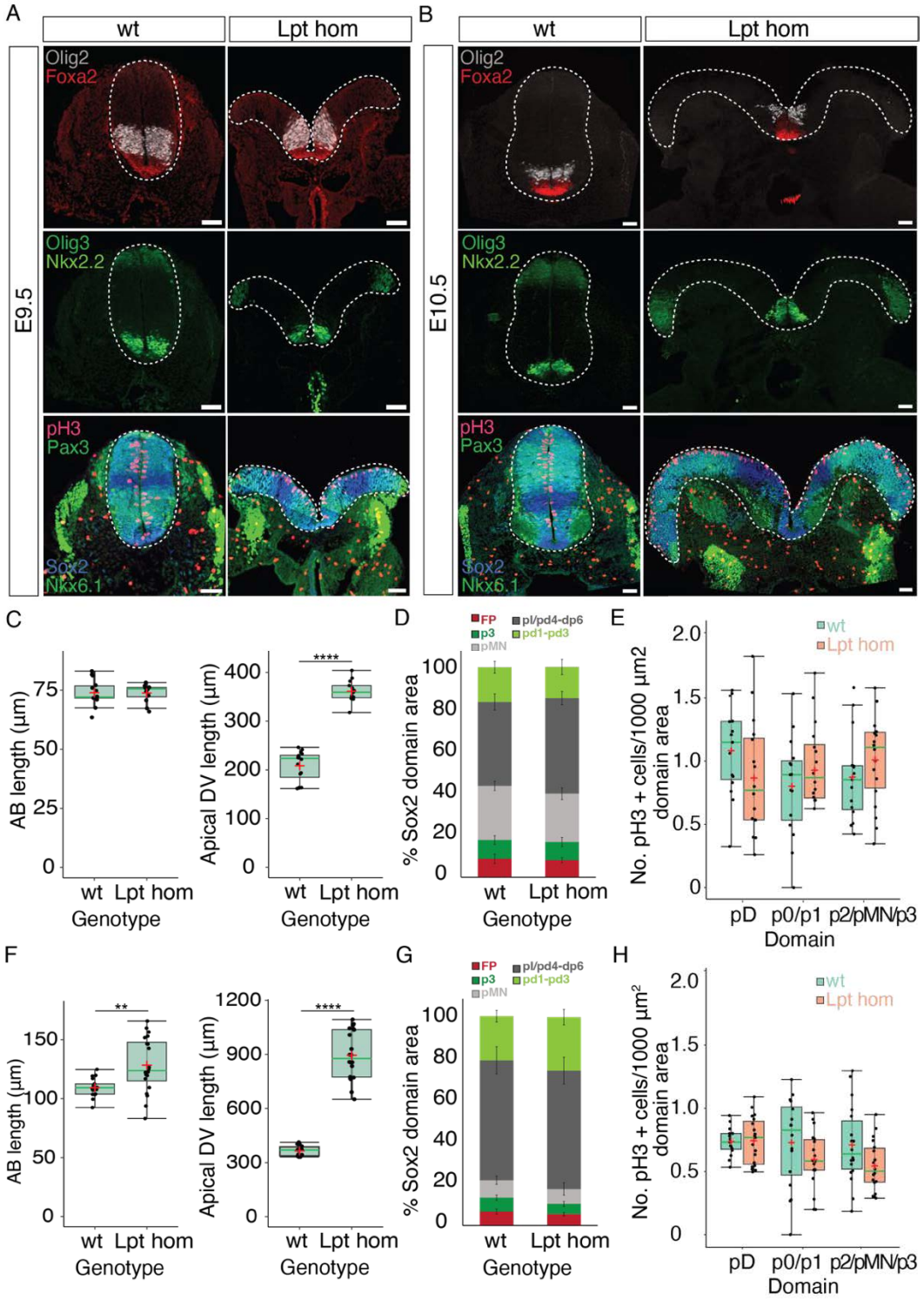

Figure 8. Dorsoventral length increase upon PCP signalling inhibition is not affected by changes in the rate of cell proliferation. A. E9.5 and **B.** E10.5 transverse sections from wt and Lpt hom neural

tubes and markers used to identify the progenitor domains along the DV axis. Sox2 was used to estimate the total area of neural progenitor cells along the DV axis and pH3 to estimate the proliferation rate. Scale bars 50 μm. **C.** Comparison of the apicobasal (AB) length and the apical dorsoventral (DV) length of the wild type and Lpt hom neuroepithelia at E9.5. AB length two-sided t-test ns, P = 0.95, apical DV length two-sided t-tests ****P = 7.2e-15. Sample size. wt: 3 embryos, 3 sections, Lpt hom: 3 embryos, 3 sections. **D.** Comparison of the mean relative DV domain area size between wild type and Lpt homozygous neuroepithelia at E9.5. Error bars, mean ± sd**.** Sample size. wt: 2 embryos, 4 sections, Lpt hom: 2 embryos, 4 sections**. E.** Comparison of the proliferation rate at distinct domains along the DV axis of wild type and Lpt homozygous neuroepithelia at E9.5. Two-sided t-tests ns, P > 0.05 for all pair-wise comparisons. Sample sizes. wt: 3 embryos, 3 sections, Lpt hom: 3 embryos, 5 sections. **F.** Comparison of the apicobasal (AB) length and the apical dorsoventral (DV) length of the wild type and Lpt hom neuroepithelia at E10.5. AB length two-sided t-test **P = 0.0023, apical DV length two-sided t-tests ****P = 1e-13. Sample size. wt: 3 embryos, 4 sections, Lpt hom: 3 embryos, 5 sections. **G.** Comparison of the mean relative DV domain area size between wild type and Lpt homozygous neuroepithelia at E10.5. Error bars, mean ± sd. Sample size. wt: 3 embryos, 3 sections, Lpt hom: 2 embryos, 3 sections. **H.** Comparison of the proliferation rate at distinct domains along the DV axis of wild type and Lpt homozygous neuroepithelia at E10.5. Two-sided t-tests ns, P > 0.05 for all pair-wise comparisons. Sample sizes. wt: 3 embryos, 3 sections, Lpt hom: 3 embryos, 5 sections. All boxplots represent 25-75% quartiles, median (green), mean (red crosses), highest/lowest observations without outliers (whiskers).

Given that we observed a substantial increase in the DV length of Lpt hom neural tube, we assessed whether this could be generated by a change in the proliferation rate. We quantified the fraction of mitotic neural progenitors by immunostaining pH3 and Sox2. We did not find significant differences in the rate of proliferation between Lpt hom mutant embryos and the wild type litter mates along the DV axis at any of the analysed stages (Figure 8E, H). Thus, the rate of cell proliferation is not responsible for the increase in DV length of the neuroepithelium in Lpt mutant embryos. This result suggests that the total number of cells in the Lpt hom epithelium and wild type epithelium may be the same, thus the difference in AP and DV length in the mutant probably arises from the redistribution of cells along the AP and DV axes.

To further investigate the tissue anisotropy in the Lpt mutant embryos, we induced Confetti clones in the neuroepithelium at E8.5 and analysed them 48 hours later (Figure 9A) (Methods). Our analysis shows that Lpt mutant clones fragment less than wild type clones indicating a decrease in cell rearrangements (decrease in the rate of T1 transition) at early stages of neural tube development, consistent with previous reports (Williams et al., 2014) (Figure 9A-B). We also quantified the AP/DV clone aspect ratio and we found no significant difference between the aspect ratio of Lpt mutant clones and wild type clones, clones were isotropic (Figure 9C). This result alone does not allow us to distinguish whether there is an effect of T1 orientation or another factor that could contribute to anisotropic growth. Moreover, unreliable clone assignment in this genetic background could be a factor that challenges the interpretation of clone shape, thus the aspect ratio. To address this, sparser labelling using MADM clones could be employed, or alternatively, stricter criteria for reliable identification of clones might be necessary. This, together with direct measurements of T1 orientation by live imaging would help to investigate the mechanism behind altered tissue shape in the Lpt mutant. Our analysis does not distinguish potential domain-specific effects on cell rearrangements, because collecting clone data from the ventral domains of Lpt mutant neuroepithelium, which are highly deformed compared to wild type, is technically challenging. Future studies would be needed to understand how cell rearrangements differ between different DV positions.

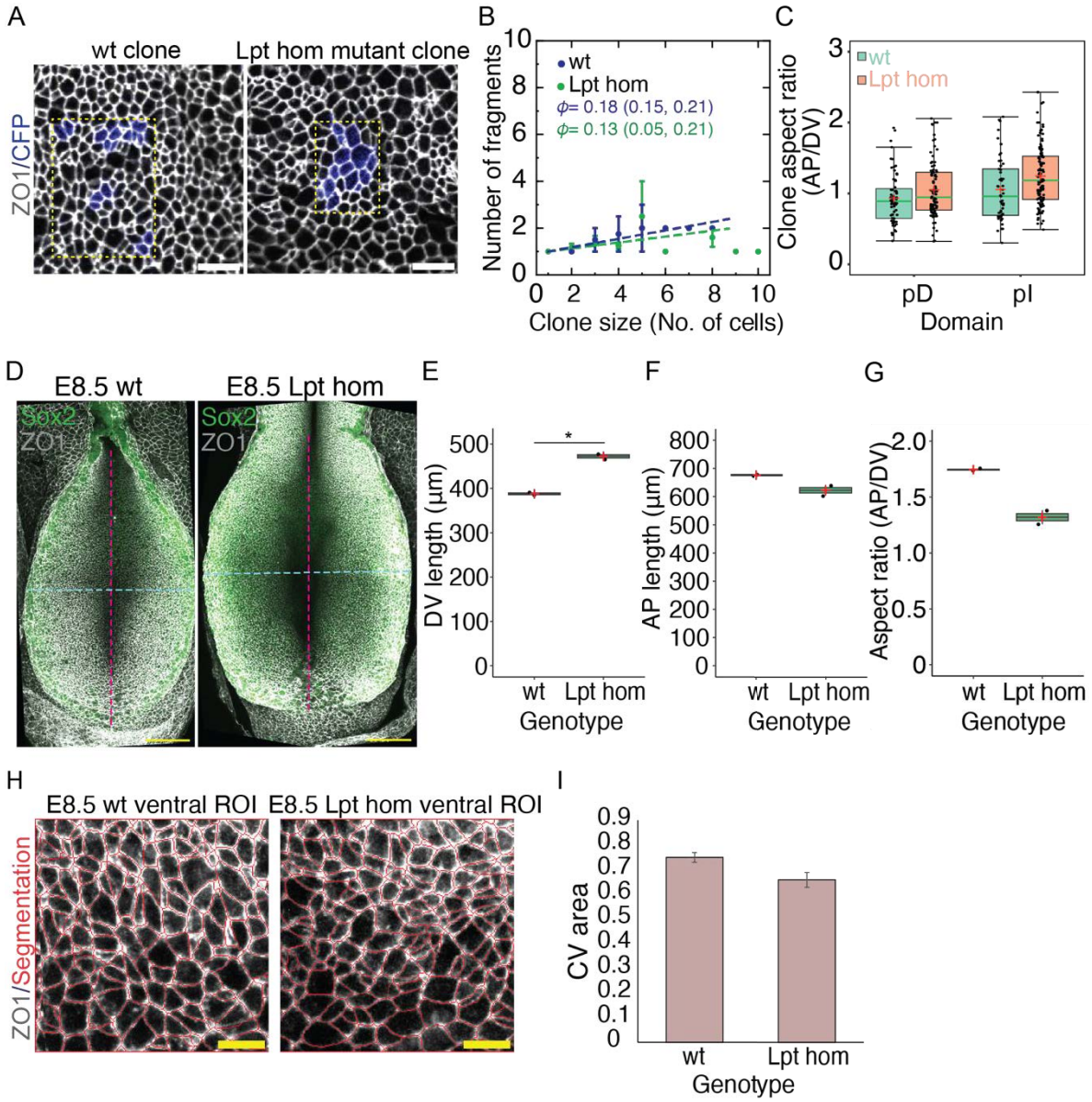

Figure 9. Lpt mutant neuroepithelium displayed low apical area variability and AP/DV aspect ratio. **A.** Confetti clones marked by the expression of mCFP produced in the wild type and Lpt homozygous neuroepithelia. DV axis is up to down of the image. Scale bars 10 µm. **B.** Mean number of fragments per clone for a given clone size produced in the wild type and Lpt homozygous neuroepithelia. Error bars, mean ± SEM. Clones were induced at E8.5 and were analysed 48 hours after. Corresponding fragmentation coefficient ϕ (95% CI) was obtained using linear fit to the data for clones ≤8 cells (dashed lines) Sample sizes. wt: 17 clones, Lpt hom: 40 clones. Only clonally labelled cells that were not in proximity with other labelled cells in a radius of 70 µm were used for the analysis. **C.** Aspect ratio of clones generated in the dorsal (pD) and intermediate (pI) progenitor domains in the wild type and Lpt homozygous neuroepithelia. The aspect ratio was estimated from the AP and DV boundary lengths of rectangles drew (yellow dashed in A) around the clones. 25-75th percentile (box), median (green), mean (red croix), highest/lowest observations without outliers (whiskers). Two-sided t-tests ns, P > 0.05 for all pair-wise comparisons. Sample sizes. pD wt: 65 clones, pD Lpt hom: 93 clones, pI wt: 54 clones, pI Lpt hom: 114 clones. **D.** wild type and Lpt homozygous neural plate at E8.5 stained for ZO1 and Sox2. Scale bars 100 µm. **E.** Dorsoventral length (cyan dashed line in D) of wild type and Lpt homozygous neural plates. Two-sided t-tests *P = 0.022. **F.** Anteroposterior (AP) length (dark pink

dashed line in D) of wild type and Lpt homozygous neural plates. Two-sided t-tests ns, P = 0.21. **G.** Aspect ratio (AP/DV) of the wildtype and Lpt homozygous neural plates Two-sided t-tests ns, P = 0.089. Sample sizes from E-G. wt: 2 embryos, Lpt hom: 2 embryos. Boxplots show the 25-75% quartiles, median (black), mean (red crosses). **H.** Example of segmented ventral ROIs (region of interest) in the wild type and Lpt mutant neuroepithelia based on ZO1 staining. Scale bars 10 μm. **I.** Cell apical area variability in the wild type and Lpt homozygous neuroepithelium. Error bars, mean ± SEM. Sample size. wt: 1138 cells, Lpt hom: 647 cells.

In our computational model, a decline in the extent of clone fragmentation without any changes in the rate of proliferation, would imply that one of the other vertex model parameters is changed. The parameters that are essential to observe clone fragmentation in the model are cell contractility, junctional tension, junctional tension noise and cell loss. A decline in the contractility and/or junctional tension would correspond to subregion B of the vertex model parameter space (see Chapter 2). Indeed, in region B the AP/DV aspect ratio of the tissue is predicted to be lower than in region C. Interestingly, we observed a decrease in the aspect ratio of the Lpt mutant neural plate in comparison to the wild type (Figure 9D-G). This raises the possibility that the decreased frequency of cell rearrangements in the Lpt mutant arises as a result of changes in the effective cell junctional tension and /or contractility, which in turns decreases the efficiency with which the tissue elongates along the AP dimension. Consistent with this idea, we observed a small decrease in the apical cell area variability (area CV) of Lpt mutant neural plates (Figure 9H-I), which may be indicative of lower contractility and junctional tension in the mutant tissue. Nevertheless, these predictions need further experimental validation. Furthermore, the observed decrease in clone fragmentation is minor, which raises the possibility that the phenotypic differences in the AP/DV aspect ratio of the tissue in the Lpt mutant arise as a result of altered T1 orientation, rather than T1 frequency.

Laser ablations in the posterior neuropore, which is the caudal region of the neural tube after the posterior zipping point (Galea et al., 2018), have resulted in diminished cell retraction thus reduced apical tension in *Vangl2* depleted neuroepithelial cells in comparison to wild type cells (Galea et al., 2021). This difference in the mechanical forces generated by the mutant cells alongside the decrease in cell rearrangements and apical cell area variability could suggest that Lpt hom epithelium has solid-like characteristics, where low fluctuations in the cell edges contribute to the defect in tissue shape and size. Further analyses are required to quantitatively describe what are the material properties of the Lpt mutant neuroepithelium during development. For example, the injection of magnetic beads and subsequent analysis of how the tissue responds to the application of mechanical forces could provide valuable insight into the physical state of the epithelium. Additionally, the quantification of cell shape index and other cell shape descriptors could help to determine the epithelium topological configuration and packing, shedding light on epithelium dynamics. Finally, studying the temporal and spatial dynamics of PCP signalling and actomyosin apical activities in the Lpt homozygous mutant neuroepithelium could be crucial for understanding how their perturbation influences tissue morphogenesis.

3.4 Characterization of *Pten* knock-out in the brachial neural tube

Pten gene has been described to modulate cell proliferation (Huang et al., 1999; Nowak et al., 2013), cell survival (Chaffee et al., 2016), cell death (Huang et al., 1999), cell migration (Bloomekatz et al., 2012) and cell morphology (Grego-Bessa et al., 2015) in different epithelia. In particular at early stages of neural tube development (E8.5), *Pten* deletion has been observed to perturb neuroepithelium morphogenesis by hindering the cell geometry over time (Grego-Bessa et al., 2015). Pten null mutant cephalic neural plates ($PTEN^{flox/flox}$, Sox2creERT2/+) are strongly ruffled and less pseudostratified in comparison to wildtype cephalic neural plates. Cells in the mutant neuroepithelium do not change from cuboidal to columnar and their apical surface do not decrease from E7.5 to E9.0. Thus, the apical area of Pten null cells is ~2-fold bigger than the apical area of wild type cells by E8.5 (Grego-Bessa et al., 2015).

Given the effect of *Pten* deletion in the cephalic neuroepithelium architecture, we wanted to use this mutant mouse to determine the role of cell geometry in cell rearrangements during spinal cord development. Thereby, we crossed $Pten^{flox/flox}$ mice with Sox2creERT2 hemizygous (Sox2creERT2/+) mice and injected pregnant females with high concentration of tamoxifen (3 mg/200 µl of tamoxifen in corn oil) at E4.5, E5.5, E6.5 and E7.5 in order to induce *Pten* knock-out. Subsequently, we analysed the effect of *Pten* deletion in the apicobasal length of E9.5 mutant neural tubes (at the brachial level) in cross-sections (Figure 10). We also qualitatively assessed the effect of *Pten* deletion in patterning and cell proliferation.

Conditional *Pten* knock-out at different stages of neural tube development did not affect cell proliferation or patterning (Figure 10A-E). The number of mitotic figures as well as the progenitor domains marked by the expression of different transcription factors appeared to be similar between the Pten mutant ($Pten^{flox/flox}$, Sox2creERT2/+) and wild type neural tubes. Furthermore, the apicobasal length of the neuroepithelium did not change after knocking-out *Pten* 120 hours (E4.5), 96 hours (E5.5), 72 hours (E6.5) or 48 hours (E7.5) before the tissue collection in comparison to the wildtype littermates (Figure 10H). The apical area of cells in the Pten mutant caudal neural plate was similar to the apical area of wild type cells (Figure 10E-G). Altogether, these results show that conditional *Pten* knock-out does not disrupt the neural epithelium architecture during neural tube development. *Pten* knock-out in our experiments relied on tamoxifen-inducible Cre mediated gene recombination that leads to the gene excision in neural progenitors expressing *Sox2*. It is possible that with this system *Pten* knock-out is not fully efficient, thus in order to further investigate the role of *Pten* during neural tube development it will be important to use a conditional system such as is Sox2-cre that does not depend on tamoxifen induction.

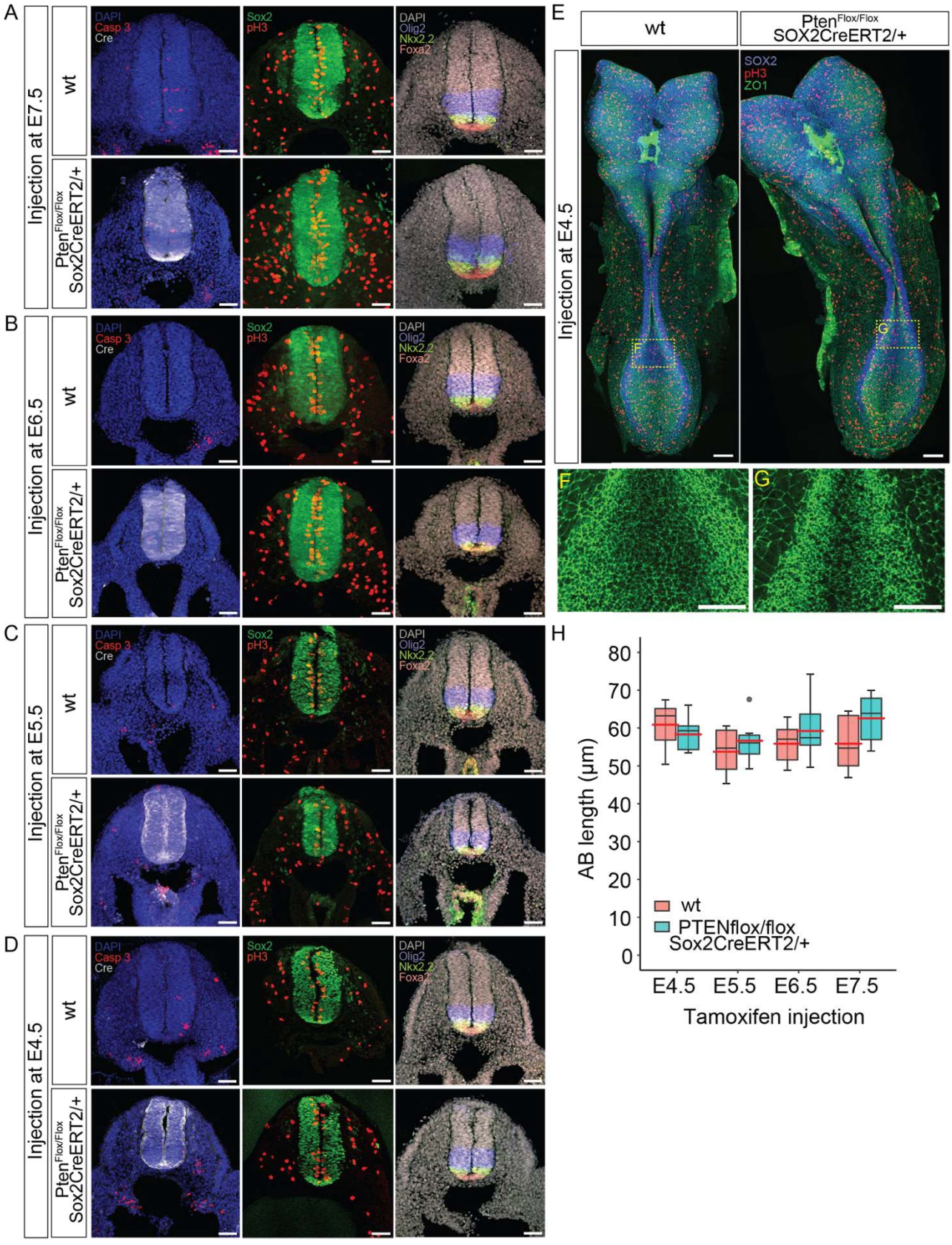
A
Injection at E7.5
wt
PtenFlox/Flox Sox2CreERT2/+
DAPI
Casp 3
Cre
Sox2
pH3
DAPI
Olig2
Nkx2.2
Foxa2
B
Injection at E6.5
C
Injection at E5.5
D
Injection at E4.5
E
wt
PtenFlox/Flox SOX2CreERT2/+
Injection at E4.5
SOX2
pH3
ZO1
F
G
H
AB length (µm)
0
10
20
30
40
50
60
70
80
wt
PTENflox/flox Sox2CreERT2/+
E4.5
E5.5
E6.5
E7.5
Tamoxifen injection

Figure 10. Pten conditional deletion in the neuroepithelium during development does not impact the epithelium architecture. E9.5 transverse sections of wild type (top) and Pten mutant (bottom) neural tubes that were collected **A.** after injection of tamoxifen at E7.5. **B.** after injection of tamoxifen at E6.5. **C.** after injection of tamoxifen at E5.5. **D.** after injection of tamoxifen at E4.5. Neural tube cross-sections were stained with Cre to detect Cre recombinase expression, with Caspase 3 to detect apoptotic cells, with Sox2 to mark the neural progenitors, with pH3 to detect mitotic cells and with distinct transcription factors to detect the ventral progenitor domains along the DV axis of the neural tube. **E.** E8.5 flat mounted Pten mutant and wild type mouse embryos that were collected after injecting tamoxifen at E4.5. **F.** Zoom-in ROI in the wild type caudal neural plate marked in E with a yellow dashed rectangle (left panel). **G.** Zoom-in ROI in ffe Pten mutant caudal neural plate marked in E with a yellow dashed rectangle (Right panel). **H.** Apicobasal length of the neuroepithelium at E9.5 after *Pten* knock-out at different stages during neural tube development. Boxplots represent 25-75% quartiles, median (black), mean (red), highest/lowest observations without outliers (whiskers). Two-sided t-tests ns, $P > 0.05$ for all pair-wise comparisons. Sample sizes : E4.5, wt: 2 embryos, 2 sections, Pten mutant: 3 embryos, 3 sections. E5.5, wt: 3 embryos, 2 sections, Pten mutant: 3 embryos, 3 sections. E6.5, wt: 5 embryos, 5 sections, Pten mutant: 5 embryos, 5 sections. E7.5, wt: 3 embryos, 3 sections, Pten mutant: 3 embryos, 3 sections.

3.5 Investigation of the effect of transient actomyosin perturbation in cell rearrangements during neural tube morphogenesis

The actomyosin complex within epithelial cells is responsible of generating contractile and tensile forces (Heisenberg & Bellaïche, 2013) that modulate cellular processes such us cell division (Scarpa et al., 2018), changes in cell geometry (Polyakov et al., 2014) and cell rearrangements (Curran et al., 2017). Thus, the mechanical forces generated by the actomyosin network can influence the global tissue topology and dynamics (Etournay et al., 2015).

In chapter 2, we report that the cell shapes and the neuroepithelium topological configuration throughout development maps to region C of the vertex model parameter space. In this region, the *in-silico* epithelium configuration is characterized by high line tension and contractility. Thus, *in-vivo* neuroepithelium topology could be characterized by high line tension and contractility. We wanted to investigate the potential role of these mechanical characteristics in cell rearrangement and neural tube morphogenesis. Therefore, we cultured E8.5 Rosa26:Confetti, Sox2creERT2/+ mouse embryos *ex-vivo* for 6 hours with 8μM Rock inhibitor Y-27632, which impairs actomyosin organization and reduces tissue tension in the mouse neural tube (Butler et al., 2019). After 6 hours treatment, the culture medium with Rock inhibitor was removed and embryos were further cultured for 36 hours in fresh culture medium. Prolonged exposure of the embryos to high concentration (8μM) of the Rock inhibitor resulted in low rates of embryo survival and impaired growth as reported in a previous study (Escuin et al., 2015).

Treatment of the epithelium for 6 hours with Y-27632 decreased F-actin apical accumulation. We found F-actin distributed in the lateral cortex of cells in Y-27632 treated neural plates, in contrast, F-actin was apically enriched in cells in the control condition (Figure 11A). The apical cell area was enlarged in Y-27632 neural plates as a result of the change in F-actin organization (Figure 11B). Body axis elongation was also affected right after inhibiting rock for 6 hours (Figure 11C-D), and after the transient inhibition of rock plus 36 hours of culture without Y-27632 (Figure 11E-F). In order to look at the effect of tension reduction in cell rearrangements, we analysed confetti clone fragmentation after 42 hours of culture, during which clones grew upon rock inhibition for 6 hours. The fragmentation coefficient of Y-27632 treated clones was only marginally smaller than the fragmentation coefficient of clones that grew in the control condition (Figure 11G-H). This result suggests that a transient decrease in tissue tension is not sufficient to induce significant changes in cell rearrangements.

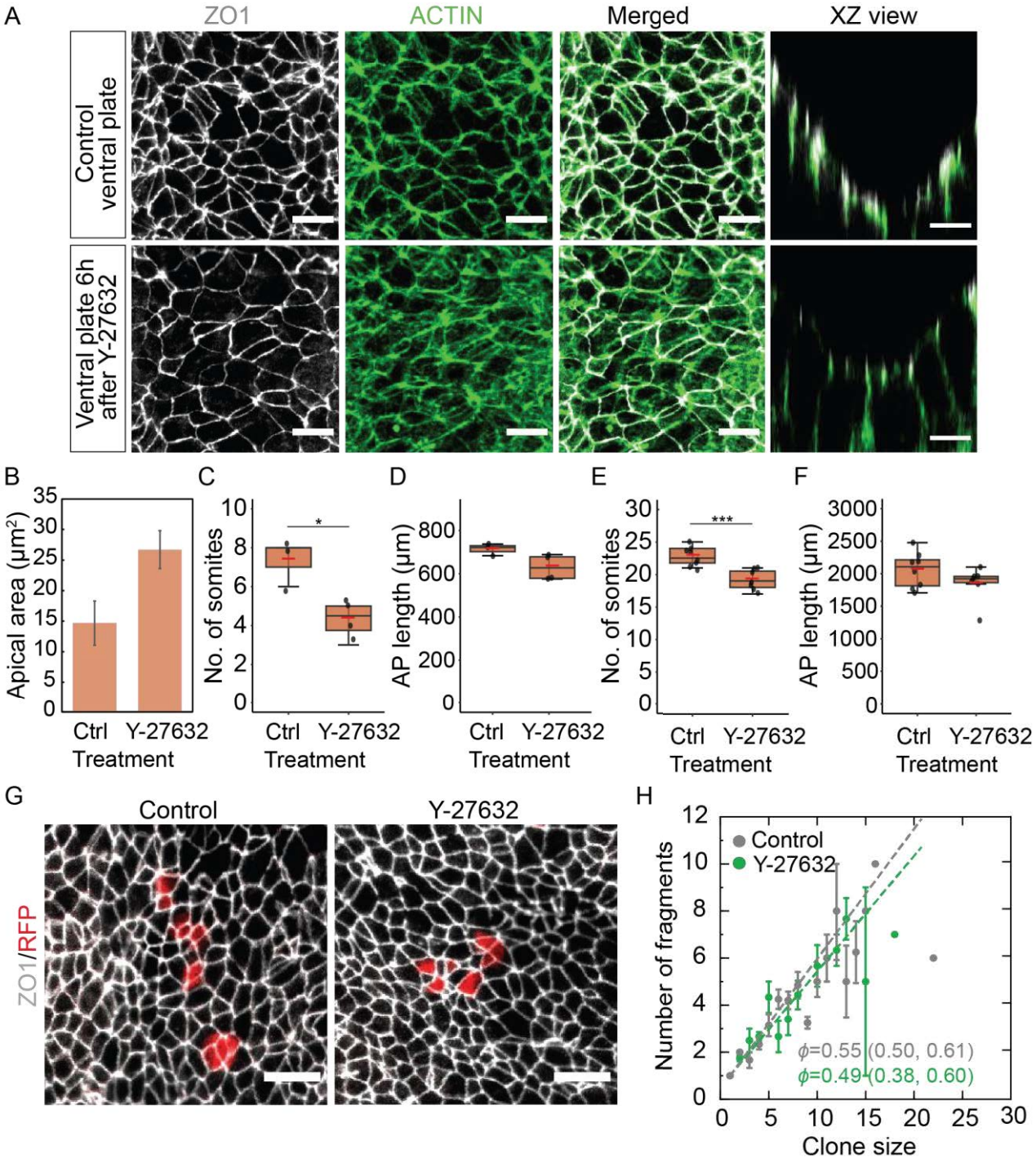

Figure 11. Transient perturbation of actomyosin does not affect cell rearrangement during neural tube development. A. E8.5 neural plate stained for ZO1 (white) and actin (green) after treatment with 8µM Y-27632 or vehicle for 6 hours. Left panels, apical view, right panel – apicobasal view. **B.** Apical cell area in embryos treated with 8µM Y-27632 or vehicle for 6 hours. Error bars, mean ± SEM. Sample sizes. Control, n: 2922 cells, Y-27632: 1728 cells. **C.** Number of somites in embryos treated with 8µM Y-27632 or vehicle for 6 hours. Two-sided t-tests *P = 0.021. **D.** Anterioposterior (AP) length of the prospective neural tube in embryos treated with 8µM Y-27632 or vehicle. AP length was quantified from the caudal edge of the head neural folds to the caudal end of the neural plate. Two-sided t-tests ns, P > 0.05. Sample sizes (C-D). Control, n: 3 embryos, Y-27632, n: 4 embryos. **E.** Number of somites for F. Two-sided t-tests ***P = 0.00061. **F.** Anterioposterior (AP) length of the neural tube in

embryos treated for 6 hours with 8µM Y-27632 or vehicle and subsequently cultured for 36 hours in absence of the ROCK inhibitor. AP length was quantified from the cervical region of the neural tube to the caudal end of the neural tube. Two-sided t-tests ns, $P > 0.05$. Boxplots represent 25-75% quartiles, median (black), mean (red), highest/lowest observations without outliers (whiskers). Sample sizes (E-F). Control, n: 8 embryos, Y-27632, n: 7 embryos. **G.** RFP labelled Confetti clones in Y-27632 treated embryos vs controls. ROCK inhibitor treatment was performed for 6h at E8.5, subsequently embryos were cultured for 36h without inhibitor before harvesting for analysis. **H.** Mean number of fragments per clone for a given clone size produced in neuroepithelium treated with 8µM Y-27632 or the vehicle for 6 hours and subsequently cultured without the treatment for 36 hours. Error bars, mean $\pm$ SEM. Sample sizes. Control n= 83 clones, Y-27632 n = 58 clones. Scale bars, 10 µm.

3.6 Analysis of the orientation of cell division in the neural plate

In order to qualitatively analyse the orientation of cell division, we collected E8.5 wild type embryos and stained them for Sox2, pH3 and ZO1 (Figure 14A). Then, we examined the orientation of positive pH3 nuclei in the caudal neural plate. We did not observe any obvious preferred orientation of the mitotic nuclei (Figure 14A, right panel). Furthermore, we measure the proliferation rate in different regions along the DV axis of the plate. We observed that proliferation is uniform across the neural plate (Figure 14B).

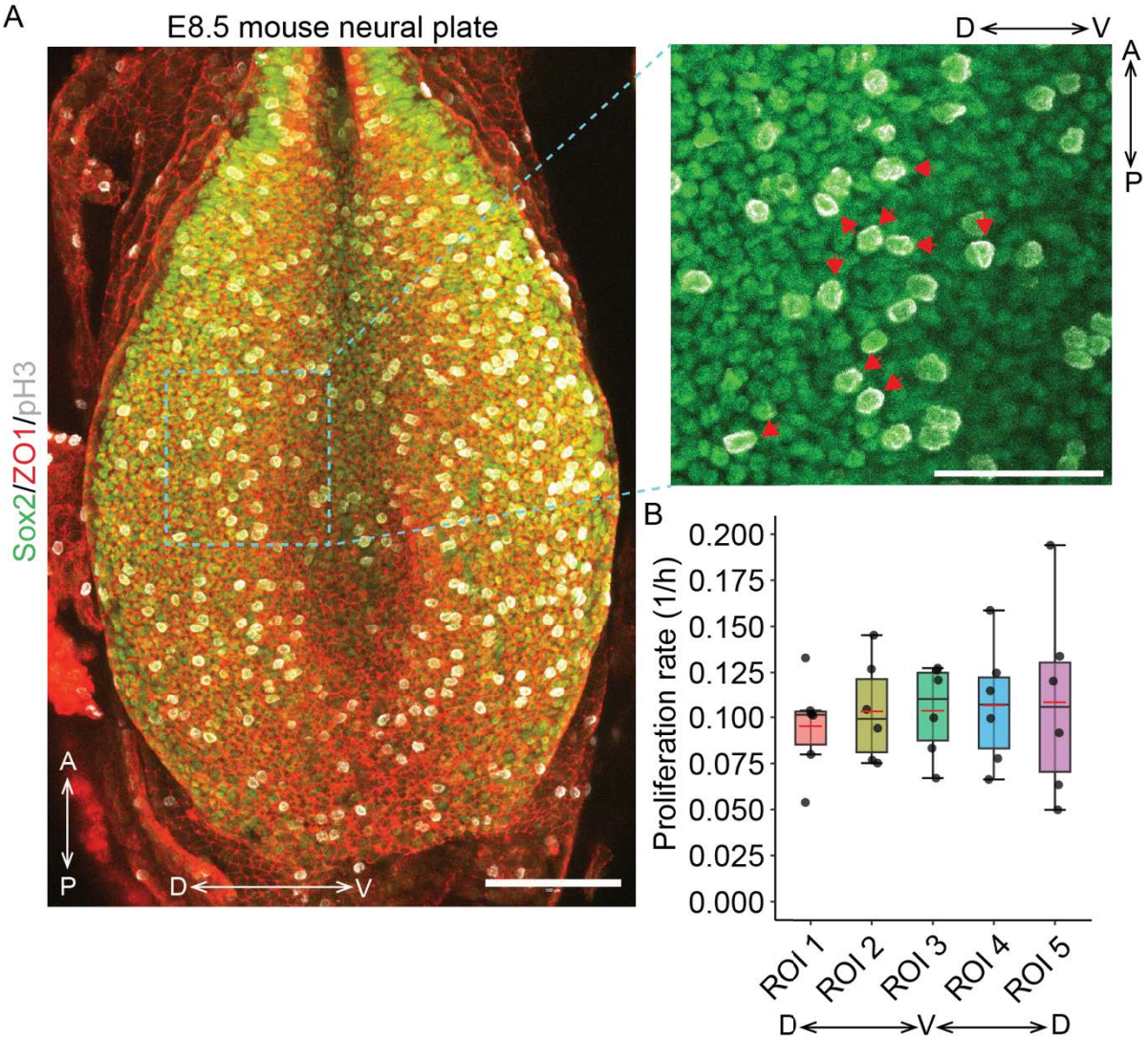

Figure 12. The rate of proliferation is uniform in the neural plate at E8.5. **A.** Left. E8.5 mouse neural plate stained for pH3 to detect mitotic nuclei, for Sox2 to marked the neuroepithelium and for ZO1 to marked the epithelium apical surface. Right. Zoomed-In ROI of the neural plate that contains ph3 positive nuclei. Red arrows indicate the orientation of the nuclei. **B.** Proliferation rate across the DV axis of the neural plate. Five ROIs distributed from the dorsal left to the dorsal right edge of the neural plate were used to quantify the mitotic index (pH3 positive cells/Sox2 positive cells). Then, the proliferation rate was estimated from the duration of mitosis. Boxplots represent 25-75% quartiles, median (black), mean (red), highest/lowest observations without outliers (whiskers). Sample sizes. 6 embryos.

Chapter 4. Discussion

Epithelial morphogenesis is fundamental for correct tissue formation and it is achieved by spatiotemporal coordination of distinct cellular processes such as cell division, changes in cell geometry, cell rearrangements and cell differentiation. Therefore, a quantitative description of the dynamics of these processes is crucial to understand how the changes in epithelia dynamics take place over time to direct morphogenesis. For instance, decrease of the apical surface of intestine progenitor cells is necessary for crypt formation (Sumigray et al., 2018), oriented cell divisions at early developmental stages are crucial for proper mouse gut and Drosophila germ band extension (Morais & Vincent, 2007; Matsuyama et al., 2009), and convergent extension in different epithelia such as Drosophila wing disc (Diaz de la Loza et al., 2018) and mouse neural plate (Ybot-Gonzalez et al., 2007) depends on cell rearrangements. Studies in the chick neural tube have suggested differences in cell displacement during development, which led us to investigate how these differences contribute to the epithelium dynamics and to determine which other accompanying cell processes could be involved in their temporal regulation.

In this study we developed an experimental quantitative framework compatible with computational tools, that allowed us to determine and quantify in parallel how mechanical forces, cell proliferation and cell differentiation influenced epithelial rearrangements. This framework that combined high resolution lineage tracing analysis, systematic quantification of cell geometry, and the vertex model revealed the epithelium material properties during development. We think this quantitative framework can be used in other epithelia to shed light on the relationship between epithelial cell dynamics, epithelial rheological properties and morphogenesis.

We observed a sharp decline in epithelial rearrangements over a 24-hour period, between E8.5 and E9.5, this occurs in the period of time in which the neural plate transforms into a tubular structure. The apical cell area and its heterogeneity, the cell shape index representing the energetically optimal cell shape that facilitates T1 transitions, and the cell elongation significantly decrease, whereas the % of hexagons that represent the degree of epithelia organization increases over the same period of time. The temporal dynamics of these cellular features indicate that they support the change of the neuroepithelium shape from E8.5 to E9.5 while the number of progenitors increases through cell division, and morphogens activities patterned the epithelium. From E9.5 to E11.5, cells cease to rearrange, the cells are predominantly hexagonal, cell shape index does not substantially change and the cell area and elongation continue decreasing, although to a lesser extent, indicating that the epithelium apical topology is more stable than at early stages. During this period of time the growth of the epithelium is not only mediated by cell division but also by cell differentiation, and patterning, as mentioned earlier, is sustained through transcriptional regulation between domains. The temporal description that we generated by analysing the apical surface of the epithelium and the neighbour relationships of neural progenitors during development provided a detailed temporal view of the cellular contributions to neural tube formation.

The functional experiments performed in this study, in conjunction with the vertex model revealed that the temporal dynamics of cell rearrangements are regulated by the net tissue growth rate. Over time, the decrease in the rate of proliferation and increase in the rate of cell differentiation lead to the reduction of epithelial rearrangements *in vivo*. Furthermore,

we encountered that cell cycle dependent IKNM introduces variation in apical cell area that influences junctional remodeling, thereby short cell cycle at E8.5 generates high apical area heterogeneity that elicits high levels of epithelial rearrangements. We observed that at this embryonic stage, the epithelium dynamics is dictated by T1 transitions ocurring between cells of different apical sizes in different configurations: before or after cell division, concomitant with cell division or in absence of cell division. This mechanism differs from other epithelia, such as the chick epiblast where active daughter cell separation upon cytokinesis induces cell rearrangements and thereby increases tissue fluidity (Firmino et al., 2016). The mechanism of rearrangements also differs from that uncovered in situations of aberrant cell growth in the Drosophila wing disc. In that case, cell area heterogeneity was found to generate packing discrepancies in the preferred cell side length, which promote cell rearrangements (Ramanathan et al., 2019). In this research study we present a distinct mechanism where IKNM, which is a conserved feature of proliferative epithelia (Meyer et al., 2011b), controls the dynamic change in apical cell area in accordance with the cell cycle kinetics, thereby influencing epithelial rearrangements and the epithelium dynamics.

The cell dynamics we report at different developmental stages characterize a change in the material properties of the epithelium from fluid-like to solid-like. Change in tissue fluidity in other epithelia have been observed to rely on distinct cellular dynamics. For instance, the decrease of random cell motion regulated by Fgf signalling in chick presomitic mesoderm (Bénazéraf et al., 2010), the increase in cell density in epithelia monolayers (Garcia et al., 2015) and in Xenopus head mesoderm (Barriga et al., 2018), and changes in cell shape mediated by fluctuations in cell-cell adhesion and contractile stresses in lung monolayers (Park et al., 2015). In our study, we encountered that the temporal dynamics of cell proliferation, rather than changes in cell mechanical forces, regulates the change in the epithelium material properties necessary to establish the correct aspect ratio of the tissue. Tissue solidification was previously found to be crucial for Zebrafish posterior axis elongation (Mongera et al., 2018), stressing the important role of the material properties in tissue morphogenesis. We found that change in the physical state of the neuroepithelium from fluid to solid-like occurs at high levels of junctional tension and contractility, which could be potentially mediated by the apical enrichment of the actomyosin network in the epithelium apical surface at early and late stages of development (Figure 3B-C). Interestingly, this mechanical regime in other epithelia has been described to influence tissue phase transitions in distinct manners. In MDCK cell monolayers, high ZO1 mediated cortex contractility drives contact inhibition that controls cell proliferation, thus preventing a cell density induced jamming transition (Skamrahl et al., 2021). In contrast, in Drosophila ommatidial tissue solidification arises from high junctional tissue tension mediated by E-cadherin dynamics (Founounou et al., 2021). Altogether, this evidence suggests that high levels of junctional tension and contractility can support both tissue fluidity and rigidity in epithelia to facilitate tissue morphogenesis.

The evidence we provide in this research study describe the relationship between epithelial cell dynamics, tissue growth and morphogenesis. Yet, the molecular regulators responsible for integrating cell behaviors at the tissue scale in the mouse neural tube remain poorly understood. To address this gap, we used the Lpt mutant mice to investigate the impact of inhibited PCP signalling on cell and epithelium dynamics. Our findings suggest that in order to understand the effect of depleted cell rearrangements on the emergent epithelium properties, it is necessary to measure how the tissue responds to the application of mechanical

forces. This will reveal the physical state of the epithelium and its relationship with the observed defects in morphogenesis. The Lpt mutant epithelium shape provides an ideal platform for implementing tools such as ferrofluid oil droplets or tissue scale laser ablation (Lenne & Trivedi, 2022) without perturbing the native configuration of the epithelium due to manipulation during tissue dissection. Thus, we think that further investigation of the Lpt mutant epithelium dynamics could refine the understanding of the role of mechanical stress, material properties and tissue morphogenesis during neural tube development.

While the present study sheds light on the dynamics of cell rearrangements during neural tube development, the potential link between these movements and morphogen signalling remains to be investigated. How high levels of epithelial rearrangements influence cell identity and the formation of morphogen gradients during neural tube morphogenesis, in particular between E8.5 to E9.5 when the gradients are established and cells are responsive to the morphogen activities, remains to be investigated. It is possible that frequent cell position exchange could alter the spatial distribution of morphogens, changing their local concentration and/or could affect the temporal exposure of neighbor cells to the signal, which could introduce noise during the interpretation of the gradient affecting cell identity acquisition and the formation of precise progenitor domain boundaries. During zebrafish neural keel formation, cell divisions and prominent cell movements generate distinct temporal Shh cell response profiles that are reinforced by locally heterogeneous signal (Xiong et al., 2013). Early cell fate specification and cell sorting were described to reconcile the extensive cell movement and heterogeneous morphogen gradient with patterning in this embryonic structure (Xiong et al., 2013) . This mechanism has been also observed to help establishing rhombomeres domain boundaries during zebrafish hindbrain convergent extension (Qiu et al., 2021). The degree of cell movement taking place in the zebrafish and mouse neuroepithelium differs, suggesting that cells might employ different mechanisms to support patterning at early developmental stages. Yet, in mouse further experimental investigation is required to describe the relationship between morphogen gradient formation and cell dynamics at early developmental stages. Live reporters of the morphogens and their effectors in conjunction with high resolution live imaging could help to investigate this potential relationship.

Chapter 5. Methods

5.1 Generation of MADM clones at different stages of neural tube development

To generate MADM clones, MADM-11$^{TG/TG}$ mice were crossed to MADM-11$^{GT/GT}$ (Hippenmeyer, et al., 2010), Sox2-CreERT2/+. MADM lines are composed of complementary cassettes that contain two chimeric fluorescent reporter genes eGFP and TdTomato. The GT cassette contains the N-terminus of eGFP and the C-terminus of TdTomato separated by a LoxP site, while the TG cassette contains the N-terminus of TdTomato and the C-terminus of eGFP also separated by a LoxP site (Zong et al., 2005). Both cassettes were inserted in the *Hipp11* loci on homologous chromosomes. Cre expression under the *Sox2* promoter drives interchromosomal recombination at the LoxP sites after tamoxifen mediated enzymatic activation, that results in reconstituted eGFP and TdTomato expression only in cells expressing Sox2 transcription factor, thus neural progenitors (Zong et al., 2005). Interchromosomal recombination take place during G2 phase of the cell cycle, subsequently during mitosis sister recombinant chromatids can be segregated into different daughter cells (X-segregation), each will express either eGFP or TdTomato (Zong et al., 2005). Alternatively, sister recombinant chromatids can be segregated in the same daughter cells that will expresse eGFP and TdT, while the other daughter cells will not express any fluorescent protein. Interchromosomal recombination can also take place in G1 where both fluorescent proteins are reconstituted making the cells to be double labelled (Zong et al., 2005).

To induce clonal labelling in MADM$^{TG/GT}$ trans-heterozygous Sox2-CreERT2 expressing embryos, pregnant females from the cross described above were injected with 3mg/mouse of tamoxifen (stock solution 15mg/ml) at E8.5, E9.5 and E10.5. Embryos were collected 24h after injection at the different stages and yolks sacs were collected and lysed for DNA extraction to proceed with genotyping for *Sox2*. Primers used to detect the wild type Sox2 allele were: OIMR0042, and OIMR0043. Primers used to detect Sox2CreERT2 mutant allele were: 344 and 345 (Table 1). For PCR reaction Phire Green Hot Start II Master mix (Thermo Scientific, F126S) was used and the following PCR steps were run: Initial denaturation 98°C for 30 seconds; denaturation 98°C for 30 seconds, annealing 55°C for 5 sec, extension 72°C for 15 sec this for 30 cycles; then 72°C for 1 min. Sox2CreERT2 heterozygous positive embryos were processed for immunostaining.

In order to detect the MADM clones tissue was stained for GFP and TdTtomato with Sheep anti-GFP and Rabbit anti-RFP, respectively, the apical surface of the epithelium labelled with Mouse anti-ZO1 and the p3 domain was labelled with Mouse anti-Nkx2.2 (Table 2).

5.2 Neural epithelium immunostaining and mounting

Sox2CreERT2 heterozygous positive embryos which are expressing reconstituted GFP and TdTomato were collected in cold 1X PBS. From E9.5 to E11.5, the apical surface of the epithelium is facing the lumen. Therefore, in order to have access to this surface of the epithelium it was necessary to dissect open the dorsal neural tube with a thin and sharp wire. The sharp wire was inserted in the cervical cavity and displaced posteriorly carefully cutting the surface ectoderm and neural tube at the dorsal midline. In the case of E8.5 embryos, they were dissected out of the yolk sac and were taken with tweezers from the head and neural plate to

be flattened and positioned with the dorsal side of the head plate facing the cover slip during the mounting step.

Fixation: Embryos were fixed in 4% PFA according to the stage, E9.5 embryos were fixed 50min, E10.5 embryos were fixed for 70 min and E11.5 embryos were fixed for 80min. After PFA fixation, embryos were washed with 0.1% tween in PBS, 3 times every 5 min keeping the embryos in ice or at 4°C.

Permeabilization: Embryos were washed with increased then decreased concentration of methanol in 0.1% tween in PBS to permeabilize the cells. In sequence, 25% MeTOH in 0.1% tween in PBS for 1 minute, 50% MeTOH in 0.1% tween in PBS for 1 minute, 75% MeTOH in 0.1% tween in PBS for 1 minute, 100% MeTOH for 1 minute. Subsequently, 75% MeTOH in 0.1% tween in PBS for 1 minute, 50% MeTOH in 0.1% tween in PBS for 1 minute and 25% MeTOH in 0.1% tween in PBS for 1 minute. Finalize with 3 washes every 5 minutes with 0.1% PBStween.

Primary antibody treatment: After permeabilization, embryos were incubated with the primary antibodies at 4°C overnight. Dilute the primary and secondary antibodies in pre-blocking solution (1% BSA in 0.1% PBSTween). After incubation with primary antibodies embryos were washed with 0.1% PBStween, 3 times for 5 minutes, then they were kept in 0.1% tween in PBS at 4°C for at least 8 hours.

Secondary antibody treatment: Embryos were incubated with secondary antibodies at 4°C overnight. Then, wash them with 0.1% PBStween, 3 times for 5 min and keep them at 4°C for at least 8 hours in 0.1% PBStween.

Mounting: Embryos were placed in a petri dish with cold 0.1% tween in PBS to continue with the flat mount preparation. The wire was used to fully bisect the neural tube in anterior to posterior direction along the AP axis and expose the apical surface of the epithelium. Subsequently, the mesodermal tissue underneath the neuroepithelium (somites) was removed. This was done by carefully pinching out the somites under the neural tissue with the tweezers and with help of the wire. The forelimb was cut out of the neural tube with the wire to proceed with flat mounting. The cut region was taken from the petri dish with a Pasteur pipette and put onto a glass slide, the apical side of the neural tissue facing up, then the excess of 0.1% tween in PBS was removed by carefully drying it with a piece of Kimtech precision wipe. Subsequently, Prolong™ Gold to mount the tissue was added (13ul per sample is recommended) and also a drop of grease in the 4 corners of a coverslip (18X18), the tissue was covered with it and sealed the edges of the coverslip with transparent nail polish.

In order to stain actin filaments and pMLC the following steps of the protocol were modified: Embryos were fixed in 4% PFA overnight and methanol fixation was omitted. To permeabilize the tissue, embryos were treated for 6 hours at room temperature with pre-blocking solution (5% BSA in 0.1% triton in PBS). Then, embryos are incubated with primary antibodies diluted in freshly prepared blocking solution at 4°C overnight. Subsequently, embryos were washed every 30 min 3 times with 0.1% triton in PBS and incubated for 2 hours in secondary antibodies diluted in pre-blocking solution at room temperature followed by washes every 30 min three times with 0.1% triton in PBS. Alexa fluor™ 488 Phalloidin was added together with the secondary antibody.

5.3 Generation of confetti clones, whole mouse embryo culture and pharmacological treatment

To generate confetti clones, Rosa26-Confetti (Brainbow 2.1) homozygous or heterozygous mice were crossed with Sox2creERT2 hemizygous (Sox2creERT2/+). Rosa26-Confetti (Brainbow 2.1) contains a cassette with the DNA sequence of four different fluorescent proteins: membrane targeted CFP, cytoplasmic YFP, cytoplasmic RFP and nuclear targeted GFP positioned in two inverted DNA sequences, each flanked by a pair of LoxP sites oriented in opposite direction (Livet et al., 2007). Tamoxifen Cre-mediated activation taking place only in cells expressing *Sox2* drive excision or inversion of the DNA sequences based on the orientation of the LoxP sites (Livet et al., 2007). Thus, Cre mediated chromosomal recombination leads to the stochastic expression of one out of four distinct fluorescent reporters in the neural progenitors. The frequency of recombination and level of expression of any of these fluorescence proteins depends on the amount of active Cre which is determine by the concentration of tamoxifen injected. Thereby to induce sparse clones, confetti clones were induced at E7.5 by injecting 0.75 mg/mouse of tamoxifen diluted in corn oil (stock solution 3.75mg/ml).

In order to culture whole E8.5 embryos the mouse embryo culture system was used and the following protocol of mouse embryo dissection and culture was followed:
Before starting embryo dissection clean the tweezers, the mouse embryo incubator and the stereoscope with 70 % ethanol to sterilize the workspace. Also, warm at 37°C the dissection medium and aliquots of rat serum according to the number of glass bottles to be cultured, and start the heat controller of the mouse embryo culture incubator (37°C). All the dissection process is carried out in small petri dishes (35/10 milimeters) with warm dissection medium which is composed by Gibco DMEM/F12 no phenol red (Thermofisher, 21041-025), 1X penicillin/streptomycin (Sigma, P4333) and 10 % FBS (fetal bovine serum, Thermofisher, 10270-106). 50 ml falcon tubes of dissection medium are prepared before embryo dissection and are warmed up at 37°C.

24 hours after tamoxifen injection, cut out the uterus of the female and transfer it to a dish with warm dissection medium, then carefully remove the fat and dissect out the uterus to expose the individual embryo decidua, then separate all decidua. Exchange frequently the culture medium while dissecting to keep the embryos warm and clean. Subsequently, remove the decidua without disrupting the yolk sac and the ectoplacental cone. Thus, E8.5 embryos are kept in the intact yolk sacs with the ectoplacental attached (Garcia et al., 2011). Once the E8.5 embryos are dissected place them in the 5 % CO2 cell incubator while preparing the culture medium. The culture medium is composed of dissection medium plus rat serum, 1:1 ratio, prepare fresh dissection medium to mix it with the rat serum.

Take the glass bottles of the mouse embryo culture and add 2.5ml of culture medium and place them in the rotator to calibrate them with the gas mixture. To growth E8.5 embryos 20% O_2 and 5 % of CO_2 was used, to growth E9.5 embryos 60 % O_2 and 5 % of CO_2 was used. Check that the gas mixture is feeding the rotator by looking at the glass tube outlet, approximately 1 bubble per second should appeared in the glass tube outlet. Then transfer the embryos in the glass bottles containing the warmed calibrated culture medium. Maximum 4 embryos can be cultured per bottle in 2.5 ml. During the embryo manipulation and transfer is recommended to use a Pasteur pipette with a cut tip coated with the medium. Finally, plug the bottles in the rotator and make it runs.

Pharmacological treatment: Once the mouse embryo culture was set up with the E8.5 embryos in the glass bottles, dilute the drug of interest to the desired concentration in the culture medium for a final volume of 2.5 ml, then plug the bottles in the rotator and start the culture.

To inhibit cell proliferation, E8.5 embryos were treated with 210 µM L-mimosine (Sigma M0253) or with 800nM of Aphidicolin (Sigma A0781) for 42 hours. To inhibit cell intercalation mediated by cell division the actomyosin dynamics was perturbed at E8.5 with 0.6 nM Calyculin A (Merck millipore 208851) for 42 hours. In order to perturb the mechanical characteristic of the neuroepithelium, actomyosin organization was impaired for 6 hours by treating E8.5 embryos with 8µM Rock inhibitor Y-27632 (Merck millipore 688000).

Embryo collection after culture and tissue preparation: 42 hours after embryo culture, approximately E10.0 embryos were retrieved. To check for normal embryo development the number of somites were counted, taking into account that a pair of somites is formed every two hours, in 42 hours, 21 pair of somites should have been formed. Also, heart beating and embryo turning was analysed. To record the morphology of the treated embryos upon drug or the vehicle, stereoscope pictures were taken. Subsequently, the yolk sacs were collected in cold 1X PBS as well as the embryos. Embryos were processed for staining as described in section 5.2 and yolk sacs were lysed for DNA extraction to proceed with genotyping for *Sox2* and the confetti cassette. Primers used to detect Sox2 are described in the Table. 1 and in the section 5.1. Primers used to detect the confetti cassette were: R26R Mt forward, R26R wt forward and common reverse (Table 1). For the PCR reaction the program described in section 5.1 was used for confetti and *Sox2* detection. Only embryos were Sox2CreERT2 heterozygous and that contained the Confetti cassette were processed for immunostaining and mounting. The apical surface of the epithelium expressing the confetti fluorescence proteins were stained with Mouse anti-ZO1 and the pMN domain was detected with Goat anti-Olig2 (Table 2). The fluorescent reporters of the confetti cassette were not enhanced by immunostaining, the native signal was imaged using a confocal microscope.

Table 1. Primers for PCR genotyping of all mouse lines used in the project.

Strain	Primer name	Primer sequence (5'- 3')	Detected allele
MADM 11 TG	TG forward	GGA CTG GGT GCT CAG GTA GTG GTT GTC G	MADM 11 TG mutant
MADM 11 TG	TG reverse	GGT ACG TCC AGG AGC GCA CCA TCT TCT TCA AGG	MADM 11 TG mutant
MADM 11 GT	GT forward	CCA AGC TGA AGG TGA CCA AG	MADM 11 GT mutant
MADM 11 GT	GT reverse	TCT TCT TCT GCA TTA CGG GG	MADM 11 GT mutant
MADM 11 TG/GT	Internal control DLX5 oIMR8744 contr.	CAA ATG TTG CTT GTC TGG TG	MADM 11 TG/GT wild type
MADM 11 TG/TG	Internal control DLX5 oIMR8745 contr.	GTC AGT CGA GTG CAC AGT TT	MADM 11 TG/GT wild type

Sox2CreERT2	344	GTC CAA TTT ACT GAC CGT ACA CC	Sox2CreERT2 mutant
Sox2CreERT2	345	GTT ATT CGG ATC ATC AGC TAC ACC	Sox2CreERT2 mutant
Sox2Cre-ERT2	Internal control OIMR0042	CTA GGC CAC AGA ATT GAA AGA TCT	Sox2CreERT2 Wild type
Sox2Cre-ERT2	Internal control OIMR0043	GTA GGT GGA AAT TCT AGC ATC ATCC	Sox2CreERT2 wild type
R26R Con-fetti	R26R Mt forward	GAA TTA ATT CCG GTA TAA CTT CG	R26R confetti mutant
R26R Con-fetti	Common reverse	CCA GAT GAC TAC CTA TCC TC	R26R confetti mutant
R26R Con-fetti	R26R wt forward	AAA GTC GCT CTG AGT TGT TAT	R26R confetti wild type
LPT/Lej	48765 forward	TGG CTG TCT TCT GCA CTC AC	LPT mutant
LPT/Lej	48766 reverse	GCA CCT TCT TGG TGC TCA CT	LPT mutant
mtmg	GT26 18 mutant re-verse	CTC TGC TGC CTC CTG GCT TCT	mT/mG mutant
mtmg	GT26 20 common forward	TCA ATG GGC GGG GGT CGTT	mT/mG mutant
mtmg	GT26 19 wt reverse	CGA GGC GGA TCA CAA GCA ATA	mT/mG wild type
R26Tomato	9105 mutant for-ward	CTG TTC CTG TAC GGC ATG G	R26Tomato mutant
R26Tomato	9103 mutant reverse	GGC ATT AAA GCA GCG TAT CC	R26Tomato mutant
R26Tomato	9020 wt forward	AAG GGA GCT GCA GTG GAG TA	R26Tomato wild type
R26Tomato	9021 wt reverse	CCG AAA ATC TGT GGG AAG TC	R26Tomato wild type
Pten floxed	Pten forward	CAA GCA CTC TGC GAA CTG AG	Pten floxed
Pten floxed	Pten reverse	AAG TTT TTG AAG GCA AGA TGC	Pten floxed
R26-ZO1-GFP	P3 com forward	TCC CTC GTG ATC TGC AAC TCC AGTC	R26-ZO1-GFP mutant
R26-ZO1-GFP	P6 mutant reverse	GCT GCA GGT CGA GGG ACC	R26-ZO1-GFP mutant
R26-ZO1-GFP	P4 wt reverse	AAC CCC AGA TGA CTA CCT ATC CTCC	R26-ZO1-GFP wild type

Table 2. List of antibodies used for immunostaining

Antibody name	Reference	Dilution	Labeling of
Mouse anti-ZO1	33-9100 Invitrogen	1:90	Apical junctions
Goat anti-Olig2	AF2418 R&D systems	1:100	pMN domain
Sheep anti-GFP	4745-1051 AbD Ser-otec	1:1000	Cytoplasmic GFP
Rabbit anti-RFP	600-401-379 Rock-land	1:2000	Cytoplasmic TdTomato and RFP
Mouse anti-Nkx2.2	74.5A5 DSHB	1:20	p3 domain

Rat anti-pH3	H9908 Sigma	1:1000	Mitotic cells
Goat anti-SOX2	AF2018 R&D systems	1:100	Neural progenitors
Rabbit anti-Brachyury	ab209665 abcam	1:100	Neuromesodermal progenitors
Rabbit-Phospho-Myosin Light chain 2 (Ser19)	3617 Cell signalling	1:50	Phosphorylated myosin II
Alexa fluor™ 488 Phalloidin	A12379 ThermoFisher Scientific	1:100	F-actin
Donkey anti-mouse Alexa fluor 647	Jackson Immuno	1:250	--
Donkey anti-goat FITC	Jackson Immuno	1:250	--
Donkey anti-rabbit Cy3	Jackson Immuno	1:1000	--
Donkey anti-rat Cy3	Jackson Immuno	1:1000	--
Donkey anti-sheep FITC	Jackson Immuno	1:250	--

5.4 High resolution imaging of MADM, confetti clones and of E8.5 whole mouse embryo

Imaging of the entire DV apical surface of the brachial neuroepithelium was performed in the Zeiss LSM880 inverted confocal microscope. Images were acquired with 40X objective with 1.3 NA oil objective through tile scanning with Z-slices 0.8µm apart, the scan mode was by frame and bidirectional, frame size was 1024 x 1024, pixel dwell time 0.77 µsec and pixel size 0.20 µm. Tiles were scanned with zoom 1 and were configured in the form of a grid and overlapped 10%.

In order to image the confetti fluorescent proteins three laser tracks were set up: For CFP, laser 458 with emission range 466-507nm, detected with the GaAsP detector. For RFP, laser 561 with emission range 566-623 nm, detected with the PMT detector. For YFP, laser 514 detected with emission range 517-562 nm, detected with GaAsP detector. The pinhole size was 2.0 µm (2.37 airy unit) for these three lasers. One more laser track was added to detect ZO1 junctional protein that was paired with the Donkey anti-mouse Alexa fluor 647. Laser 633 was used with emission range 651-735 nm, detected with PMT and pinhole size was 1.2 µm (1 airy unit).

In order to image the MADM fluorescent proteins three laser tracks were set up: For GFP, laser 488 with emission range 597-508 nm, detected with GaAsP detector. For TdTomato, laser 561 with emission range 575-615 nm, detected with the PMT detector. For Alexa 647 paired to ZO1, Laser 633 was used with emission range 651-735 nm, detected with PMT. The pinhole size was 1.2 µm for all the laser tracks in this case.

Imaging of E8.5 whole mouse embryos after flat mounting (see section 5.2) was performed in the Zeiss LSM880 inverted confocal microscope. Images were acquired with 40X objective with 1.3 NA oil objective through tile scanning with Z-slices 1.5µm apart, the scan mode was by frame and bidirectional, frame size was 1024 x 1024 and pixel size 0.20 µm. In order to

capture the entire embryo tile scanning was executed. Tiles were imaged with zoom 1 and were configured in the form of a grid and overlapped 10%.

5.5 Image processing, clone identification and quantification of clone fragmentation

MADM and confetti tiles were processed with FIJI. Confetti tiles were stitched with the Big-Stitcher pluggin.

To identify MADM clones, the progenitors marked with GFP and TdTomato were manually marked at their apical surface labelled with ZO1 staining. MADM clone were define as a group of adjacent progenitor cells labelled with GFP and Tdtomato, adjacent labelled cells were separated by less than 25 µm each to the nearest neighbour labelled cell. Clone fragments were defined as adjacent labelled cells that shared an edge or a vertex.

To identify confetti clones, CFP, RFP and YFP labelled progenitors were also manually marked at the apical surface (ZO1) and the coordinated of the cells marked by each colour were recorded independently. Based on the cell coordinates a custom-built python script classified clones by scanning each labelled cell with a 25 µm radius (approximately 5 cell diameters). If neighbor labelled cells were within the radius, they were grouped as a clone. Clone fragments were classified using a 5 µm radius (1 cell diameter) and correspond to labelled cells that strictly touch each other or that are separated by less than one cell.

In order to describe the temporal dynamics of epithelial rearrangements, from the clone and clone fragment classification the number of fragments per clone for a given clone size were quantified as well as a fragmentation coefficient.

5.6 Live imaging of the mouse neuroepithelium

In order to study epithelial rearrangement at the apical surface of the epithelium live, we used the R26-ZO1-GFP mouse line (Katsunuma et al., 2016)as well as the mtmg mouse line(Muzumdar et al., 2007). The R26-ZO1-GFP line allowed us to constitutively mark the cell junctions that outline the apical cell surface of the neural tube epithelium. On the other hand, the mtmg line allowed us sparsely labelled the membrane of the epithelium with membrane targeted GFP after Cre-mediated recombination. The mtmg cassette contained membrane targeted TdTomato flanked by unidirectional LoxP sites followed by the sequence of membrane targeted GFP. After tamoxifen dependent activation of Cre in the neural progenitor, Cre excises the mTdtomato through chromosomal recombination leading to the expression of mGFP (Muzumdar et al., 2007). The frequency of recombination and level of expression of membrane targeted GFP depends on the amount of active Cre which is determine by the concentration of tamoxifen injected.

In order to obtain embryos with cell edges labelled with GFP, R26-ZO1-GFP heterozygous mice were crossed between them to collect ZO1-GFP homozygous or heterozygous embryos. E8.5 and E10.5 embryos were dissected out of the uterus and decidua and kept in the yolk sac in warm dissection medium (see section 5.3). Before proceeding with mounting to performed live imaging, the culture medium is prepared and warm up at 37 °C (1:1 ratio of dissection medium and rat serum).

Two drops of silicon grease were placed adjacent to each other in the bottom of a 35mm Ibidi glass bottom dish (Ibidi Gmbh, 81218-200) and 2 ml of warm culture medium was added in the dish. Then, an 18 X 18 cover slip was cleaved in small pieces and a piece was placed on top of the two grease drops executing a little force so that it attached to the grease but also leaved space to slide the embryos. Subsequently, E8.5 embryos were transferred to the dish using a coated Pasteur pipette and the yolk sac was removed. E8.5 embryos were carefully slid and immobilized under the cover slips with the apical surface facing the glass, up to two embryos can be manipulated for imaging at the same time.

In order to immobilize the E10.5 neuroepithelium, first it was necessary to open up the neural tube from the dorsal side and bisected it using a sharp wire (see section 5.2). Then, only the brachial region was separated to be mounted and the mesoderm underneath was carefully removed without disrupting the apical surface. The dissected brachial neuroepithelium (explant) was transferred to the Ibidi glass bottom dish that had warm culture medium (2 ml) and the coverslip on silicon grease spacers. The epithelium was slid under cover slip with the apical surface facing the glass bottom, up to two brachial segments can be manipulated for imaging at the same time. The Ibidi dish with the E8.5 or E10.5 epithelium is transported to the confocal microscope where the environmental control chambered was set to 37 °C and it was supplied with 5 % CO_2.

Live imaging of the ZO1-GFP mouse embryos was performed with a Zeiss LSM800 inverted confocal microscope using a 40X/1.2X water objective. A region of interest in the dorsal half of the epithelium was scanned with 1.5 zoom by line, with Z-slices 0.75 μm apart for up to 4 hours with frames taken every 25 seconds. The frame size was 1024 x 1024, the frame time was 0.93 msec and pixel size was 0.1 μm. Junctional GFP was imaged with the 488 laser and the pinhole was opened to 2.12 airy units (1.0 μm). In order to avoid losing the apical surface from the range of imaging during acquisition because of thermal drift, the microscope chamber was set up to 37 °C 30 minutes before starting imaging, once imaging started another 30 min of thermal calibration was allowed by imaging the tissue with 100 gain and 0.05 % of laser power to not photo bleach the signal. Moreover, a big enough Z-stack was set with several slices left before reaching the apical plane to be imaged (-stack size was approximately 15 μm).

In order to collect sparsely membrane GFP marked neuroepithelium at E10.5, mtmg homozygous mice were crossed with Sox2creERT2 hemizygous (Sox2creERT2/+). To induce sparse membrane GFP expression 1 mg /mouse of tamoxifen in corn oil (stock 5 mg/ml) was injected in the females 24 hours (E9.5) before the embryo collection. At E10.5, embryos were collected and dissected for live imaging as described above. After dissection, the neural tube halves were kept in warm culture medium and were rapidly checked for fluorescent GFP signal under the fluorescence stereoscope, only GFP positive neural tubes were taking to cut out brachial segments (explants) to be mounted and live imaged.

Brachial segments were immobilized in a fibrinogen-thrombin clot in 35 mm Idibi glass bottom dishes. The immobilize the brachial segments first they were washed in drops (2) of approximately 50 μl fibrinogen on a dish lid. Fibrinogen (Merck millipore US1341573) was prepared fresh before every experiment to 8mg/ml concentration and it was dissolved in DMEM/F12 (Thermofisher, 21041-025). Then, the brachial segments were transferred with a coated and cut pipette tip to the glass bottom dish were previously several drops of 10 μl

fibrinogen were placed at the bottom. Once the brachial segments were in the fibrinogen drops, they were positioned with the apical surface facing the glass bottom and the excess of fibrinogen was removed so that the surface of it slightly touched the explant, this hindered explant flipping. Subsequently, 5 µl of thrombin (Sigma T7326) were added carefully on top of the fibrinogen drop (one brachial explant per drop) to form the clot. Small drops of thrombin were also added at the edges of the fibrinogen drop to seal the clot which had dried in approximately 30 seconds. Finally, 2 ml of culture medium was added and the Ibidi dish was transferred to the microscope where the environmental control chambered was set to 37 °C and it was supplied with 5 % CO_2.

Live imaging of the membrane GFP marked neuroepithelium was performed with a Zeiss LSM800 inverted confocal microscope using a 40X/1.2X water objective. A region of interest in the dorsal half of the epithelium was scanned with 1 zoom by line, with Z-slices 0.7 µm apart for up to 6 hours with frames taken every 5 minutes. The frame size was 1024 x 1024, pixel size was 0.13 µm. Membrane GFP was imaged with the 488 laser and the pinhole was opened to 2 airy units (1.0 µm) and membrane TdTomato was imaged with the 561 laser and the pinhole was opened to 2 airy units (1.0 µm). In order to avoid losing the apical membrane from the range of imaging during acquisition because of thermal drift, the microscope chamber was set up to 37 °C 30 minutes before starting imaging, once imaging started another 30 min of thermal calibration was allowed by imaging the tissue with 100 gain and 0.05 % of laser power to not photo bleach the signal. Moreover, a big enough Z-stack was set with several slices left before reaching the membrane plane to be imaged (Z-stack size was approximately 50 µm).

5.7 EdU labelling of the mouse neuro epithelium at E8.5 and E10.5

In order to detect the cell cycle phase of neural progenitors in the E8.5 and E10.5 epithelium EdU pulses and RFP and PH3 immunostaining were performed. First, Sox2creERT2 hemizygous mice were crossed to Rosa26-Tdtomato heterozygous or homozygous in order to labelled the cytoplasm of the neural progenitors with RFP. The Rosa26-Tdtomato is composed by a LoxP flanked stop cassette that block the expression of the TdTomato DNA sequence located after the stop cassette (Madisen et al., 2010). Thus, after Cre-mediated chromosomal recombination in Sox2 positive cells the stop cassette is excised permitting Tdtomato expression. The frequency of recombination and level of expression of this fluorescent protein depends on the amount of active Cre which is determine by the concentration of tamoxifen injected. Thereby to induced sparse labelling at E8.5, 3 mg/mouse of tamoxifen in corn oil (stock 15mg/ml) were injected at E6.5. To induce sparse labelling at E10.5, 0.08 mg/mouse of tamoxifen (stock solution 0.4mg/ml) were injected at E9.5.

After induction of TdTomato labelling in order to mark cells in S phase at E8.5, 0.5 mg of EdU (Invitrogen A10044) in 1X PBS (stock 2.5 mg/ml) were injected 20 minutes before embryo collection. To mark cells in S phase at E10.5 after induction of TdTomato labelling, 0.5 mg of EdU in 1X PBS were injected 30 min before embryo collection. To mark cells in G2 phase 0.5 mg of EdU in 1X PBS was injected 2 hours before embryo collection. Embryos at different stages and after the EdU pulses were collected, dissected and prepared for immunostaining as described in the section 5.2.

EdU incorporation was detected using the Alexa Fluor-488 antibody from the Click-iT EdU imaging kit and protocol (Invitrogen, C10337). Tissue prepared for immunostaining was incubated with ZO1 and RFP primary antibodies overnight at 4 °C then washed and incubated with the secondary antibodies including DAPI following the protocol of immunostaining in section 5.2. Subsequently, tissue was incubated with the Click-iT reaction that contains Alexa Fluor-488 for 30 minutes at room temperate, followed by washes with 3 % BSA in 1X PBS 3 times every 7 minutes. After tissue was mounted as described in section 5.2.

In order to label cells in mitosis at E8.5 and E10.5 after induction of TdTomato labelling as described above. Embryos were collected, dissected and prepared for immunostaining as described in section 5.2. The neuroepithelium was immunostained for ZO1, TdTomato, pH3 and DAPI.

Imaging of the flat mounted tissue was performed in the LSM880 inverted confocal microscope. Images were acquired with 40X objective with 1.3 NA oil objective through tile scanning with Z-slices 0.65 μm apart, the scan mode was by frame and bidirectional, frame size was 1024 x 1024, pixel dwell time 0.77 μsec and pixel size 0.20 μm. Tiles were scanned with zoom 1 and were configured in the form of a grid and overlapped 10%. The pinhole size for the different laser tracks was 1.2 μm (1 airy unit).

5.8 Neuroepithelium segmentation

In order to segment and quantify different cell shape descriptors of the neuroepithelium at different developmental stages, E8.5, E9.5, E10.5 and E11.5 embryos were processed as described in section 5.2, immunostained for ZO1 and imaged as describe in section 5.4, with pinhole size 1.2 μm (1 airy unit) and Zoom 1.

Regions of interest (ROIs) of 50 μm x 50 μm at different domain along the DV axis were cropped to be segmented using the Tissue Analyser (TA) pluggin from FIJI (Aigouy et al., 2016). Cell boundaries were automatically detected using the watershed algorithm in the pluggin and the segmented mesh was manually revised. TA plugin provided description of polygonal mesh including vertices and edges of cell outlines as well as the number and identity of cell neighbours. Cell shape descriptors were quantified as described in Guerrero et al., 2019. TA pluggin was also used to segment the live imaging movies of ZO1-GFP marked neuroepithelium at E8.5 and E10.5 (Aigouy et al., 2016).

Imaris 9.1 was used to quantify the distance of nuclei at distinct cell cycle phases relative to the apical surface. Tracing the cell body labelled with TdTomato together with the EdU labelled nuclei to the apical surface of the epithelium allowed to identify the apical surface of neural progenitors in S and G2 phase. Then, the distance of the nuclei was quantified as well as the apical cell area at E8.5 and E10.5.

In order to quantify the cell area associated to the different cell cycle phases, segmentation was performed in Imaris 9.1. The cell wizard detection from Imaris menu was selected. Then, membrane-based detection, a filter for cell diameter, the source channel for the segmentation (ZO1) and the filter type, which was local contrast (water shed algorithm) were chosen as the parameters to produce the segmentation. Subsequently, ROIs were specified on the

single apical (ZO1 marked) that contained the cells to be segmented and then segmentation was produced. If errors were generated, the cell membrane intensity threshold to improve the segmentation was adjusted. The cell area was estimated from the segmented cell volume within the relevant Z-slice divided by the voxel depth (0.65 μm).

Same segmentation steps were followed to quantify the sub-apical area of membrane GFP marked neural progenitors over time and analyse the dynamics during mitosis. In this case, the channel for segmentation was GFP, the ROIs that contained the cells to be segmented were specified 3 to 4 slices bellow the apical cell membrane corresponding to 2.1-2.8 μm bellow, and the voxel depth to quantify the cell area was 0.7 μm.

References

Aigouy, B., Umetsu, D., & Eaton, S. (2016). Segmentation and quantitative analysis of epithelial tissues. *Methods in Molecular Biology*, 1478, 227–239.

Andrews, M. G., Del Castillo, L. M., Ochoa-Bolton, E., Yamauchi, K., Smogorzewski, J., & Butler, S. J. (2017). BMPs direct sensory interneuron identity in the developing spinal cord using signal-specific not morphogenic activities. *ELife*. 6:e30647.

Araya, C., Tawk, M., Girdler, G. C., Costa, M., Carmona-Fontaine, C., & Clarke, J. D. W. (2014). Mesoderm is required for coordinated cell movements within zebrafish neural plate in vivo. *Neural Development*, *9*(9).

Araya, C., Ward, L. C., Girdler, G. C., & Miranda, M. (2016). Coordinating cell and tissue behavior during zebrafish neural tube morphogenesis. *Developmental Dynamics*, *245*(3), 197–208.

Balaskas, N., Ribeiro, A., Panovska, J., Dessaud, E., Sasai, N., Page, K. M., Briscoe, J., & Ribes, V. (2012). Gene regulatory logic for reading the sonic hedgehog signaling gradient in the vertebrate neural tube. *Cell*, *148*(1–2), 273–284.

Barriga, E. H., Franze, K., Charras, G., & Mayor, R. (2018). Tissue stiffening coordinates morphogenesis by triggering collective cell migration in vivo. *Nature*, *554*(7693), 523–527.

Bénazéraf, B., Francois, P., Baker, R. E., Denans, N., Little, C. D., & Pourquié, O. (2010). A random cell motility gradient downstream of FGF controls elongation of an amniote embryo. *Nature*, *466*(7303), 248–252.

Bloomekatz, J., Grego-Bessa, J., Migeotte, I., & Anderson, K. V. (2012). Pten regulates collective cell migration during specification of the anterior-posterior axis of the mouse embryo. *Developmental Biology*, *364*(2), 192–201.

Briscoe, J., & Small, S. (2015). Morphogen rules: Design principles of gradient-mediated embryo patterning. *Development, 142*(23), 3996–4009.

Brooks, E. R., Islam, M. T., Anderson, K. V., & Zallen, J. A. (2020). Sonic hedgehog signaling directs patterned cell remodeling during cranial neural tube closure. *ELife*, 9:e60234.

Burstyn-Cohen, T., & Kalcheim, C. (2002). Association between the Cell Cycle and Neural Crest Delamination through Specific Regulation of G1/S Transition. *Developmental Cell*, *3*(3), 383–395.

Butler, M. B., Short, N. E., Maniou, E., Alexandre, P., Greene, N. D. E., Copp, A. J., & Galea, G. L. (2019). Rho kinase-dependent apical constriction counteracts M-phase apical expansion to enable mouse neural tube closure. *Journal of Cell Science*, *132*(13): jcs230300.

Cayuso, J., Ulloa, F., Cox, B., Briscoe, J., & Marti, E. (2006). The Sonic hedgehog pathway independently controls the patterning, proliferation and survival of neuroepithelial cells by regulating Gli activity. *Development*, *133*(3), 517–528.

Chaffee, B. R., Hoang, T. V., Leonard, M. R., Bruney, D. G., Wagner, B. D., Dowd, J. R., Leone, G., Ostrowski, M. C., & Robinson, M. L. (2016). FGFR and PTEN signaling interact during lens development to regulate cell survival. *Developmental Biology*, *410*(2), 150 -163.

Chiang, C., Litingtung, Y., Lee, E., Young, K. E., Corden, J. L., Westphal, H., & Beachy, P. A. (1996). Cyclopia and defective axial patterning lacking Sonic hedgehog gene function. *Nature*, *383*(6599), 407–413.

Copp, A. J., & Greene, N. D. E. (2010). Genetics and development of neural tube defects. *Journal of Pathology, 220*(2), 217–230.

Cunningham, T. J., Kumar, S., Yamaguchi, T. P., & Duester, G. (2015). Wnt8a and Wnt3a Cooperate in the Axial Stem Cell Niche to Promote Mammalian Body Axis Extension. *Developmental Dynamics*, *244*(6), 797–807.

Curran, S., Strandkvist, C., Bathmann, J., de Gennes, M., Kabla, A., Salbreux, G., & Baum, B. (2017). Myosin II Controls Junction Fluctuations to Guide Epithelial Tissue Ordering. *Developmental Cell*, *43*(4), 480-492.e6.

da Silva, S. M., & Vincent, J. P. (2007). Oriented cell divisions in the extending germband of Drosophila. *Development*, *134*(17), 3049–3054.

De Goederen, V., Vetter, R., Mcdole, K., & Iber, D. (2022). Hinge point emergence in mammalian spinal neurulation. *PNAS*, *119*(20): e2117075119.

Delfino-Machín, M., Lunn, J. S., Breitkreuz, D. N., Akai, J., & Storey, K. G. (2005). Specification and maintenance of the spinal cord stem zone. *Development*, *132*(19), 4273–4283.

Diaz-de-la-Loza, M. del C., Ray, R. P., Ganguly, P. S., Alt, S., Davis, J. R., Hoppe, A., Tapon, N., Salbreux, G., & Thompson, B. J. (2018). Apical and Basal Matrix Remodeling Control Epithelial Morphogenesis. *Developmental Cell*, *46*(1), 23-39.e5.

Eom, D. S., Amarnath, S., Fogel, J. L., & Agarwala, S. (2011). Bone morphogenetic proteins regulate neural tube closure by interacting with the apicobasal polarity pathway. *Development*, *138*(15), 3179–3188.

Erskine, L., Patel, K., & Clarke, J. D. W. (1998). Progenitor Dispersal and the Origin of Early Neuronal Phenotypes in the Chick Embryo Spinal Cord. *Developmental Biology*, *199*(1), 26–41.

Escuin, S., Vernay, B., Savery, D., Gurniak, C. B., Witke, W., Greene, N. D. E., & Copp, A. J. (2015). Rho-kinase-dependent actin turnover and actomyosin disassembly are necessary for mouse spinal neural tube closure. *Journal of Cell Science*, *128*(14), 2468–2481.

Etournay, R., Popović, M., Merkel, M., Nandi, A., Blasse, C., Aigouy, B., Brandl, H., Myers, G., Salbreux, G., Jülicher, F., & Eaton, S. (2015). Interplay of cell dynamics and epithelial tension during morphogenesis of the Drosophila pupal wing. *ELife*, 4:e07090.

Exelby, K., Herrera-Delgado, E., Perez, L. G., Perez-Carrasco, R., Sagner, A., Metzis, V., Sollich, P., & Briscoe, J. (2021). Precision of tissue patterning is controlled by dynamical properties of gene regulatory networks. *Development*, *148*(4): dev197566.

Ferreira, M. A., Despin-Guitard, E., Duarte, F., Degond, P., & Theveneau, E. (2019). Interkinetic nuclear movements promote apical expansion in pseudostratified epithelia at the expense of apicobasal elongation. *PLoS Computational Biology*, *15*(12): e1007171.

Firmino, J., Rocancourt, D., Saadaoui, M., Moreau, C., & Gros, J. (2016). Cell Division Drives Epithelial Cell Rearrangements during Gastrulation in Chick. *Developmental Cell*, *36*(3), 249–261.

Founounou, N., Farhadifar, R., Collu, G. M., Weber, U., Shelley, M. J., & Mlodzik, M. (2021). Tissue fluidity mediated by adherens junction dynamics promotes planar cell polarity-driven ommatidial rotation. *Nature Communications*, *12*(1): 6974.

Galea, G. L., Cho, Y. J., Galea, G., Molè, M. A., Rolo, A., Savery, D., Moulding, D., Culshaw, L. H., Nikolopoulou, E., Greene, N. D. E., & Copp, A. J. (2017). Biomechanical coupling facilitates spinal neural tube closure in mouse embryos. *PNAS*, *114*(26), E5177–E5186.

Galea, G. L., Maniou, E., Edwards, T. J., Marshall, A. R., Ampartzidis, I., Greene, N. D. E., & Copp, A. J. (2021). Cell non-autonomy amplifies disruption of neurulation by mosaic Vangl2 deletion in mice. *Nature Communications*, *12*(1): 3301.

Galea, G. L., Nychyk, O., Mole, M. A., Moulding, D., Savery, D., Nikolopoulou, E., Henderson, D. J., Greene, N. D. E., & Copp, A. J. (2018). Vangl2 disruption alters the biomechanics

of late spinal neurulation leading to spina bifida in mouse embryos. *Disease Models and Mechanisms, 11(3)*: dmm032219.

Garcia, M. D., Udan, R. S., Hadjantonakis, A. K., & Dickinson, M. E. (2011). Preparation of postimplantation mouse embryos for imaging. *Cold Spring Harbor Protocols*, *6*(4).

Garcia, S., Hannezo, E., Elgeti, J., Joanny, J. F., Silberzan, P., & Gov, N. S. (2015). Physics of active jamming during collective cellular motion in a monolayer. *PNAS*, *112*(50), 15314–15319.

Geldmacher-Voss, B., Reugels, A. M., Pauls, S., & Campos-Ortega, J. A. (2003). A 90° rotation of the mitotic spindle changes the orientation of mitoses of zebrafish neuroepithelial cells. *Development*, *130*(16), 3767–3780.

Greene, N. D. E., Gerrelli, D., Van Straaten, H. W. M., & Copp, A. J. (1998). Abnormalities of floor plate, notochord and somite differentiation in the loop-tail (Lp) mouse: a model of severe neural tube defects. *Mechanisms of Development*, *73*(1), 59 –72.

Grego-Bessa, J., Bloomekatz, J., Castel, P., Omelchenko, T., Baselga, J., & Anderson, K. V. (2015). The tumor suppressor PTEN and the PDK1 kinase regulate formation of the columnar neural epithelium. *ELife*, 5:e12034.

Guerrero, P., Perez-Carrasco, R., Zagorski, M., Page, D., Kicheva, A., Briscoe, J., & Page, K. M. (2019). Neuronal differentiation influences progenitor arrangement in the vertebrate neuroepithelium. *Development*, *146*(23): dev176297.

Heisenberg, C. P., & Bellaïche, Y. (2013). Forces in tissue morphogenesis and patterning. *Cell*. *153*(5): 948-62.

Henrique, D., Abranches, E., Verrier, L., & Storey, K. G. (2015). Neuromesodermal progenitors and the making of the spinal cord. *Development*, *142*(17), 2864–2875.

Hippenmeyer, S., Youn, Y. H., Moon, H. M., Miyamichi, K., Zong, H., Wynshaw-Boris, A., & Luo, L. (2010). Genetic mosaic dissection of Lis1 and Ndel1 in neuronal migration. *Neuron*, *68*(4), 695–709.

Hoijman, E., Rubbini, D., Colombelli, J., & Alsina, B. (2015). Mitotic cell rounding and epithelial thinning regulate lumen growth and shape. *Nature Communications*, *16*(6): 7355.

Horne-Badovinac, S., Lin, D., Waldron, S., Schwarz, M., Mbamalu, G., Pawson, T., Jan, Y.-N., Stainier, D. Y. R., & Abdelilah-Seyfried, S. (2001). Positional cloning of heart and soul reveals multiple roles for PKCλ in zebrafish organogenesis. *Current Biology*, *11*(19), 1492–1502.

Huang, H., Potter, C. J., Tao, W., Li, D.-M., Brogiolo, W., Hafen, E., Sun, H., & Xu, T. (1999). PTEN affects cell size, cell proliferation and apoptosis during Drosophila eye development. *Development*, *126*(23), 5365–5372.

Ishii, M., Tateya, T., Matsuda, M., & Hirashima, T. (2021). Stalling interkinetic nuclear migration in curved pseudostratified epithelium of developing cochlea. *Royal Society Open Science*, *8*(12): 211024.

Jayachandran, P., Olmo, V. N., Sanchez, S. P., McFarland, R. J., Vital, E., Werner, J. M., Hong, E., Sanchez-Alberola, N., Molodstov, A., & Brewster, R. M. (2016). Microtubule-associated protein 1b is required for shaping the neural tube. *Neural Development*, *11*(1).

Jeong, J., & McMahon, A. P. (2005). Growth and pattern of the mammalian neural tube are governed by partially overlapping feedback activities of the hedgehog antagonists patched 1 and Hhip1. *Development*, *132*(1), 143–154.

Katsunuma, S., Honda, H., Shinoda, T., Ishimoto, Y., Miyata, T., Kiyonari, H., Abe, T., Nibu, K. I., Takai, Y., & Togashi, H. (2016). Synergistic action of nectins and cadherins generates

the mosaic cellular pattern of the olfactory epithelium. *Journal of Cell Biology*, *212*(5), 561–575.

Kicheva, A., Bollenbach, T., Ribeiro, A., Valle, H. P., Lovell-Badge, R., Episkopou, V., & Briscoe, J. (2014). Coordination of progenitor specification and growth in mouse and chick spinal cord. *Science*, *345*(6204):1254927.

Kicheva, A., & Briscoe, J. (2015). Developmental Pattern Formation in Phases. *Trends in Cell Biology*, *25*(10), 579–591.

Kidokoro, H., Yonei-Tamura, S., Tamura, K., Schoenwolf, G. C., & Saijoh, Y. (2018). The heart tube forms and elongates through dynamic cell rearrangement coordinated with foregut extension. *Development, 145*(7): dev152488.

Kosodo, Y., Suetsugu, T., Suda, M., Mimori-Kiyosue, Y., Toida, K., Baba, S. A., Kimura, A., & Matsuzaki, F. (2011). Regulation of interkinetic nuclear migration by cell cycle-coupled active and passive mechanisms in the developing brain. *EMBO Journal*, *30*(9), 1690–1704.

Kuzmicz-Kowalska, K., & Kicheva, A. (2021). Regulation of size and scale in vertebrate spinal cord development. *Wiley Interdisciplinary Reviews Developmental Biology*, *10*(3): e383.

Leber, S. M., & Sanes, J. R. (1995). Migratory Paths of Neurons and Glia in the Embryonic Chick Spinal Cord. *The Journal of Neuroscience, 15*(2): 1236-48.

Lenne, P. F., Munro, E., Heemskerk, I., Warmflash, A., Bocanegra-Moreno, L., Kishi, K., Kicheva, A., Long, Y., Fruleux, A., Boudaoud, A., Saunders, T. E., Caldarelli, P., Michaut, A., Gros, J., Maroudas-Sacks, Y., Keren, K., Hannezo, E., Gartner, Z. J., Stormo, B., … Tlili, S. (2021). Roadmap for the multiscale coupling of biochemical and mechanical signals during development. *Physical Biology*, *18*(4).

Lenne, P. F., & Trivedi, V. (2022). Sculpting tissues by phase transitions. *Nature Communications*, *13*(1): 664.

Leung, B., & Shimeld, S. M. (2019). Evolution of vertebrate spinal cord patterning. In *Developmental Dynamics*, *248*(11), 1028–1043.

Livet, J., Weissman, T. A., Kang, H., Draft, R. W., Lu, J., Bennis, R. A., Sanes, J. R., & Lichtman, J. W. (2007). Transgenic strategies for combinatorial expression of fluorescent proteins in the nervous system. *Nature*, *450*(7166), 56–62.

Lobjois, V., Benazeraf, B., Bertrand, N., Medevielle, F., & Pituello, F. (2004). Specific regulation of cyclins D1 and D2 by FGF and Shh signaling coordinates cell cycle progression, patterning, and differentiation during early steps of spinal cord development. *Developmental Biology*, *273*(2), 195–209.

Lowery, L. A., & Sive, H. (2004). Strategies of vertebrate neurulation and a re-evaluation of teleost neural tube formation. *Mechanisms of Development*, *121*(10), 1189–1197.

Lunn, J. S., Fishwick, K. J., Halley, P. A., & Storey, K. G. (2007). A spatial and temporal map of FGF/Erk1/2 activity and response repertoires in the early chick embryo. *Developmental Biology*, *302*(2), 536–552.

Madisen, L., Zwingman, T. A., Sunkin, S. M., Oh, S. W., Zariwala, H. A., Gu, H., Ng, L. L., Palmiter, R. D., Hawrylycz, M. J., Jones, A. R., Lein, E. S., & Zeng, H. (2010). A robust and high-throughput Cre reporting and characterization system for the whole mouse brain. *Nature Neuroscience*, *13*(1), 133–140.

Mahaffey, J. P., Grego-Bessa, J., Liem, K. F., & Anderson, K. V. (2013). Cofilin and Vangl2 cooperate in the initiation of planar cell polarity in the mouse embryo. *Development*, *140*(6), 1262–1271.

Marahatta, A., McElhinney, K., Howard, T. A., & Ware, R. E. (2015). Pharmacokinetics and Tissue Distribution of Hydroxyurea in a Mouse Model. *Blood*, *126*(23), 4579–4579.

Massa, V., Savery, D., Ybot-Gonzalez, P., Ferraro, E., Rongvaux, A., Cecconi, F., Flavell, R., Greene, N. D. E., & Copp, A. J. (2009). Apoptosis is not required for mammalian neural tube closure. *Proceedings of the National Academy of Sciences*, *106*(20), 8233–8238.

Mathis, L., & Nicolas, J. F. (2000). Different clonal dispersion in the rostral and caudal mouse central nervous system. *Development*, *127*(6), 1277–1290.

Matsuyama, M., Aizawa, S., & Shimono, A. (2009). Sfrp controls apicobasal polarity and oriented cell division in developing gut epithelium. *PLoS Genetics*, *5*(3): e1000427.

McGreevy, E. M., Vijayraghavan, D., Davidson, L. A., & Hildebrand, J. D. (2015). Shroom3 functions downstream of planar cell polarity to regulate myosin II distribution and cellular organization during neural tube closure. *Biology Open*, *4*(2), 186–196.

McShane, S. G., Molè, M. A., Savery, D., Greene, N. D. E., Tam, P. P. L., & Copp, A. J. (2015). Cellular basis of neuroepithelial bending during mouse spinal neural tube closure. *Developmental Biology*, *404*(2), 113–124.

Megason, S. G., & McMahon, A. P. (2002). A mitogen gradient of dorsal midline Wnts organizes growth in the CNS. *Development*, *129*(9), 2087–2098.

Meyer, E. J., Ikmi, A., & Gibson, M. C. (2011a). Interkinetic nuclear migration is a broadly conserved feature of cell division in pseudostratified epithelia. *Current Biology*, *21*(6), 485–491.

Molè, M. A., Galea, G. L., Rolo, A., Weberling, A., Nychyk, O., de Castro, S. C., Savery, D., Fässler, R., Ybot-González, P., Greene, N. D. E., & Copp, A. J. (2020). Integrin-Mediated Focal Anchorage Drives Epithelial Zippering during Mouse Neural Tube Closure. *Developmental Cell*, *52*(3), 321-334.e6.

Mongera, A., Rowghanian, P., Gustafson, H. J., Shelton, E., Kealhofer, D. A., Carn, E. K., Serwane, F., Lucio, A. A., Giammona, J., & Campàs, O. (2018). A fluid-to-solid jamming transition underlies vertebrate body axis elongation. *Nature*, *561*(7723), 401–405.

Muzumdar, M. D., Tasic, B., Miyamichi, K., Li, N., & Luo, L. (2007). A global double-fluorescent cre reporter mouse. *Genesis, 45*(9), 593–605.

Nikolopoulou, E., Galea, G. L., Rolo, A., Greene, N. D. E., & Copp, A. J. (2017). Neural tube closure: cellular, molecular and biomechanical mechanisms. *Development*, *144*(4), 552–566.

Nishimura, T., Honda, H., & Takeichi, M. (2012). Planar cell polarity links axes of spatial dynamics in neural-tube closure. *Cell*, *149*(5), 1084–1097.

Norden, C. (2017). Pseudostratified epithelia - cell biology, diversity and roles in organ formation at a glance. *Journal of Cell Science*, *130*(11), 1859–1863.

Norden, C., Young, S., Link, B. A., & Harris, W. A. (2009). Actomyosin Is the Main Driver of Interkinetic Nuclear Migration in the Retina. *Cell*, *138*(6), 1195–1208.

Nowak, K., Seisenbacher, G., Hafen, E., & Stocker, H. (2013). Nutrient restriction enhances the proliferative potential of cells lacking the tumor suppressor PTEN in mitotic tissues. *ELife*. 2:e00380.

Park, J. A., Kim, J. H., Bi, D., Mitchel, J. A., Qazvini, N. T., Tantisira, K., Park, C. Y., McGill, M., Kim, S. H., Gweon, B., Notbohm, J., Steward, R., Burger, S., Randell, S. H., Kho, A. T., Tambe, D. T., Hardin, C., Shore, S. A., Israel, E., … Fredberg, J. J. (2015). Unjamming and cell shape in the asthmatic airway epithelium. *Nature Materials*, *14*(10), 1040–1048.

Petridou, N. I., Grigolon, S., Salbreux, G., Hannezo, E., & Heisenberg, C. P. (2019). Fluidization-mediated tissue spreading by mitotic cell rounding and non-canonical Wnt signalling. *Nature Cell Biology*, *21*(2), 169–178.

Petridou, N. I., & Heisenberg, C. (2019). Tissue rheology in embryonic organization. *The EMBO Journal*, *38*(20): e102497.

Polyakov, O., He, B., Swan, M., Shaevitz, J. W., Kaschube, M., & Wieschaus, E. (2014). Passive mechanical forces control cell-shape change during drosophila ventral furrow formation. *Biophysical Journal*, *107*(4), 998–1010.

Qiu, Y., Fung, L., Schilling, T. F., & Nie, Q. (2021). Multiple morphogens and rapid elongation promote segmental patterning during development. *PLoS Computational Biology*, *17*(6): e1009077.

Ramanathan, S. P., Krajnc, M., & Gibson, M. C. (2019). Cell-Size Pleomorphism Drives Aberrant Clone Dispersal in Proliferating Epithelia. *Developmental Cell*, *51*(1), 49-61.e4.

Ran Straaten, H. W. M., & Hekking, J. W. M. (1991). Anatomy and Embryology Development of floor plate, neurons and axonal outgrowth pattern in the early spinal cord of the notochord-deficient chick embryo. *Anatomy and Embryol*ogy, 184(1), 55-63.

Saadaoui, M., Rocancourt, D., Roussel, J., Corson, F., & Gros, J. (2020). A tensile ring drives tissue flows to shape the gastrulating amniote embryo. *Science*, *367*(6476), 453–458.

Saade, M., Gutiérrez-Vallejo, I., LeDréau, G., Rabadán, M. A., Miguez, D. G., Buceta, J., & Martí, E. (2013). Sonic hedgehog signaling switches the mode of division in the developing nervous system. *Cell Reports*, *4*(3), 492–503.

Sagner, A., & Briscoe, J. (2019). Establishing neuronal diversity in the spinal cord: A time and a place. *Development, 146*(22): dev182154.

Sausedo, R. A., Smith, J. L., & Schoenwolf, G. C. (1997). Role of nonrandomly oriented cell division in shaping and bending of the neural plate. *Journal of Comparative Neurology*, *381*(4), 473–488.

Scarpa, E., Finet, C., Blanchard, G. B., & Sanson, B. (2018). Actomyosin-Driven Tension at Compartmental Boundaries Orients Cell Division Independently of Cell Geometry In Vivo. *Developmental Cell*, *47*(6), 727-740.e6.

Skamrahl, M., Pang, H., Ferle, M., Gottwald, J., Rübeling, A., Maraspini, R., Honigmann, A., Oswald, T. A., & Janshoff, A. (2021). Tight Junction ZO Proteins Maintain Tissue Fluidity, Ensuring Efficient Collective Cell Migration. *Advanced Science*, *8*(19): e2100478.

Spear, P. C., & Erickson, C. A. (2012). Interkinetic nuclear Migration: A mysterious Process in search of function. *Development, Growth & Differentiation*, *54*(3), 306–316.

Steventon, B., Duarte, F., Lagadec, R., Mazan, S., Nicolas, J. F., & Hirsinger, E. (2016). Species-specific contribution of volumetric growth and tissue convergence to posterior body elongation in vertebrates. *Development*, *143*(10), 1732–1741.

Strzyz, P. J., Lee, H. O., Sidhaye, J., Weber, I. P., Leung, L. C., & Norden, C. (2015). Interkinetic Nuclear Migration Is Centrosome Independent and Ensures Apical Cell Division to Maintain Tissue Integrity. *Developmental Cell*, *32*(2), 203–219.

Sumigray, K. D., Terwilliger, M., & Lechler, T. (2018). Morphogenesis and Compartmentalization of the Intestinal Crypt. *Developmental Cell*, *45*(2), 183-197.e5.

Takahashi, T., Nowakowski, R. S., & Caviness, V. S. (1995). The Cell Cycle of the Pseudostratified Ventricular Epithelium of the Embryonic Murine Cerebral Wall. *The Journal of Neuroscience, 15*(9), 6046-6057.

Tozer, S., Le Dréau, G., Marti, E., & Briscoe, J. (2013). Temporal control of BMP signalling determines neuronal subtype identity in the dorsal neural tube. *Development*, *140*(7), 1467–1474.

Tzouanacou, E., Wegener, A., Wymeersch, F. J., Wilson, V., & Nicolas, J. F. (2009). Redefining the Progression of Lineage Segregations during Mammalian Embryogenesis by Clonal Analysis. *Developmental Cell*, *17*(3), 365–376.

Wartlick, O., Mumcu, P., Kicheva, A., Bittig, T., Seum, C., Jülicher, F., & González-Gaitán, M. (2011). Dynamics of Dpp Signaling and Proliferation Control. *Science*, *331*(6021), 1154–1159.

Wilcock, A. C., Swedlow, J. R., & Storey, K. G. (2007). Mitotic spindle orientation distinguishes stem cell and terminal modes of neuron production in the early spinal cord. *Development*, *134*(10), 1943–1954.

Williams, M., Yen, W., Lu, X., & Sutherland, A. (2014). Distinct apical and basolateral mechanisms drive planar cell polarity-dependent convergent extension of the mouse neural plate. *Developmental Cell*, *29*(1), 34–46.

Xiong, F., Tentner, A. R., Huang, P., Gelas, A., Mosaliganti, K. R., Souhait, L., Rannou, N., Swinburne, I. A., Obholzer, N. D., Cowgill, P. D., Schier, A. F., & Megason, S. G. (2013). Specified neural progenitors sort to form sharp domains after noisy Shh signaling. *Cell*, *153*(3), 550–561.

Yanakieva, I., Erzberger, A., Matejčić, M., Modes, C. D., & Norden, C. (2019). Cell and tissue morphology determine actin-dependent nuclear migration mechanisms in neuroepithelia. *Journal of Cell Biology*, *218*(10), 3272–3289.

Ybot-Gonzalez, P., Cogram, P., Gerrelli, D., & Copp, A. J. (2002). Sonic hedgehog and the molecular regulation of mouse neural tube closure. *Development*, *129*, 2507–2517.

Ybot-Gonzalez, P., Savery, D., Gerrelli, D., Signore, M., Mitchell, C. E., Faux, C. H., Greene, N. D. E., & Copp, A. J. (2007). Convergent extension, planar-cell-polarity signaling and initiation of mouse neural tube closure. *Development*, *134*(4), 789–799.

Zagorski, M., Tabata, Y., Brandenberg, N., Lutolf, M. P., Tkačik, G., Bollenbach, T., Briscoe, J., & Kicheva, A. (2017). Decoding of position in the developing neural tube from antiparallel morphogen gradients. *Science*, *356*(6345), 1379–1383.

Zong, H., Espinosa, J. S., Su, H. H., Muzumdar, M. D., & Luo, L. (2005). Mosaic analysis with double markers in mice. *Cell*, *121*(3), 479–492.